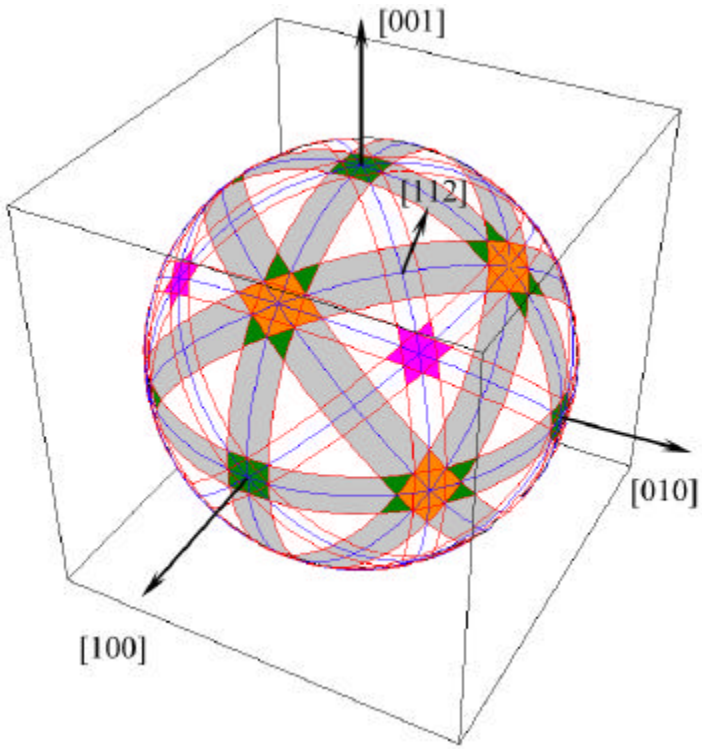

Figure 1-1. The visibility band map of a spherical f.c.c. crystal. This provides an elegant means of unification of all the subjects in this thesis. For details please refer to 1.5 and 3.3.2.

DIRECT SPACE (NANO)CRYSTALLOGRAPHY VIA HIGH-RESOLUTION TRANSMISSION ELECTRON MICROSCOPY

by

WENTAO QIN

A DISSERTATION

Presented to the Faculty of the Graduate School of the

UNIVERSITY OF MISSOURI-ROLLA

In partial Fulfillment of the Requirements for the Degree

DOCTOR OF PHILOSOPHY

in

PHYSICS

2000

_____	_____
Philip B. Fraundorf, Advisor	Edward B. Hale, Co-advisor
_____	_____
William J. James	Bernard J. Feldman
_____	_____
Joseph W. Newkirk	Oran A. Pringle

_____

Haresh Siriwardane

ABSTRACT

This thesis focuses on direct space nanocrystallography in 3-dimension (3D) via high-resolution transmission electron microscopy (HRTEM). It comprises three topics, each of which is presented in a chapter. Chapter 2 describes the development and application of an analytical technique to determine the lattice parameters of a nanocrystal from direct space images taken at two tilts. The development mainly involves choosing two appropriate viewing directions to resolve the lattice structure in 3D. General principles for establishing data acquisition protocols as well as certain protocols for some simple and popular lattices are presented. In the application of one of the protocols, the lattice parameters of a 10 nm f.c.c. WC_{1-x} crystal are determined. The significance of this technique lies in that it provides 3D crystal lattice structure information, and possesses the atomic-resolution of HRTEM. In Chapter 3, a semi-empirical model for predicting lattice fringe visibility after tilt is presented. It is based on studying the relative positions of the reciprocal lattice spots of the diffracting lattice plane set and the Ewald sphere in 3D. Modified versions of the model enable predicting the invisibility of the lattice fringes and quantifying the probability of such an invisibility after tilt. A new concept of visibility band of a set of lattice planes of a spherical crystal is introduced. The ensemble of visibility bands of a nanocrystal, the visibility band map, is like a roadmap to guide direct space nanocrystallographic analyses in 3D. In this sense, a visibility band map is much like a Kikuchi map, and in principle contains the solutions to all the problems encountered in the thesis. In Chapter 4, both the probability of success and the uncertainties of reciprocal lattice vectors in applying the stereo analysis technique described in Chapter 2 are quantified. The relationship to calculate the size of a reciprocal lattice spot was determined, and it is the key to obtaining numeric solutions to all the problems encountered in the thesis. Improvement of the probability of success and reduction of reciprocal lattice vector uncertainties are discussed.

ACKNOWLEDGMENTS

I have continued to learn both science and how to work with people during my Ph. D. study. I want to thank my advisor, Dr. Phil Fraundorf for teaching me this. In doing research with him, his expertise in physics and microscopy has helped to elevate our understanding of technical issues to higher levels. His introduction of visibility band and band map provides not only a thorough understanding of HRTEM of nanocrystals, but also an elegant means of unification of all the subjects in my thesis. The Fourier Analysis course he taught has had crucial impact on my research. It is from this course that I learned to some degree about the relationship between direct space and reciproal space. In numerous cases I practiced making presentations in his presence. I have benefited from his industrial experience in team work and communication.

I fortunately have chosen a great thesis committee consisting of excellent scholars with diverse backgrounds. Being able to think and act to orient toward “materials physics” is an important step for me to take, and it is after communicating with my committee members that I could do that. Dr. Haresh Siriwardane first “showed me the door” to do reseach and indoctrinated some industrial ethics as well, always with his patience and encouragement. Dr. James and Dr. Shih have provided specimens for my experiments, as well as instructive insights about thin film issues in materials science. All my thesis projects were carried out through analyzing these samples. Dr. Pringle advised me to “make the thesis work managable” on the very first day I submitted my Ph. D. study proposal. Dr. Newkirk cautioned me to be aware of the capabilities and limitations of existing techniques (such as CBED) before developing a new one, and the fact that “not all the particles are round”. Dr. Feldman advised me of conciseness in writing, and has always been a strong backup for my industrial outreach activities. Dr. Hale assigned a problem involving the diffraction of two atoms in my qualifying exam. I solved the problem based on the geometry between the reciprocal lattice spots and the Ewald sphere. This later provided a prototype for me to solve almost all the problems in Chapter 3 and 4. Dr. Fraundorf, Dr. Hale, Dr. Pringle and Roberta Cox, the Graduate

Studies Assistant in College of Arts and Sciences, have assisted me in professional formatting. I am grateful to all of them.

Beginning from the time I joined Dr. Fraundorf's group, Dr. Mulestagno in MEMC has always encouraged me explore industrial opportunities "beyond campus", and given advice while I walked along this track. Dr. Augusto Morrone and Dr. Mike Hintz offered me the opportunity to be an Engineering Intern at Seagate Technology, Inc. The experience of working with talented industrial engineers has broadened my knowledge and made me excited.

The Physics Department of UM-St. Louis has provided me opportunities in teaching undergraduate physics labs and discussion. This is an invaluable experience. My oral commnication skill has been improved, and I have learned some American culture. Being able to get high student evaluation in the last two semesters has given me the confidence to work and live in the U.S. Dr. Wilking has kindly helped me on administrative work in the Ph. D. program.

The librarians in the Interlibrary Loan of the Thomas Jefferson Library have offered effective assistance with my loan requests. Thanks to their help, my literature research was finished in a timely manner. They are: Lucinda, Lisandras, and Mary.

I fortunately have my wife, Lihong, to accompany me on the walk through this path. My sister, Wenning, has assisted me in business professional writing. Thanks to my father, Haiyue, my mother, Peizhen, and my elder sister Wenjing.

TABLE OF CONTENTS

LIST OF ILLUSTRATIONS

Figure Page

LIST OF TABLES

1. INTRODUCTION

In this chapter, techniques and the literature on crystallographic analysis and 3-dimensional (3D) reconstruction in transmission electron microscopy are outlined. The resolution limits of these techniques are reviewed. In context of the scaling-down trend in materials science and engineering, this chapter argues that direct space crystallography by high-resolution TEM can provide 3D lattice information from arbitrarily small crystals. As computer and microscope performance evolves, this approach will be of increasing usefulness, for the study of nanoscale structures already common in advanced materials today.

1.1. TRANSMISSION ELECTRON MICROSCOPES AND CRYSTALLOGRAPHY

In the advancement of materials science and engineering, it is necessary to observe, analyze and understand phenomena occuring on a small size scale. The transmission electron microscope (TEM) is a powerful and versatile instrument which permits characterization of materials. The first TEM was built by two German scientists, M. Knoll and E. Ruska, in 1932 (Knoll, 1932). The first comercial TEM, MetropolitanVickers EM1, was manufactured in the UK in 1936. Nowadays TEMs have become widely available. Major manufacturers include Philips, JEOL and Hitachi.

In a TEM a high-energy (~100 keV) electron beam is transmitted through the specimen. During transmission, the electrons interact with the specimen, giving rise to signals containing information about the internal structure and chemistry of the specimen. Electron diffraction patterns and lattice images are two forms of data which allow crystallographic analysis in TEM. Two types of electron diffraction patterns in TEM are referred to as selected area electron diffraction (SAED) and convergent beam electron diffraction (CBED). Lattice images are interference patterns between the direct beam and diffracted beams, viewed in direct space, and are obtained by high-resolution TEM (HRTEM) imaging. In the images, the spacing of a set of fringes is proportional to the

lattice spacing when the corresponding lattice planes meet the Bragg condition. Among these crystallographic techniques, HRTEM has the highest resolution. For direct inference of defect structure on the atomic scale, a sub-two-angstrom point resolution in an HRTEM is particularly useful, given that this is the typical spacing between atoms in solids (Spence, 1988a).

1.2. LIMITS OF CRYSTALLOGRAPHY TECHNIQUES IN TEM

In this section, the limits of the crystallographic techniques mentioned above are discussed. These include limits on crystal size, spatial resolution and sensitivity to vertical position (along the direction of the electron beam in the specimen).

1.2.1. Resolution Limits of Diffraction In SAED, the sample is illuminated with a parallel electron beam to ensure convergence of the incident unscattered electrons on the back focal plane of the objective lens. A specific area of the sample is selected by an SAED aperture that is in an "image plane" conjugate with the sample in the electron optic system of the TEM. The inserted SAED aperture creates a virtual aperture in the sample plane, giving a selected area that is about 0.4 μm or greater, in diameter (Williams, 1996b). A few hundred nanometers is therefore the typcal lateral size of the region sampled by SAED in TEM.

Historically CBED is older than SAED. It was developed by Kossel and Möllenstedt in 1939 before LePoole developed SAED in 1947 (Kossel, 1939; Lepoole, 1947). Compared with SAED, CBED can examine smaller areas. In CBED, the incident electron beam is converged and focused down to a spot 10-100 nm in diameter on the region of interest by a pre-specimen lens (the second condenser lens, C2) (Williams, 1996g) . The size of the focused electron beam as incident on the sample, determines the sampled volume which in turn defines the resolution of CBED.

Only under "kinematical" conditions, i.e., when either the crystal thickness is less than about one-tenth of the extinction distance under a two-beam condition or when the crystal orientation is far away from all Bragg-conditions, can single-scattering events become dominant and CBED source regions approach the size of the beam size (Gevers,

1970; Hirsch, 1977c; Edington, 1976e). However, when the specimen is so thin as to satisfy kinematical condition, the diffraction disks are uniformly bright and devoid of contrast. The resulting patterns will give no more information than the SAED ones. Their only advantage over SAED is that they come from smaller regions. This is one of a few cases in which higher "resolution" is achieved by focusing the electron beam.

With a thermionic electron gun, the electron beam can in principle be focused down to 1 nm, yet a compromise in beam intensity occurs. The intensity will be so low that the diffraction patterns are difficult to observe or record. A field emission gun (FEG) can make an improvement in this regard, since it offers brightness that is two to three orders higher than that of a thermionic gun (Williams, 1996a). For this reason, CBED with a subnanometer resolution has become possible but only in a TEM equipped with a field emisison gun, as pioneered by Cowley and co-workers (Cowley, 1981; Cowley, 1996; Liu M., 1994). Nanodiffraction has been applied to study the structures of nanometer metal particles in supported metal catalysts, and more recently to carbon nanotubes. For example, Monosmith and Cowley determined the existence of twining and multiple twining in Au particles on an amorphous support (Monosmith, 1984). Iijima showed that carbon nanotubes consist of concentric cylinders of graphitic carbon sheets, some of which have one or more distict helical angles (Iijima, 1991). Cowley confirmed the polygonal shape of carbon nanutubes and suggested the possibility of obtaining an ordered 3D graphitic structure in the planar areas of the tube walls (Cowley, 1996). Some difficulties are found with nanodiffraction, as a result of the necessarily large diffraction spots. From these large spots it is impossible to accurately measure lattice parameters, and sometimes even the symmetry of the patterns may be confused (Cowley, 1996).

In short, for thin crystals the sampled volume of the CBED technique is close to the electron beam spot size, which is in the range of 10-100 nm (in diameter). This can go below a nanometer only in a field emission gun TEM (FEGTEM). Nanodiffraction is the form of CBED with the highest sampling resolution, and has proven useful in studies of very small crystals.

When the crystal thickness is greater than one extinction distance, CBED becomes more versatile, and can be applied to the determination of crystal lattice

symmetry, structure factor, strain and lattice parameters, characterization of crystal defects and so on (Eades, 1989; Changmo, 1991). With so much thickness, however, the electron beam will be spread out, mainly due to multiple scattering events (Williams, 1996h).

Another disadvantage of CBED is that the specimen is more likely to be contaminated or damaged by the electron beam. As is true in general, the high-energy electron beam causes both contamination and damage to the specimen. A major source of contamination is the residual hydrocarbons from the pump oil or the specimen surface, which crack under the electron beam. Carbonaceous material is then fixed on the irradiated area. This local contamination can also cause stress in the specimen. Damage takes two principle forms, radiolysis and knock-on damage. In radiolysis, the chemical bonds of certain materials such as polymers and alkali halides are broken through inelastic scattering. In knock-on damage, atoms of crystal lattice sites are displaced by the high-energy electrons, creating point defects. When the electron beam is focused, as in CBED, the beam is more intense, hence both contamination and damage are more severe.

1.2.2. **Two-Dimensional Nature of Transmission Electron Data** A fundamental limit of transmission electron microscopy (TEM) arises from the two-dimensional (2D) nature of transmitted electron data. This includes selected area electron diffraction (SAED) patterns and lattice images (Williams, 1996m). Each micrograph carrying such information, to first order, represents a 2D projection of the 3D object subjected to the electron beam. This lack of depth sensitivity often results in ambiguous data on the structure of the examined object. For example, in crystallographic analysis where the phase is unknown, it is possible that different candidate lattices can generate selected area electron diffraction patterns identical to the experimental one within measurement error (Qin, 2000a).

1.3. THREE-DIMENSIONAL RECONSTRUCTION TECHNIQUES IN TEM

There are different 3D reconstruction schemes in TEM. Here we focus on one of them, which is the correlation of transmission data taken at different tilts. A brief introduction to another will be given in 1.3.4.

1.3.1. Three-dimensional Reconstruction Scheme The side-entry goniometer tilt stage in a transmission electron microscope provides specimen orientation adjustment capability. This allows acquiring projections of an examined object from different viewing angles. The orientation adjustment capability is enhanced by using special holders, including double-tilt and tilt-rotate holders. Proper correlation of these projections serves the purpose of expanding the 2D limit of transmission electron data in a TEM to 3D.

1.3.2. Reconstruction From Kikuchi Diffraction Patterns 3D reconstruction of crystal lattices in reciprocal space has been mainly performed from one or more Kikuchi diffraction patterns taken at different tilts. The accuracy achieved is very high. Kikuchi maps have been widely used in crystallographic analysis. However, this technique faces some serious problems in analyzing small crystals that are beyond the resolution limit. We'll begin with a review of Kikuchi diffraction.

1.3.2.1 Kikuchi Diffraction Since its discovery in 1928 by Kikuchi, in work on diffraction of cathode rays by mica, Kikuchi diffraction has been an invaluable tool for crystallographic analysis (Kikuchi, 1928; Hirsch, 1977a). Kikuchi diffraction generates a complex pattern of lines known as Kikuchi lines. The mechanism, as presented by Kikuchi, is that the incident electrons suffer very small energy loss (compared with their total energy) or zero energy loss in their passage through the crystal. Since the crystal is not quite thin, they are scattered more than once and hence in all directions. These diffusely scattered electrons will be selectively reflected by the lattice planes of mica according to Bragg conditions and cones of reflected rays are formed, intersecting the photographic plate. Since the scattering intensity decreases with increasing scattering

angle, a pair of excess and deficient lines are generated for each set of lattice planes (strictly speaking, the lines are two branches of a hyperbola). The main advantage of a Kikuchi pattern over a spot pattern is that its symmetry is precisely that of the crystal (Thomas, 1970b; Edington, 1976b).

Kikuchi diffraction can be realized via both SAED and CBED. In SAED the Kikuchi lines are diffuse, while in CBED patterns they become sharp. This is because the sampled volume in CBED is smaller, hence there is little or no strain (Williams, 1996i). The sharpening effect can be enhanced by making the incident convergent angle greater than the Bragg angle.

1.3.2.2 Crystallographic Analysis From One Kikuchi Diffraction Pattern A Kikuchi diffraction pattern provides information about crystal lattice planes along more than one zone axis, thus enabling crystallographic analysis in 3D. When all the diffraction features of interest are contained in one pattern, 3D crystallographic anlysis can readily be performed. Heimendahl *et al*. first presented a three-pole solution for such a Kikuchi pattern, which involves indexing of three line pairs and their intersections, each of which is a crystal zone axis (aslo called “pole”) (Heimendahl, 1964). Crystal orientation is obtained from the angles between these three poles and the direct beam. This method has been widely accepted and applied (Thomas, 1970a; Edington, 1976a; Williams, 1996f).

1.3.2.3 Kikuchi Analysis at Different Tilts If the reciprocal space to be explored is so large that the diffraction features of interest must be recorded on more than one plate/micrograph in a tilt series, the patterns on different plates must be properly correlated. The projection of the tilt axis on a diffraction pattern is a line common to all the patterns taken in the tilt series. Spatial relationship among the patterns can be inferred with the knowledge of the projection of this tilt axis and the goniometer readings corresponding to the specimen orientations at which the patterns were taken. As reviewed by Möck, quantitative 3D crystallographic analysis based on such Kikuchi diffraction patterns generally consists of three sequential steps, i.e., determination of the projection(s) of tilt axis/axes on diffraction patterns, establishing spatial relationships

among reciprocal lattice vectors in reciprocal space via matrix algebra and application of the spatial relationship in crystallographic analysis (Möck, 1997). Success of the related techniques has been found in the determinations of crystal orientation (Liu Q., 1990; Möck , 1991a; Möck , 1991b; Liu Q., 1995; Liu Q., 1989), orientation difference between two phases or grains (Liu Q., 1989), grain boundary parameters (Liu Q., 1992), crystallographic basis triplet (Fraundorf, 1981b), specimen orientation adjustment (Liu Q., 1989), indexing diffraction patterns (Tambuyser, 1985), phase identification (Fraundorf, 1981a) and so on.

1.3.2.4 Roadmaps for 3D Crystallographic Analysis Reicke and Sakaki adopted a different method to correlate Kikuchi diffraction patterns exposed on different plates in a tilt series (Riecke, 1959). The recording was performed in such a manner that the patterns on successive plates have some overlap. The positions of the plates were arranged through matching patterns on successive plates. This way standard Kikuchi projections, known as Kikuchi maps, for fcc, bcc and hcp crystals were constructed by Levine, Okamoto and co-workers (Levine, 1966; Okamoto, 1967; Johari, 1996). Very much like the roadmaps for a tourist, Kikuchi maps have been used to guide adjusting crystal orientation in TEM for 3D crystallographic analysis (Levine, 1966; Edington, 1976d). However, this method of correlation through matching adjascent Kikuchi patterns has some disadvantages. As pointed out by Levine *et al.*, when one tilts far away from a low index zone, matching of patterns on adjacent plates becomes more difficult (Levine, 1966). A more fundamental problem arises from the curvature of the Kikuchi lines, which is usually not noticeable on a single plate, but causes distortion of the composite Kikuchi map, particularly for orientations that are more than 20° from an axis of symmetry (Levine, 1966).

1.3.2.5 Limits of Kikuchi Diffraction for Small Crystals While Kikuchi diffraction has been an effective tool for 3D crystallographic analysis, it faces some serious problems in analyzing small crystals. As discussed in 1.3.2.1, Kikuchi diffraction is formed through either SAED or CBED, therefore general conclusions drawn about the "resolution" limit of these two techniques in 1.2.1 are applicable to Kikuchi diffraction.

Liu Q. *et al.* made some specific comments about the difficulty of Kikuchi diffraction for small crystals. When a crystal is small, it will be not thick enough to generate discernible Kikuchi pattern (Liu Q., 1989). In addition, if a Kikuchi diffraction pattern is to be used for adjusting the crystal orientation, it will be hard to keep the small crystal subjected to the beam during tilting. The loss of the crystal from the beam during tilting requires switching back to the image mode to look for the crystal, which will be tedious and time-consuming.

1.3.3. **Three-dimensional Reconstruction in Direct Space (Based on TEM Images)** Three-dimensional reconstruction techniques in direct space include stereomicroscopy and electron tomography. Neither is for crystallographic anlysis (and stereomicroscopy is not even a quantitative techqniue). However, the underlying principle of electron tomography is almost identical to that of the 3D reconstruction from Kikuchi patterns taken at different tilts, as discussed in 1.3.2.3, and that of the technique to be presented in Chapter 2. We begin from a review of stereomicroscopy as follows.

1.3.3.1 Stereomicroscopy Stereomicroscopy is a technique that provides 3D views of certain features and enables depth perception and measurement from a pair of TEM micrographs. It is a mimic or an extension of the human binocular vision of 3D objects. In the latter case, the views from two eyes are from different angles (~5º), giving rise to a parallax shift as the signal is interpreted in the human brain. Depth is gauged from the parallax shift (Williams, 1996m). Analogous to this mechanism, a pair of TEM image are taken at two different specimen orientations a few degrees apart. With a stereo viewer, the depth information is regained from the images.

Stereomicroscopy is applicable only to features showing mass-thickness or diffraction contrast. The idea originated from a technique by Lang (Lang, 1959). Lang used stereo X-ray micrograph pairs, each of which comprises one photograph taken in **g** reflection and the other in **–g** reflection, to obtain relative positions of dislocations in 3D. However, this principle to form stereo pairs can not be simply extended to electron microscopy, as the amount of tilt is only twice the Bragg angle for **g**, which is on the order of 0.1° and too small compared with a tilt of at least 5° that is necessary to produce

a reasonable stereoscopic effect. To avoid this problem, Basinski, in studying dislocation networks generated by deformation at liquid He temperature in a Cu crystal, excited the same **g** reflection in a stereo pair through tilting along the corresponding lattice plane, i.e., the tilt axis is parallel to **g (**Basinski, 1962). This way stereo pairs of dislocation networks were successfully produced with tilts of up to about 20°, and very strong stereoscopic effect was obtained. This approach has been widely accepted and applied as a standard (Thomas, 1970c; Edington, 1976c; Hirsch, 1977d). Kikuchi maps are particularly useful in realizing the right diffraction condition, since both the sense and the approximate value of tilt can be determined from the maps.

In their stereomicroscopy analysis of spatial distribution of voids produced in nickel/copper during ion irradiation, Chen *et al.* measured the depths of individual voids approximately from stereo pairs taken 6° apart (Chen, 1972). The depth measurement, however, was subject to an uncertainty of ±20%. Maher *et al.* used stereo pairs to determine the 'sign' of small point defect clusters (interstitial or vacancy) in neutron irradiated molybdenum foils (Maher, 1971). In addition to materials science, stereomicroscopy has been applied to biology in studying cell-wall structure and deposition, connective tissues and biological thin sections (Hudson, 1973; Cox, 1973; Glauer, 1973; Willis, 1973). As a closing remark, stereomicroscopy is not an adequate technique for solving a structure, since it does not reproduce structures in a quantitative form. Information from pairs of corresponding points in a stereo pair is combined only visually. Quantitative stereo measurement is treated in stereology (Russ, 1990). Algorithms for applying stereology to the mapping of lateral tip forces in scanning tunneling microscopy were developed at UM-St. Louis by Shen (Shen, 1997).

1.3.3.2 Electron Tomography Electron tomography is a general term for any technique that employs TEM to collect projections of an object so as to reconstruct the object in its entirety (Frank, 1992a). The first consideration of the general 3D reconstruction of an object from its projections can be traced back to 1917 (Randon, 1917). DeRosier and Klug introduced this technique into electron microscopy, and formulated the general principles for object reconstruction (DeRosier, 1968). The first formal solution of this problem was given in terms of Fourier transforms by Crowther *et*

al. (Crowther, 1971). In the underlying principle, a projection yields a single central plane of the examined object's 3D Fourier transform. The Fourier transform, an alternative representation of the object, breaks down the object's density distribution into sinusoidal waves. Projections of the object along different viewing directions are obtained by tilting the object, then used to perform Fourier synthesis, after which the 3D structure of the object can be built up. The number of projections needed to fill Fourier space depends on both the size of the particle and the desired resolution. Intrinsic symmetry of an object generally reduces the total amount of necessary projections and the maximum tilt angle required, since different orientations of the object present identical projections (Frank, 1992b; DeRosier, 1968; Hoppe, 1976). Utilizing its high rotational symmetry, DeRosier and Klug successfully demonstrated the 3D reconstruction of a phage tail from only one electron micrograph (DeRosier, 1968). (This is similar to the 3D reconstruction of crystal lattices, since they comprise just a different type of structure symmetry for which often only two projections containing three linearly independent reciprocal lattice vectors are sufficient to infer the whole crystal lattice) (Fraundorf, 1981a).

There are two methods of data acquisition: either by imaging the same object at different tilts or by imaging different copies of the object occurring in different orientations (provided the structure is reproducible) (Frank, 1989). The second method offers the advantage of less radiation damage to any single specimen. Based on the theories developed, electron tomography has found success in the studies of both symmetric and asymmetric biological objects (Frank, 1992d; Frank, 1986; DeRosier, 1968; Crowther, 1971; Frank, 1989; Herman, 1979; Hoppe, 1981; Lewitt, 1978; Henderson, 1975).

1.3.4. <u>Other TEM Techniques Capable of Retrieving 3D Information</u> Other techniques are capable of retrieving 3D information. These techniques include electron holography. A brief introduction to electron holography is given as follows.

Electron holography was proposed as a method of interference imaging by Gabor in the late 1940s and strongly pursued after introduction of FEGTEM in late 1970s (Gabor, 1948; Gabor, 1949). In essence it employs an electron biprism to allow

interference between an object wave and a reference wave. The interferogram is then processed to yield separate amplitude and phase images (Tonomura, 1995). Twenty modes have been described and success has been found in the determinations of shape and thickness, magnetization measurements, imaging magnetic lines of force and so on (Cowley, 1992; Beeli, 1997; Wang, 1997).

1.4. SMALLER CRYSTALS IN 3D: LOCATION AND PERIODICITY FROM IMAGES

From the above discussion, it becomes obvious that 3D information can be acquired from projections at two tilts. However, when analyzing tiny crystals (more and more common in many materials fields), a decrease in the size of the region analyzed is desirable.

1.4.1. The Scaling-down Trend In recent years, tremendous interest has been generated in the fabrication and characterization of submicrometer and even nanoscale structures in many fields, such as device manufacturing and nanocrystalline materials.

In device manufacturing, there exists a drive toward smaller, faster and more sensitive and reliable systems. This is evident from the fact that the size of a single transistor in semiconductor devices has evolved from millimeters to 0.18 μm, and is currently progressing toward 0.15 μm (Wauters, 1998). The "roadmap" for the Si ultralarge-scale-integration circuit (ULSI) industry targets the production-level realization of a 70 nm minimum feature size for the year 2010 (Hasegawa, 2000). Similar trends exist in compound semiconductor device manufacturing. The relentless miniaturization of GaAs- and InP-based heterostructure devices has brought about ultrahigh speeds, approaching the tHz range with ultralow power consumption. In the disc drive industry, areal storage density has been increasing at a remarkable rate of 60% per year for about a decade, owing to the improvements made in the head designs (KnowledgeTek, 1999). Anisotropic magnetoresistive (AMR) heads dominated the magnetic data storage systems in the 90's, but are now being replaced by giant-magnetoresistive (GMR) heads, since a GMR head has a smaller size and offers about

five times as high a sensitivity, i.e., $\triangle R/R \cong 20\%$ (Baibich, 1988; White, 1994; Mallinson, 1996). The upper limit of areal density demonstrated with an AMR head is 5 Gbits/in^2 by IBM, while that with a GMR head reached 16Gbits/in^2 by Seagate (Tsang, 1997). In nanocrytsalline materials, novel properties in the areas of magnetics, catalysis, mechanics and optics have also been achieved through structural control down to the atomic scale (Kung, 1999; Ghosh, 1999; Sellmyer, 1999; Miura, 1999; Kim, 1997).

1.4.2. <u>A Possible Solution: Direct Space Crystallography</u> In response to the need to characterize structures on small size scales, a call for analytical techniques of higher spatial resolution and providing more complete information very naturally arises. In analyzing nanocrystals, one possible approach is to combine the high-resolving power of HRTEM with the specimen orientation adjustment function of a TEM, to resolve the (nano)crystal lattice structure in 3D from lattice images taken at different tilts.

In HRTEM arbitrarily small crystals (even individual atoms) can be examined. Hence the "sampled volume" limitation of diffraction does not apply. But HRTEM, unlike diffraction, can only image the largest lattice spacings, hence a brief introduction to "point-resolution" in an HRTEM follows.

In HRTEM, spherical aberration and defocus both contribute to the phase shift of an objective electron wave (relative to the reference wave) in the image. For a weak-phase object where the amplitude of a transmitted wave function is linearly related to the projected potential, Schertzer in 1949 showed that the contrast transfer could be optimized by balancing the effect of spherical aberration against a particular negative value of focus, i.e., defocus. At this defocus setting, all the objective waves are transferred with nearly constant phase out to the lowest filtered out spatial frequency, i.e., the first "cross-over" or the first zero in the contrast transfer function, and this flat-response regime becomes almost as wide as possible (Spence, 1988a; Williams, 1996k). For all objective waves with spatial frequencies in this flat-response regime, the interpretation can be directly made without taking into account contrast transfer reversal. The distance corresponding to this first cross-over in the contrast transfer function, denoted as r_{Sch}, is defined as the point-resolution of an HRTEM.

HRTEM has the advantage over diffraction that crystal structure and crystal shape/location information are incorporated in the same image. If there is amorphous material in the field of view, information on instrument response may be found in the image, thanks to an elegant theory of electron phase contrast transfer.

Fraundorf described the prospects to determine the 3D lattice parameters of nanocrystals from HRTEM images taken at different crystal orientations (Fraundorf, 1987). The reciprocal lattice vectors were to be acquired in the form of lattice fringe sets through images taken along two or three directions in a tilt series. The TEM must have a high enough point resolution, as well as a large enough tilt capability, in order to resolve the lattice plane sets of interest, and reach the desired viewing directions along which the lattice plane sets can be imaged. Once the power spectra of the lattice images are obtained, and lattice fringe vectors[†] measured, the data processing and subsequent crystallographic analysis would be identical to those described in his earlier work on stereo analysis of single crystal electron diffraction patterns (Fraundorf, 1981a). The difference only lies in the data acquisition.

Through electron diffraction, reciprocal lattice vectors with very large magnitudes can be detected. This not only offers a wide range of data to choose, but also imposes less constraint on the TEM tilt capability, as high index zones are very much closely-spaced and also offer recordable reciprocal lattice vectors. Through HRTEM, however, the magnitudes of easily interpretable lattice fringe vectors only extend to the first cross-over in the contrast transfer function (Spence, 1988a; Williams, 1996b). In direct space, this means only lattice plane sets with spacings larger than the point resolution of the TEM are easily considered. In addition, only low index zones can be chosen since they are the viewing directions along which lattice plane sets with large spacings are available for HRTEM. Since low-index zones are widely separated, the tilt range of the TEM must be accordingly wider.

[†] A lattice fringe vector associated with a set of lattice fringes is a vector whose magnitude is equal to the inverse of the spacing of the fringes, and whose direction is along the normal to the fringes. It can be measured from the power spectrum of an HRTEM image showing the fringes. It only equals to the reciprocal lattice vector corresponding to the lattice plane set when this lattice plane set is in exact Bragg condition.

In summary, when resolving the 3D crystal lattice structures from direct space images, careful consideration must be given to choosing the appropriate imaging directions in order to acquire interpretable reciprocal lattice vectors. Consequently, data acquisition protocols are important, and this will be a main focus in the development of techniques for direct space crystallography of nanocrystals via HRTEM.

1.5. CONTENT AND STRUCTURE OF THE THESIS

The content and structure of this thesis can easily be understood with the aid of the visibility band and the visibility band map shown on the front page. "Visibility" here means the visibility of fringes from a set of lattice planes of a (nano)crystal in HRTEM images. When the electron beam is incident on the lattice plane set and satisfies the Bragg condition, the lattice fringes are visible. The finite size of the (nano)crystal results in relaxation of that Bragg condition. This will enable lattice fringes to be produced in the images, for a finite range of incident angles of the electron beam. If the (nano)crystal is spherical, from the rotation symmetry of the electron beam around the lattice plane normal, it can be concluded that the region of fringe visibility will be distributed in a band running parallel to the lattice plane set. The ensemble of the visibility bands of the (nano)crystal forms the visibility band map, as shown on the front page.

Chapter 2 concerns direction of the electron beam along one cross-section of two bands and then somewhere along the middle of another band, so that three sets of lattice fringes can be obtained to perform 3D analysis. Chapter 3 involves determining whether the electron beam lies in a band or out of it after tilting the crystal, so that whether the corresponding lattice fringes are visible or not after tilt can be predicted. Part of Chapter 4 in principle focuses on calculating the solid angle subtended by a cross-section of visibility bands, which is proportional to the probability of obtaining the corresponding zone images from a randomly oriented nanocrystal. However, what has been done in this thesis is an approximation, since the exact solution has not been obtained yet. The wider a visibility band, the higher is the uncertainty of the corresponding reciprocal lattice vector. Quantifying such an uncertainty forms the second half of Chapter 4.

2. CRYSTAL LATTICE PARAMETERS FROM LATTICE IMAGES AT TWO TILTS

2.1. INTRODUCTION

Various techniques have been developed to infer the 3D relationship of reciprocal lattice vectors from Kikuchi diffraction patterns taken at different specimen orientations. Such relationships have been applied in the determinations of crystal orientation (Liu Q., 1990; Liu Q., 1989), grain boundary parameters (Liu Q., 1992), and crystallographic basis triplet (Fraundorf, 1981b). Other applications include specimen orientation adjustment (Liu Q., 1989), diffraction indexing (Tambuyser, 1985), and phase identification (Fraundorf, 1981a). The basic approach consists of 3 parts: determining the projection of the tilt axis on electron diffraction patterns of the working camera constant, inferring the relative positions of the diffraction spots in the reciprocal space, and finally, applying the spatial relationship among the reciprocal lattice spots to crystallographic analysis (Möck, 1997). When the crystal size is in the nano-meter scale, probes in conventional CBED can no longer extract lattice structure information specific to individual nano-crystals. Recent development in Field Emission Gun (FEG) TEM makes it possible to achieve nano-diffraction (Cowley, 1981; Cowley, 1996). This requires UHV technology, which is expensive and a much higher level of operator competence is needed (Williams, 1996a). Another drawback of nano-diffraction is the high current dosage due to the spatial confinement of the electron probe. Unless the crystal is very robust, it'll suffer severe radiation damage during examination. Lastly, of course, diffraction by definition contains no information of crystal location. A need thus arises for analytical microscopy techniques with high spatial resolution, lower radiation damage, and a larger base of installed instruments. Inferring the 3D lattice of a crystal from HRTEM images is the solution discussed here.

Due to the transmitted nature of the electron beam, a TEM image presents 3D information averaged throughout the thickness of the specimen on each micrograph. In order to overcome this limitation, techniques for acquiring the 3D information from TEM

images have been developed. These include stereomicroscopy and electron tomography (Basinski, 1962; Hirsch, 1977d; Tambuyser, 1984; Frank, 1986; DeRosier, 1968). However, stereomicroscopy only provides visual 3D views of features showing mass-thickness or diffraction contrast and is not a quantitative technique; while electron tomography is for the reconstruction of an object in its entirety. Neither is for crystallographic analysis.

With the availability of HRTEM, prospects of 3D reconstruction for non-periodic structures, as well as those for finding the 3D lattice parameters of nano-crystals from lattice images taken at different specimen orientations, were discussed (Hoppe, 1977; Fraundorf, 1987). In the latter case, the core instrumentation requirement consists of a TEM capable of delivering contrast on the spatial frequencies of interest in the specimen, and a tilt range of more than 30° over a single tilt axis. For crystals with unit cell sizes of ~4 Å and larger, a conventional high-resolution TEM with continuous contrast transfer to spatial frequencies beyond 1/(2 Å) is well capable of such tasks. Here we describe the development of such a technique and its application to the analysis of a nano-crystal using a Philips EM430 ST TEM. Appropriately orienting a small cell crystal so as to reveal its lattice structure in HRTEM images is a key part of the experimental design.

As a prerequisite for 3D reconstruction of crystal lattices from lattice images taken at different tilts, the projection of the (effective) tilt axis on images must be known. Such a projection is similarly crucial in the 3D reconstruction of crystal lattices from electron diffraction patterns, and the interiors of objects from images in electron tomography (Frank, 1992c; Frank, 1986; DeRosier, 1968; Möck, 1997; Liu Q., 1990; Möck, 1991a; Möck, 1991b; Liu Q., 1992; Fraundorf, 1981b; Liu Q., 1989; Fraundorf, 1981a). In techniques of 3D electron diffraction crystallography, the projection of a tilt axis is inferred from the “Kikuchi pattern moving direction” while a thick crystal is tilted. That in electron tomography involves either fiducial marker or cross-correlation function (Lawrence, 1992; Frank, 1992). An alternative marker-free scheme has been developed based on the fact that all projections of a single axis tilt series share a common line in Fourier space (Liu Y., 1995). This approach, however, requires the specimen to be freely-supported and its boundary sharply defined, and is noise-sensitive. In some other applications a side-entry tilt axis is assumed to be parallel to the specimen holder rod and

thus the tilt axis projection on images is determined by translating the specimen (Tambuyser, 1984; Liu Q., 1989; Fraundorf, 1987; Williams, 1996d). This is valid so long as the transverse backlash is negligible compared with the longitudinal translation seen in an image. This is unlikely at high magnifications, however. Another method for axis determination on ~2K magnification images is from the mirror-symmetry between a pair of images of a plankton tilted 180^o apart using a 360^o-tilt specimen holder (Zhang, 1998).

Nonetheless these image-based methods have been applied at low to medium magnifications (Amos, 1982). As the secondary focus of this paper, we will also present a method for determining the projection of a tilt axis on HRTEM images.

2.2. STRATEGY: TILT PROTOCOLS TO EXPLOIT CRYSTAL SYMMETRY

We can take advantage of the symmetry of crystals (and quasicrystals) by noting that generally 3 non-coplanar reciprocal lattice vectors seen along 2 different zone axes are sufficient for inferring a subset of the 3D reciprocal lattice of a single crystal. Often these are adequate to infer the whole lattice. The goal of the experimental design is thus to look for 3 reciprocal lattice vectors within the first contrast transfer function pass-band, and present along two zones whose angular distance is within the tilt limit of a TEM. Images with point resolution smaller than the analyzed spacings are requested, to lessen chances of missing comparable (or larger) spacings in the exit-surface wavefield. In tilting from one zone to another, the crystal must be specially oriented so that the lattice planes parallel to both desired zones are perpendicular to the tilt axis. With the above consideration of both the limited tilt range typical for an HRTEM and the point resolution taken into account, the possibilities to resolve the lattice structures of the simplest and most popular lattices are limited and can be enumerated. For each of these possibilities, there is a corresponding data acquisition protocol. Each protocol involves tilting between two low-index zones, along which altogether 3 targeted reciprocal lattice vectors can be acquired. Before treating the theory more generally, we illustrate with an example for WC_{1-x}, which is given as follows.

WC_{1-x} has an f.c.c. lattice with a = 4.248 Å (Krainer, 1967; *JCPDS-ICDD*; Qin, 1998). For a WC_{1-x} nano-crystal, the 3 targeted reciprocal lattice vectors are $\mathbf{g}_{200}$ and $\mathbf{g}_{020}$ along the [001] zone, and $\mathbf{g}_{1,1,-1}$ along the [112] zone. The corresponding lattice spacings are $d_{200} = d_{020} = 2.124$ Å and $d_{1,1,-1} = 2.45$ Å. The angle between the two zones is 35.3^o. The two specimen orientations can therefore be set at the two of ($\theta_1=15.0^o$, $\theta_2=9.7^o$) and ($\theta_1=-15.0^o$, $\theta_2=-9.7^o$), which are 35.3^o apart (Selby, 1972), where θ_1 and θ_2 are goniometer readings in a Gatan double tilt holder. The effective tilt axis for such a double tilt runs perpendicular to the electron beam and hence parallel to the micrographs in this case. Its azimuth is 123.5^o on the xy plane of the coordinate system used (The azimuth of an effective tilt axis can be calculated using (2-7), and the coordinate system will be discussed in 2.6.1). The (2, -2, 0) lattice planes are parallel to the two zones. Therefore the tilt must be along the (2, -2, 0) lattice planes, i.e., $\mathbf{g}_{2,-2,0} // T_{eff}$, where T_{eff} denotes the effective tilt axis. This tilt protocol holds valid for any f.c.c. lattice with a lattice constant greater than twice the point resolution of the TEM, and is given in Table 2-1. It can readily be obtained from the visibility band map on the front page, where the [001] and [112] zone axes (as marked) are separated by 35.26°. The expected experimental result is illustrated in Figure 2-1. In order to use appropriate protocols, "first hand" data about the crystal phase, usually from chemical composition analysis, must be obtained to provide reasonable guess of the lattice structure of the crystal. HRTEM image(s) along at least one low index zone with cross lattice fringes can further narrow down the scope of candidate lattice structures.

Table 2-1. A data acquisition protocol to determine the 3D lattice of an f.c.c crystal with a lattice constant of $a>2r_{Sch}$.

Zone	[001]	[112]
Lattice Fringes Vectors	(020) (200)	(1, 1, -1)
Tilt Along Lattice Planes	(2, -2, 0)	
Tilt	35.3^o	

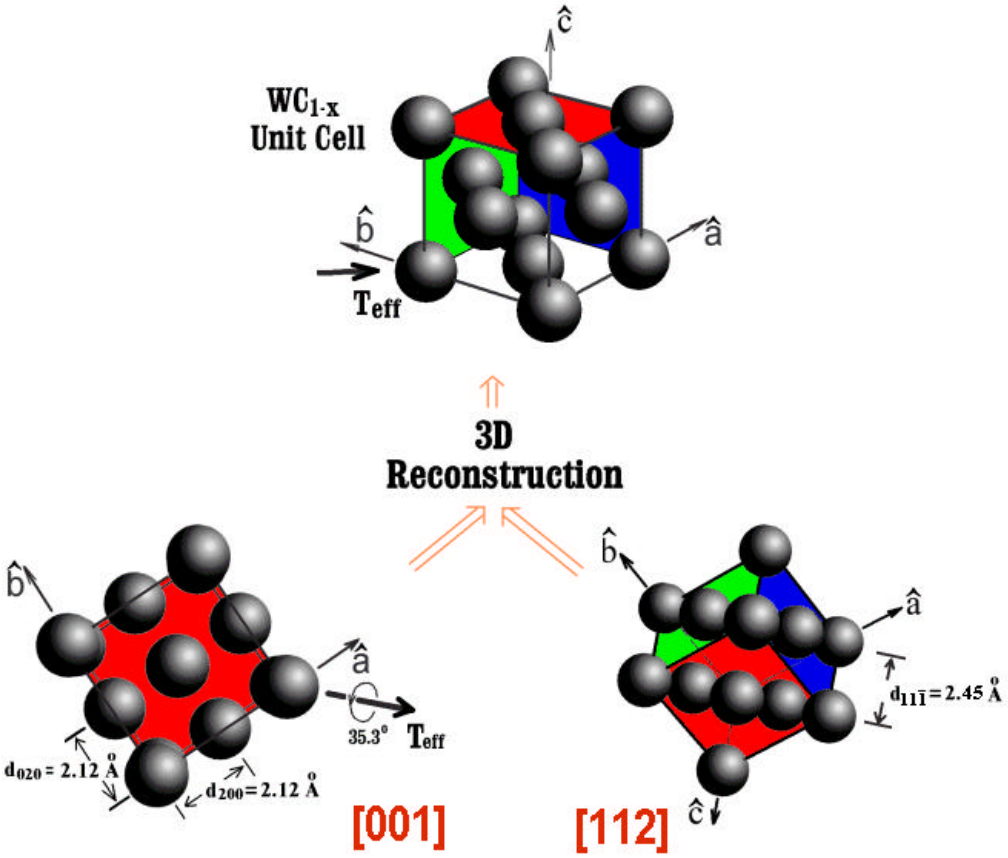

Figure 2-1. Schematic illustrating application of the f.c.c. stereo lattice tilt protocol of to a nano-crystal in a tungsten-carbide thin film. Models show tungsten atoms only. The 1st tilt was around $-T_2$ by 19.4°, the 2nd tilt, $-T_1$ by 30.0°, where T_1 and T_2 are the side-entry goniometer tilt axis and the 2nd tilt axis, respectively.

General theories to establish data acquisition protocols for any crystal system, as well as some protocols for f.c.c., b.c.c. and s.c. lattices have been presented elsewhere (Qin, 2000a). Some of these protocols are illustrated in Figure 2-2. The f.c.c. protocol specified in Table 2-1 and illustrated in Figure 2-1 is given as the 2nd entry in the first column in Figure 2-2. In addition, two tilt protocols with the lowest amount of tilts for graphite as an example of hexagonal lattice is given in Table 2-2. It can be seen that the amount of tilts are much less that those required for f.c.c. and b.c.c. lattices.

Table 2-2. Two data acquisition protocols for graphite lattice with a TEM point resolution of 1.9 Å.

Protocol	1		2	
	1st Zone	2nd Zone	1st Zone	2nd Zone
	[1, -1, 1]	[1, -1, 2]	[101]	[1, -2, 2]
Lattice Spacing to be Resolved (Å)	$d_{1, 0, -1}$ = 2.04 $d_{0, 1, 1}$= 2.04	$d_{1, -1, -1}$=2.04	$d_{1, 0, -1}$ = 2.04 $d_{1, -1, -1}$= 2.04	$d_{0, 1, 1}$ = 2.04
Tilt Along Lattice Planes	(1, 1, 0)		(2, -1, -2)	
Amount of Tilt	14.8°		16.6°	

2.3. EXPERIMENTAL SETUP

There are different subjects in this section. They include the instruments, calibration of the microscope, setting-up the coordinate system, tilting the sample, and sample preparation.

2.3.1. Instruments The Philips EM430 ST TEM used provides continuous contrast transfer to 1/(1.9 Å) at the Scherzer defocus, and is equipped with a ±15° side-entry goniometer specimen stage. A Gatan double tilt holder enables ±10° tilt around the second tilt axis. The largest orientation difference which can be achieved using this double tilt holder in the microscope is therefore 35.6° (Selby, 1972).

2.3.2. **Calibrating the Microscope: Determination of the Projection of the Tilt Axis on HRTEM Images** In order to establish spatial relationship of the lattice fringe vectors, which are determined from the images taken at different specimen orientations via tilting, the orientation of the tilt axis with respect to the images must be known. A tilt axis direction is defined such that a tilt around it, by the right hand rule, corresponds to an increase in the goniometer reading. In a single tilt, the tilt axis is

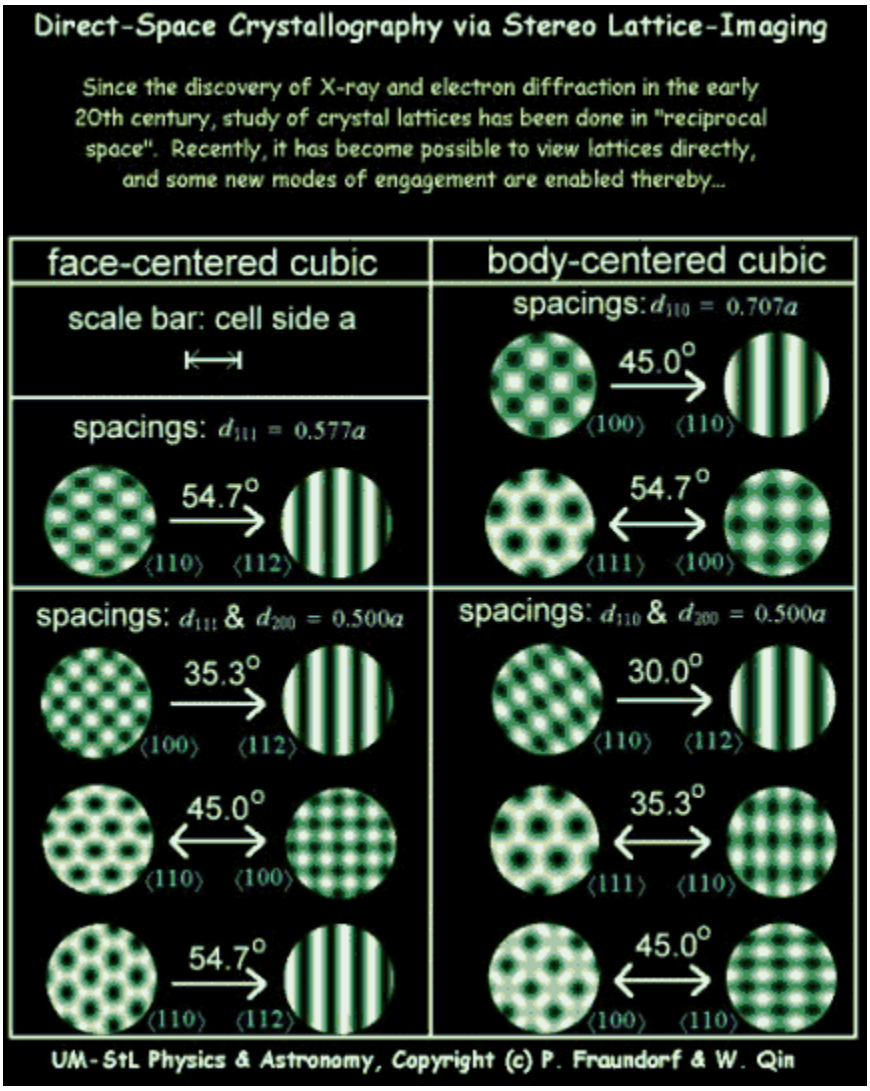

Figure 2-2. Illustration of all the protocols to determine the lattice parameters of f.c.c. and b.c.c. crystals from a pair of lattice images, given an ability to image lattice spacings down to half the unit cell side, and a tilt range of less than 60°. The two zone images in each protocol are labeled with their zone indices. The arrow for each protocol indicates the direction of tilt, which is perpendicular to the tilt axis. The double arrow in a protocol indicates that both zone images show cross-fringes, hence it is possible to determine the direction of tilt from either zone images, and tilting can be performed in either direction as indicated by the double arrow.

perpendicular to the electron beam and parallel to the micrographs. So it is with the effective tilt axis of a double tilt holder, provided the two specimen orientations are symmetric about the untilted position. We limit our discussion to double tilts falling into this category.

In the following discussion, we use T_1 and T_2 to denote the side entry goniometer tilt axis, and the second tilt axis in the Gatan double tilt holder, respectively, and θ_i (i =1 ~ 2) to denote the goniometer reading for a tilt around T_i. Determination of the projection of T_1 on HRTEM images was performed in 2 steps. First the projection of T_1 on an electron diffraction pattern with a certain camera length was determined. When the specimen was tilted about T_1, the Kikuchi pattern motion of a Si<110> specimen was recorded on either one micrograph through a double exposure, or two micrographs. Another alternative is to use a tilt-rotate holder to rotate the specimen at zero side-entry goniometer tilt, i.e., with $\theta_1=0^o$, until one Kikuchi line is parallel to the Kikuchi pattern moving direction. The projection of T_1 is parallel to the cross-product of the electron beam direction and the Kikuchi pattern moving direction. The relationship among the three directions is shown in Figure 2-3.

Secondly, an electron diffraction pattern with the same camera length and a HRTEM image at the desired working magnification, both from the same region in the above Si specimen, are taken. The rotation angle between the electron diffraction pattern and the HRTEM image allows determining the projection of T_1 on the HRTEM images (This method to determine the projection of a tilt axis on HRTEM images has not been seen in literatures). In our experiment, this rotation angle is obtained from that between the (2, -2, 0) diffraction spot in the diffraction pattern and the same (2, -2, 0) spot in the power spectrum of the HRTEM image. A 180° uncertainty will remain (Williams, 1996c; Beeston, 1972). This uncertainty can be resolved by observing the specimen moving direction in HRTEM images while the specimen is translated along T_1. Another traditional method to determine the rotation of an image at a certain magnification with respect to an electron diffraction pattern at a certain camera length is through a double-exposure which records both the image and the electron diffraction pattern of MoO_3 on one micrograph (Beeston, 1972). This also has a 180° uncertainty, and works better at lower magnifications given the usual size of the MoO_3 crystals.

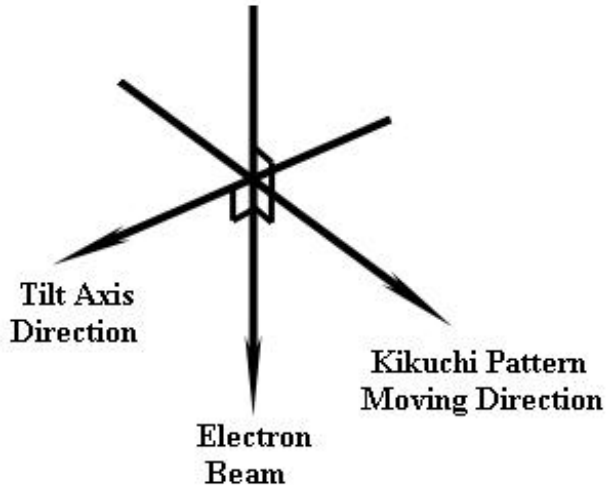

Figure 2-3. The relationship among the projection of a tilt axis on an electron diffraction, the electron beam direction and the Kikuchi pattern motion direction. The projection of the tilt axis is along the cross-product of the electron beam direction and the Kikuchi pattern motion direction.

The projection of T_2 on HRTEM images can be determined using the same method. In our work it is assumed to be perpendicular to that of T_1. This is consistent with the design of the holder, and will be confirmed by the conservation of lattice fringe vectors that are prallel to the effective tilt axis after a double tilt, which will be discussed in 3.4.1. A different approach to determine the projection of T_1 on TEM images (most were at low to medium magnifications) is by translating the specimen along the direction of T_1 (Liu Q.,1989 ; Tambuyser, 1985; Tambuyser, 1984; Fraundorf, 1987; Williams, 1996e) . The assumption held is that the longitudinal geometric axis of the specimen holder is coincident with T_1, which is valid when the traverse backlash, small and negligible compared with the longitudinal translation at low to medium magnifications, is not a limiting factor. It was found in our experiment that, however, at the high magnification of 700K, the longitudinal specimen translation direction deviates from that of the projection of T_1 by as much as 20.0^o.

A micrograph is placed in front of the microscope operator, emulsion side facing up. The direction from operator left to the right is defined as the zero degree azimuth, with azimuth increasing in the counterclockwise direction. In this case the projection of

T_1 on electron diffraction patterns of the camera length of 1200 mm is along –114.0°, as shown in Figure 2-4. The rotation angle between electron diffraction patterns at this camera length and 700K HRTEM images was determined to be –42.9°, as shown in Figure 2-5. Therefore the projection of T_1 on 700K HRTEM images is along -156.9^{o}. The projection of the second tilt axis, T_2, on 700K HRTEM images is orthorgonal, along 113.1^{o}. The projections of the tilt axes are shown in Figure 2-6.

2.3.3. <u>The Coordinate System Set-up</u> A coordinate system for measuring lattice fringe vectors from the power spectra of 700K HRTEM images is fixed to the microscope column. The y and z directions are defined to be along $-T_1$ and the electron beam direction, respectively, as shown in Figure 2-7.

The projection of this coordinate system on the power spectrum of a 700K HRTEM image is shown in Figure 2-8. Any future azimuth will be expressed as measured in the xy plane of this coordinate system.

2.3.4. <u>Double Tilting</u> The specimen was first tilted about T_2 to $\theta_2 = 9.7^{o}$ while θ_1 remained at 0^{o}, made eucentric by adjusting specimen hight, and then tilted about T_1 to $\theta_1=15.0^{o}$. The first HRTEM image was taken at this specimen orientation of ($\theta_1=15^{o}$, $\theta_2=9.7^{o}$). A similar sequence was applied to take the second HRTEM image at the second specimen orientation of ($\theta_1=-15^{o}$, $\theta_2=-9.7^{o}$).

2.3.5. <u>Sample Preparation</u> The tungsten carbide thin film was deposited by PECVD on glass substrates by introducing a gaseous mixture of tungsten hexacarbonyl and hydrogen into a RF-induced plasma reactor at a substrate temperature of 330^{o}C (Qin,1998). The specimen was disk-cut, abraded from the glass substrate side and dimpled by a Gatan Model 601 Disk Cutter, a South Bay Technology Model 900 Grinder and a Gatan Model 656 Precision Dimpler, respectively. The specimen was finally argon

Figure 2-4. Determination of the projection of the side-entry goniometer tilt axis on electron diffraction patterns with a camera length of 1200 mm. The electron diffraction pattern is that of a Si <001> specimen. The specimen was rotated (at zero side-entry goniometer tilt) to have the Kikuchi pattern moving direction parallel to the Si (004) band, then tilted around T_1. The Kikuchi pattern moving direction is measured as along -24.0^o. The projection of T_1 is thus along $-24.0^o - 90^o = -114.0^o$.

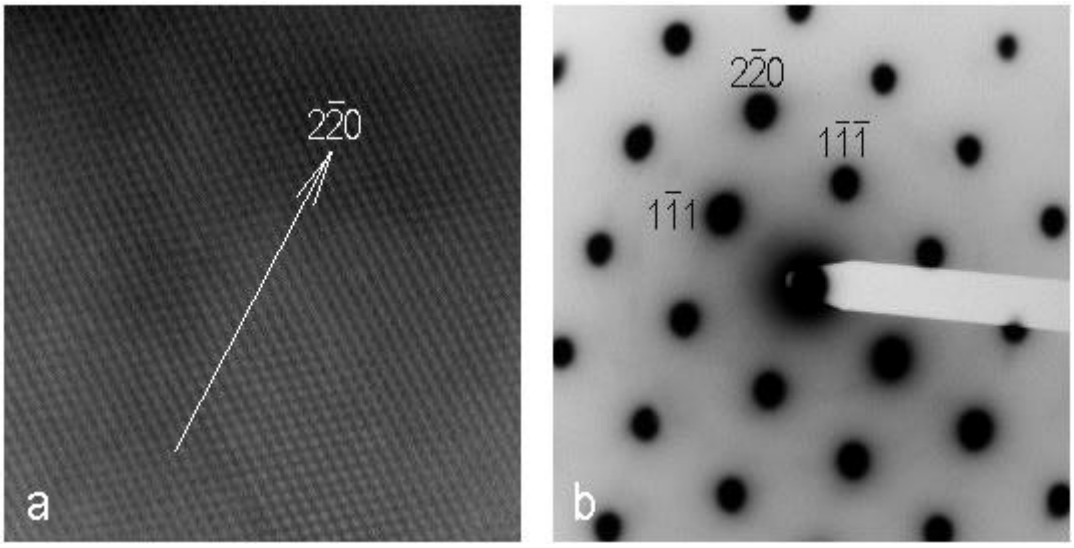

Figure 2-5. Determination of the rotation between a 700K HRTEM image and an electron diffraction pattern of a camera length of 1200 mm. The (a) inset is a 700K HRTEM image of a silicon <110> specimen. The (b) inset is an electron diffraction pattern of a camera length of 1200 mm taken from the same region in the Si <110> specimen as shown in the (a) inset. The rotation of -42.9^o between (b) and (a) was obtained from the angle between the (2, -2, 0) reciprocal lattice vectors in them.

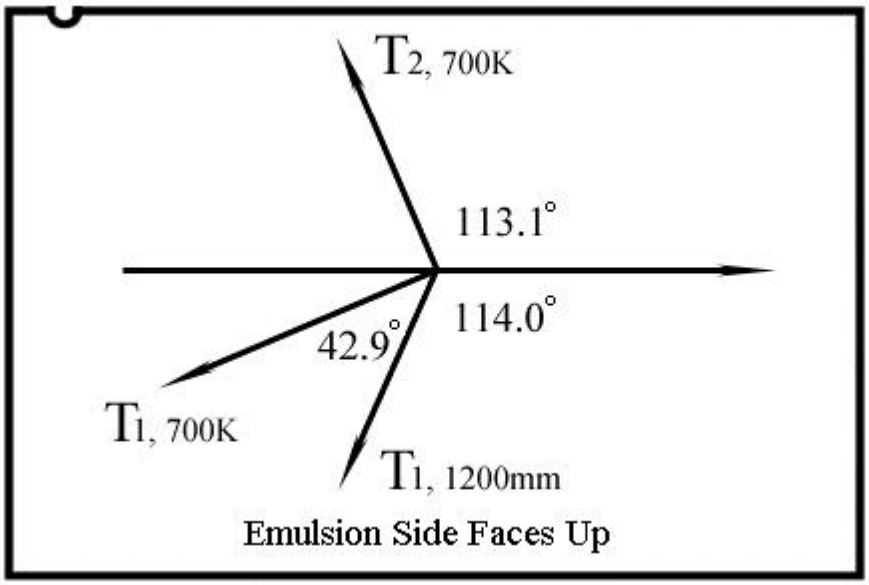

Figure 2-6. The projections of the side-entry goniometer tilt axis on electron diffraction patterns of a camera length of 1200 mm (denoted as $T_{1,\ 1200\ mm}$) and on 700K HRTEM images (denoted as $T_{1,\ 700K}$), and that of the second tilt axis on 700K HRTEM images (denoted as $T_{2,\ 700K}$).

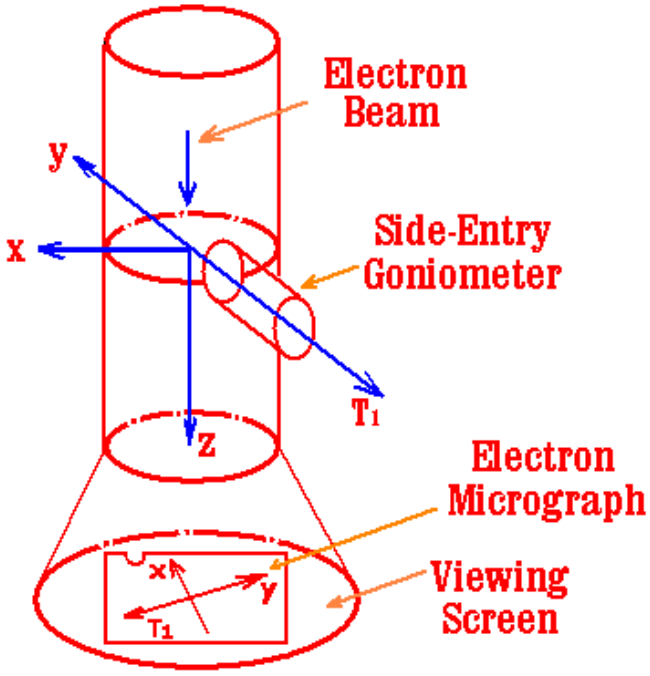

Figure 2-7. Schematic illustrating a coordinate system for measuring reciprocal lattice vectors based on their counterparts acquired along different crystal orientaitons. The y and z directions are defined to be along $-T_1$ and the electron beam direction, respectively.

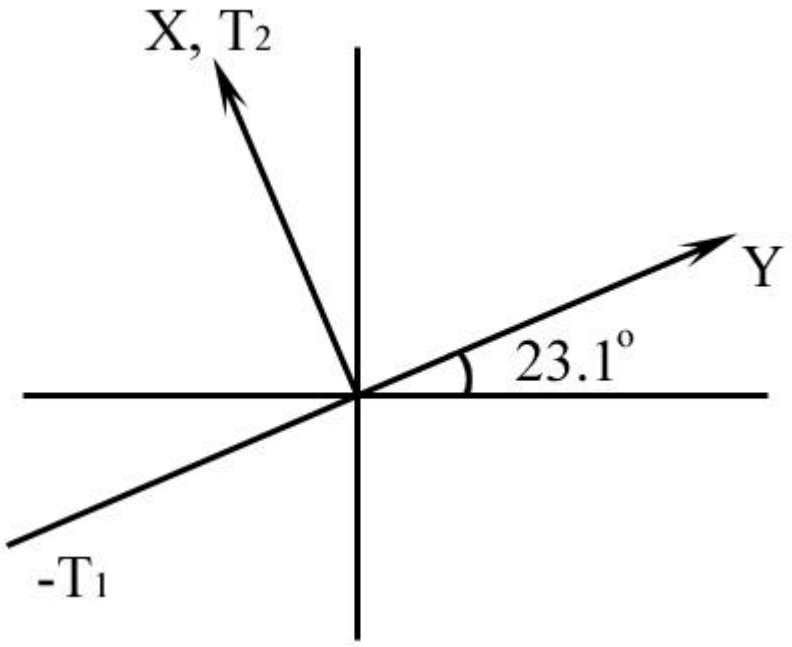

Figure 2-8. Projection of the coordinate system for measuring reciprocal lattice vectors on 700K HRTEM images.

ion-milled by a Gatan DuoMill for about 5 hours to perforation prior to the TEM study, at an incidence angle of 3°.

2.4. CALCULATION

2.4.1. Determining Reciprocal Lattice Vectors When the specimen is at the orientation of ($\theta_1=0^o$, $\theta_2=0^o$), a reciprocal lattice vector is expressed as g in our chosen coordinate system. This reciprocal lattice vector is then brought to Bragg condition by double tilting in a sequence of $T_2(\theta_2)$, $T_1(\theta_1)$, after which g becomes g_m (subscript m denotes that g_m is measured from the power spectrum of the image recorded on a micrograph). As shown here, $T_i(\theta_i)$ (i =1 ~ 2) denotes a rotation about T_i by an amont of θ_i. Therefore the following relation can be obtained

$$\mathbf{g}_m = T_1(\theta_1)\, T_2(\theta_2)\, \mathbf{g}, \tag{2-1}$$

where

$$\mathbf{g}_{mx} = \mathbf{g}\cos(\varphi),\ \mathbf{g}_{my} = \mathbf{g}\sin(\varphi),\ \mathbf{g}_{mz}=0. \tag{2-2}$$

Multiplying both sides of (2-1) by $T_1^{-1}(\theta_1)\, T_2^{-1}(\theta_2)$ leads to the following equation of

$$\mathbf{g} = T_1^{-1}(\theta_1)\, T_2^{-1}(\theta_2) = A(\theta_1, \theta_2)\, \mathbf{g}_m, \tag{2-3}$$

where $T_i^{-1}(\theta_i)$ (i = 1, 2) denotes the inverse of $T_i(\theta_i)$, and hence we obtain

$$T_2^{-1}(t_2) = \begin{bmatrix} 1 & 0 & 0 \\ 0 & \cos(q_2) & \sin(q_2) \\ 0 & -\sin(q_2) & \cos(q_2) \end{bmatrix},$$

$$T_1^{-2}(t_1) = \begin{bmatrix} \cos(q_1) & 0 & \sin(q_1) \\ 0 & 1 & 0 \\ -\sin(q_1) & 0 & \cos(q_1) \end{bmatrix}, \text{ and}$$

$$A(t_1, t_2) = \begin{bmatrix} \cos(q_1) & 0 & \sin(q_1) \\ -\sin(q_2)\sin(q_1) & \cos(q_2) & \sin(q_2)\cos(q_1) \\ -\cos(q_2)\sin(q_1) & -\sin(q_2) & \cos(q_2)\cos(q_1) \end{bmatrix}. \tag{2-4}$$

It is the components of the reciprocal lattice vector **g** associated with the crystal at the specimen orientation of zero tilt, i.e., (θ_1=0^o, θ_2=0^o), that serve to establish the spatial relationship among reciprocal lattice vectors on different micrographs. Subsequent determination of the 3D lattice, and other crystallographic analyses, can be performed.

2.4.2. <u>Calculating the Lattice Parameters</u> Lattice parameters are calculated based on the method adopted in an earlier work (Fraundorf, 1981a). First the primitive reciprocal basis triplet, a*, b* and c*, are selected from a list of integral linear combinations of the reciprocal lattice vectors. Such a basis triplet must define a unit cell of minimum volume. The lattice parameters (a, b, c, α, β, γ) are then obtained via

$$\begin{bmatrix} a_x & a_y & a_z \\ b_x & b_y & b_z \\ c_x & c_y & c_z \end{bmatrix} = \begin{bmatrix} a_x^* & b_x^* & c_x^* \\ a_y^* & b_y^* & c_y^* \\ a_z^* & b_z^* & c_z^* \end{bmatrix}^{-1}. \tag{2-5}$$

Delauney reduction provides an approach toward standardizing the choice of unit cell basis triplet (International Union of Crystallography, 1952). There remains always some ambiguity when measurement errors are large.

2.4.3. Indexing Reciprocal Lattice Vectors The Miller indices of a reciprocal lattice vector can be assigned with respect to the conventional reciprocal lattice basis triplet provided the crystal lattice is known, or otherwise with respect to the experimentally inferred reciprocal lattice basis triplet, a*, b* and c*, via

$$g = \begin{pmatrix} g_x \\ g_y \\ g_z \end{pmatrix} = \begin{bmatrix} a_x^* & b_x^* & c_x^* \\ a_y^* & b_y^* & c_y^* \\ a_z^* & b_z^* & c_z^* \end{bmatrix} \begin{pmatrix} h \\ k \\ l \end{pmatrix}. \qquad (2\text{-}6)$$

2.5. RESULTS

2.5.1. Diffraction Assisted Analysis of Bulk Silicon Calibration of this technique has been done using a Si <100> crystal. Diffraction patterns of the Si specimen along the [1, -1, -6] and [1, -1, 6] zone axes were obtained via double tilts. The lattice parameters determined through (2-5) are {a=3.83 Å, b=3.87 Å, c=3.86 Å,α=60.0^o, β=119.6^o, γ=119.1^o}. This set of chosen basis defines the rhombohedral primitive cell of the Si f.c.c lattice. Compared with the literature values of Si lattice parameters, {a=3.84 Å, b=3.84 Å, c=3.84 Å,α=60^o, β=120^o, γ=120^o}, the angular disagreements are less than 1^o and spatial disagreements are less than 1%. The accuracy is competitive with that obtained by other techniques in different crystallographic applications (Liu Q.,1990; Liu Q., 1992; Liu Q., 1989; Tambuyser, 1985; Fraundorf, 1981a). The inferred and literature values of the lattice parameters of Si are listed in Table 2-3.

Table 2-3. The inferred and the literature values of the lattice parameters of Si.

Lattice Parameters	a (Å)	b (Å)	c (Å)	α (^{o})	β (^{o})	γ (^{o})
Inferred Values	3.83	3.87	3.86	60.0	119.6	119.1
Literature Values	3.84	3.84	3.84	60.0	120.0	120.0

2.5.2. **Analysis of A Nanocrystal Using Images Only** In this section we use two approaches to perform 3D crystallographic anlysis of a nanocrystal. These two approaches are: 1) identification of the crystal lattice by comparing the acquired lattice fringe vectors with candidate lattices, to look for consistent lattice spacings and interplanar angles, and 2) direct determination of the lattice parameters of the nanocrystal. After that, we increase the tolerances for spacing and interplanar angle disagreements used in the first approach, to allow for greater uncertainties that may exist, hence eliminating alternate interpretations even more forcefully where possible.

2.5.2.1 Identification and Determination of A Nanocrystal Lattice Figure 2-9 and Figure 2-10 show a tungsten carbide nano-crystal (labeled A) at specimen orientations of ($\theta_1 = 15°$, $\theta_2 = 9.7°$) and ($\theta_1 = -15°$, $\theta_2 = -9.7°$), respectively. Three lattice fringe vectors of A are visible. The combination of lattice spacings and inter-planar angles of the three lattice fringe vectors were used to look for consistent lattice structures of 36 tungsten carbide and oxide candidates including WC_{1-x}. When an angular tolerance of 2^o and a spatial tolerance of 2% are imposed, this nano-crystal is uniquely identified as WC_{1-x}. The three lattice fringe vectors are indexed as $g_1 = (200)$, $g_2 = (020)$ and $g_3 = (1, 1, -1)$, respectively. The nanocrystal A in Figure 2-9 and Figure 2-10 are along its [001] and [112] zones, respectively.

The azimuth of the reciprocal lattice vector (2, -2, 0) was measured from the power spectrum of Figure 2-9. This azimuth is

$$\varphi_{(2,-2,0)} = \{\varphi_{(2,0,0)} + [180° + \varphi_{(0,2,0)}]\}/2 = \{79.2° + [180° - 11.6°]\}/2 = 123.8,$$

which deviates from the projection of the effective tilt axis by only 0.3^o. Therefore the (2, -2, 0) lattice planes are perpendicular to the effective tilt axis. The data acquired are consistent with our expectation shown in Figure 2-1. These two zone images and the actual tilting path in the Kikuchi map of crystal a are shown in Figure 2-11.

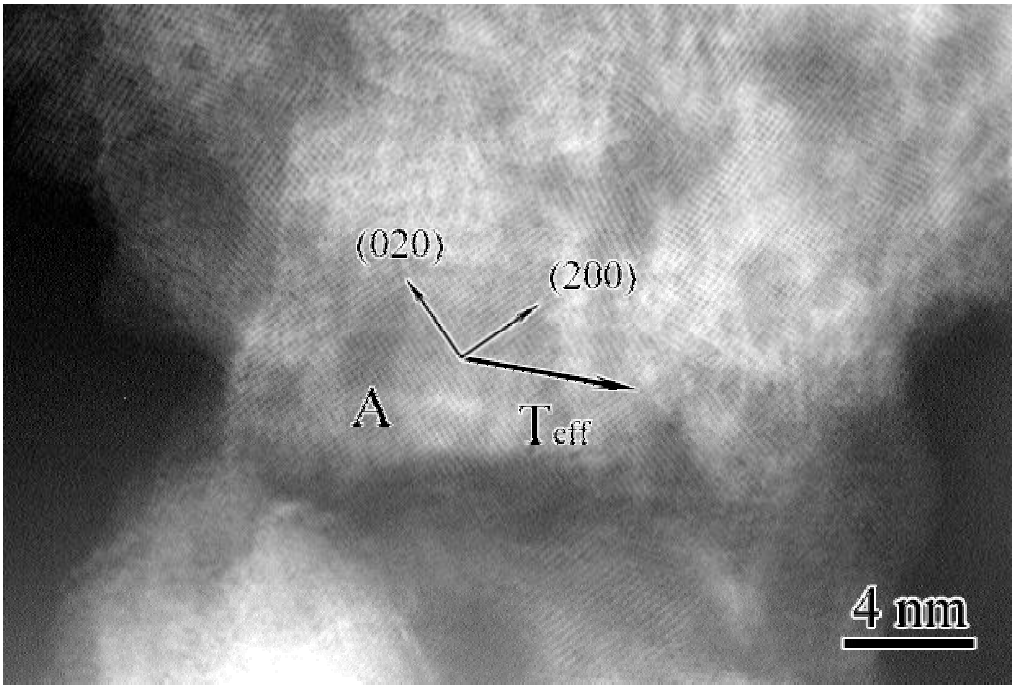

Figure 2-9. An HRTEM image showing a nanocrystal A taken at the specimen orientation of (θ_1=15^o, θ_2=9.7^o).

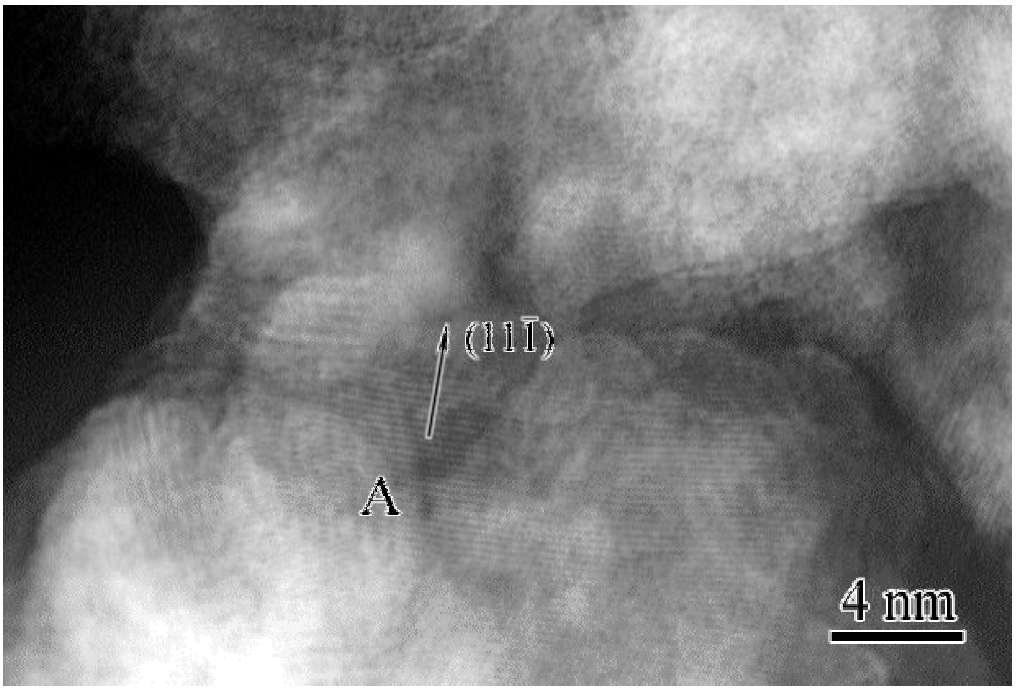

Figure 2-10. An HRTEM image showing the nanocrystal A taken at the specimen orientation of (θ_1 = -15^o, θ_2 = -9.7^o).

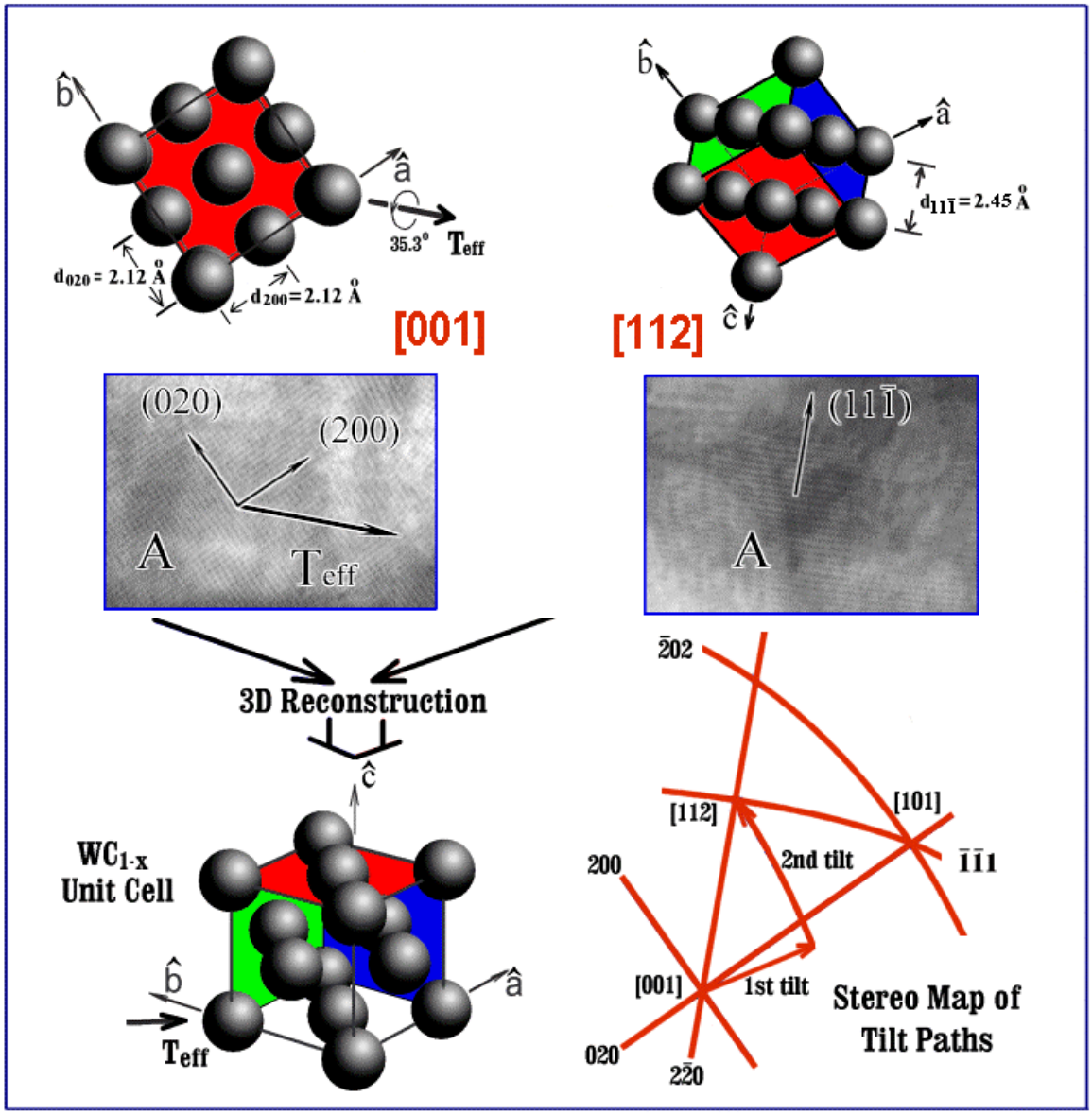

Figure 2-11. Schematic illustrating the application of the f.c.c. protocol to resolve the lattice structure of WC_{1-x}, together with the corresponding lattice image taken at two tilts. The stereo map of the tilt path is also shown.

The lattice parameters determined using equation (2-5) are {a=2.98 Å, b=2.99 Å, c=2.96 Å, α=120.0°, β=58.7°, γ=119.8°}, which compare favorably with those of WC_{1-x} {a=3.00 Å, b=3.00 Å, c=3.00 Å,α=120.0°, β=60.0°, γ=120.0°}, with spatial disagreements less than 1.5%, and angular disagreements less than 1.6°. The linear relationship between the reciprocal lattice vectors and the inferred basis triplet indicates the following indexing: $\mathbf{g}_1$ = (101), $\mathbf{g}_2$ = (0, 1, -1), $\mathbf{g}_3$ = (100). The first zone axis is [-1, 1, 1]. The "effective tilt" is along the $\mathbf{g}_1$ - $\mathbf{g}_2$ = (1, -1, 2) lattice planes. The second zone axis is [0, 2, 1]. Detailed calculations leading to the above conclusions are listed in Table 2-4 through Table 2-7.

Table 2-4. The lattice spacings, d, and azimuths, φ, of $\mathbf{g}_i$ (i = 1, 2, 3) measured from the power spectra of the nanocrystal A shown in Figure 2-9 and Figure 2-10. The camera constant λL = 66.2 pixel•Å.

$\mathbf{g}_i$	r(pixel)	$1/d = r/\lambda L$ (Å^{-1})	$d = \lambda L / r$ (Å)	φ(°)
$\mathbf{g}_1$ = (200)	31.3	0.473	2.12	79.2
$\mathbf{g}_2$ = (020)	31.6	0.477	2.09	-11.6
$\mathbf{g}_3$ = (1, 1, -1)	27.4	0.414	2.42	32.6

Table 2-5. The coordinates of $\mathbf{g}_i$ (i = 1, 2, 3) in reciprocal space, calculated using (2-2) and (2-3), and based on which the inter-planar angles can be determined via $\theta_{jk} = \cos^{-1}[\mathbf{g}_j \bullet \mathbf{g}_k/(g_j g_k)]$, (j, k =1, 2, 3; j, k ≠ i).

$\mathbf{g}_i$	g_{mx}(pixel)	g_{my}(pixel)	g_x(pixel)	g_y(pixel)	g_z(pixel)	θ_{jk}(°) (j, k ≠ i)
$\mathbf{g}_1$	5.9	30.7	5.7	30.0	-6.7	54.1
$\mathbf{g}_2$	31.0	-6.3	29.9	-7.6	-6.8	56.2
$\mathbf{g}_3$	23.1	14.8	22.3	13.5	8.4	90.7

Table 2-6. Match of $\mathbf{g}_i$ (i = 1, 2, 3) with the reciprocal lattice of WC_{1-x} using (2-6) and based on the consistency of lattice spacings and inter-planar angles as shown in Table 2-4 and Table 2-5, with a spatial and an angular tolerances of 1.5% and 1.5° imposed, respectively. The other 35 tungsten carbides and tungsten oxides have been excluded. $\Delta\theta_{jk}$ is the difference between an interplanar angle determined from experimental data and its literature value counterparts.

$\mathbf{g}_i$	d_{hkl}(Å)	$\lvert d-d_{hkl}\rvert / d_{hkl}$ (%)	$\Delta\theta_{jk}$(°) (j, k ≠ i)
$\mathbf{g}_1$ = (200)	2.12	0.0	-0.6
$\mathbf{g}_2$ = (020)	2.12	1.4	1.5
$\mathbf{g}_3$ = (1, 1, -1)	2.45	1.2	0.7

Table 2-7. An inferred reciprocal lattice triplet, (**a***, **b***, **c***), based on which the lattice parameters, (a, b, c, α, β, γ), can subsequently be calculated using (2-5) as shown in 2.5.2.1.

	$\mathbf{a}^*=\mathbf{g}_3$	$\mathbf{b}^*= \mathbf{g}_1+\mathbf{g}_2-\mathbf{g}_3$	$\mathbf{c}^*= \mathbf{g}_1-\mathbf{g}_3$
x component (pixel, $Å^{-1}$)	22.3, 0.336	13.3, 0.201	-16.6, -0.251
y component (pixel, $Å^{-1}$)	13.5, 0.204	8.9, 0.135	16.5, 0.250
z component (pixel, $Å^{-1}$)	8.4, 0.126	-21.9, -0.331	-15.1, -0.228

2.5.2.2 Strengthening the Case for WC_{1-x} As will be discussed in Chapter 4, various factors contribute to lattice spacing and interplanar angle uncertainties. For example, in HRTEM images of a 100 Å WC_{1-x} crystal, the uncertainties of the {002} spacing and the interplanar angle as indicated from the <001> zone cross-fringes are predicted to be about 1.8% and 1.9°, respectively. However, larger disagreements can be projected in reality. In our identification of the lattice structure of nanocrystal A, analyses considering larger possible errors will enable drawing a more robust conclusion.

When the tolerances in matches of lattice spacing and interplanar angle are increased up to 3° and 3%, there are many tungsten oxide and carbide candidates in addition to WC_{1-x} capable of providing indices to the observed lattice fringe vectors $\mathbf{g}_i$ (i = 1, 2, 3) (Qin,1998). In order to properly perform subsequent phase identification, it is necessary to realize that the spatial frequencies in Figure 2-9 and Figure 2-10 are continuously transferred within the first passband up to 1/(1.9 Å) (Spence, 1988b; Williams, 1996l), as shown by a power spectrum of an amorphous region in each image. Armed with this fact and by taking into account the full reciprocal lattice array along

possible zones, all the candidates except WC_{1-x} have been excluded. Specifically, it is found that for each of the candidates except WC_{1-x}, along at least one of the indexed zone axes, at least one reciprocal lattice vector shorter than the indexed experimental one(s) is missing. Table 2-8 shows an example of excluding a match with hexagonal WC_x (a = 10.58 Å, c = 13.35 Å). In this example the suggested Miller indices of $\mathbf{g}_3$ would require that another reciprocal lattice vector, (-2, 1, -1), is missing from the power spectrum of the image of nanocrystal A as shown in Figure 2-10. This match with WC_x is hence excluded.

Table 2-8. An example in excluding candidate reciprocal lattice in phase identification. The candidate is WC_x in this case. The suggested Miller indices of $\mathbf{g}_3$ indicate that another reciprocal lattice vector, (-2, 1, -1), is missing from the power spectrum of the image of nanocrystal A shown in Figure 2-10. This match with WC_x is hence excluded.

$\mathbf{g}_i$	(h, k, l)	d_{hkl}(Å)	$\lvert d-d_{hkl}\rvert / d_{hkl}$ (%)	Missing Vector	$\theta_{jk,\,wcx}$(°)	$\Delta\theta_{jk}$(°)
$\mathbf{g}_1$	(-1, 0, -6)	2.16	1.9		56.3	2.1
$\mathbf{g}_2$	(-3, 5, 0)	2.10	0.5		56.8	0.6
$\mathbf{g}_3$	(-4, 2, -2)	2.46	1.6	(-2, 1, -1)	88.4	-2.4

The exclusion of other matches of lattice spacings and interplanar angles is not as easy as the one above, and takes some extra work, but is based on the same principle. Zone axes need to be calculated at first, after which the missing reciprocal vector(s) can be found. An example is given in Table 2-9. The candidate is also WC_x in this case. The suggested first zone axis indicates that another reciprocal lattice vector, (-4, 1, -2) is missing from the power spectrum of the image of nanocrystal A shown in Figure 2-9.

Table 2-9. An example in excluding candidate reciprocal lattice in phase identification. The candidate is WC_x in this case. The suggested first zone axis indicates that another reciprocal lattice vector, (-4, 1, -2), is missing from the power spectrum of the image of nanocrystal A shown in Figure 2-9. This match with WC_x is hence excluded.

$\mathbf{g}_i$	(h, k, l)	d_{hkl}(Å)	$\lvert d-d_{hkl}\rvert/d_{hkl}$ (%)	g_{hkl}(Å^{-1})	Zone	Missing Vector g (Å^{-1})	$\theta_{jk,\,wcx}$ (^{o})	$\Delta\theta_{jk}$ (^{o})
$\mathbf{g}_1$	(-5, 2, -1)	2.08	1.9	0.481	[-1, -2, 1]	$g_{-4,\,1,\,-2} = 0.422$ ($<g_{-5,\,2,\,-1}$, $g_{1,\,-3,\,-5}$)	51.9	-2.3
$\mathbf{g}_2$	(1, -3, -5)	2.11	0.9	0.474			54.5	-1.7
$\mathbf{g}_3$	(-2, 1, -5)	2.38	1.7	0.420			90.4	-0.4

2.6. DISCUSSION

2.6.1. **A Special Direction: The Effective Tilt Axis Direction** In addition to serving as a guide to correctly set the azimuth of the crystal in tilting between the desired zones in each protocol, knowledge of the tilt axis direction plays another important role in predicting lattice fringe visibility after tilt (Qin, 2000c). As a crystal gets smaller, lattice fringes stay visible for larger deviations from the Bragg condition. Hence the persistence of fringes under tilt affects the abundance and range of lattice fringes that one sees in an image of randomly-oriented crystals. Rules for recognizing redundant lattice fringes are important in the search for new lattice fringe sets by tilting the specimen.

In a single tilt the tilt axis is simply T_1, which is always perpendicular to the electron beam and hence parallel to the micrographs. Any reciprocal lattice vector parallel or antiparallel to T_1 remains in Bragg condition throughout the whole tilting process, regardless of the amount of tilt θ_1. If the corresponding spatial frequency is transferred, the same lattice fringes will be seen perpendicular to the projection of T_1 in a HRTEM image taken in any specimen orientation (Qin,1998; Qin, 2000c).

In a double tilt, it is convenient to introduce a concept of effective tilt axis. An effective tilt axis is analogous to the tilt axis in a single tilt, in that the double tilt can be characterized by a single tilt around the effective tilt axis. The effective tilt axis is perpendicular to the electron beam and hence parallel to the micrographs only if the two specimen orientations are symmetric about the untilted one, i.e., ($\theta_1 = 0^o$, $\theta_2 = 0^o$). Here

we only consider double tilts falling into this category. Let (θ_1, θ_2) and $(-\theta_1, -\theta_2)$ denote the two specimen orientations in a double tilt. Such effective tilt axis directions have azimuths of

$$\varphi_{eff} = \tan^{-1}[-\cos(\theta_2)\sin(\theta_1)/\sin(\theta_2)]. \quad (2\text{-}7)$$

A derivation of (2-7) is given in the Appendix A. There will still exist a 180^o ambiguity in the direction of the effective tilt axis after using (2-7). Such ambiguity can be resolved with knowledge of the actual tilting sequence. In our experiment where θ_1=15° and θ_2=9.7°, φ_{eff} = 123.5°. This is the effective tilt axis direction mentioned in 2.2 and 2.5.2.1, where the tilt protocol and the correlation of the performance of the experiment with the protocol are discussed, respectively.

Any set of lattice planes perpendicular to the effective tilt axis remains in Bragg condition (only) in the initial and final specimen orientations, but not in any intermediate one. Many lattice fringes of such lattice plane sets have been observed in the same double tilt, as mentioned in 2.5.2. Figure 2-12 shows the images of a nano-crystal H with such a (1, 1, -1) lattice fringe set, which appears in both specimen orientations with identical azimuth and spacing. One may tentatively assume that the corresponding lattice fringe vectors in the two specimen orientations are distinct ones, and denote them as $\mathbf{g}_3$ and $\mathbf{g}_4$. They deviate from the effective tilt axis by only 0.4^o and 0.5^o, respectively. 3D reconstruction shows that $\mathbf{g}_3$ and $\mathbf{g}_4$ differ in magnitudes (0.407 $Å^{-1}$ and 0.403 $Å^{-1}$, respectively) by 1.0%, and subtend an angle of 0.2°, as shown in Table 2-10. This suggests that they arise from a single set of lattice planes. With the availability of the reciprocal lattice spot sizes, which will be determined experimentally in Chapter 4, it can be quantitatively proved that $\mathbf{g}_3$ and $\mathbf{g}_4$ are the results of the intersection of the same (1, 1, -1) reciprocal lattice spot with the Ewald sphere in both specimen orientations (Qin, 2000c).

Table 2-10. Analysis of the repeated appearance of the (1, 1, -1) lattice fringe vector of crystal H in a double tilt from the specimen orientation of (θ_1 = 15.0°, θ_2 = 9.7°), denoted as SO_1, to that of (θ_1 = -15.0°, θ_2 = -9.7°), denoted as SO_2, as shown in Figure 2-12. The lattice fringe vector is perpendicular to the effective tilt axis, and therefore is visible, and has identical magnitude and direction, before and after tilt (the camera constant λL = 71.9 pixel•Å).

Orientation	r(pixel)	$g = r/(\lambda L)$ (Å^{-1})	$d = \lambda L/r$ (Å)	φ(°)	$\lvert\varphi-\varphi_{eff}\rvert$(°)
SO_1	29.0	0.403	2.48	124.0	0.5
SO_2	29.3	0.407	2.46	123.9	0.4

Orientation	x_m(pixel)	y_m(pixel)	x(pixel)	y(pixel)	z(pixel)	θ_{12}(°)
SO_1	-16.2	24.0	-15.7	24.4	0.1	0.2
SO_2	-16.4	24.3	-15.8	24.7	0.0	

2.6.2. **<u>Higher Probability of Success Through Increased Tiltability</u>** In a microscope capable of a side-entry goniometer tilt of at least ±35.3°, any f.c.c crystal, with a lattice constant of $a > 2r_{Sch}$, and the [001] zone parallel to the optical axis at the specimen orientation of (θ_1 = 0°, θ_2 = 0°), can have its (2, -2, 0) reciprocal lattice vector aligned parallel or antiparallel to T_1 through an azimuthal rotation of the specimen. The parallelism of the optical axis, the [001] zone and the specimen rotation axis leaves the [001] zone parallel to the optical axis throughout the rotation. A subsequent tilting by 35.3° will lead to the [1, 1, 2] zone, along which the 2nd zone image can subsequently be taken. The following conclusion will be shown in Chapter 4. For randomly oriented f.c.c. crystals with a lattice constant of about 4 Å and each of which has a diameter of 20

how <001> zone cross-fringes approaches 1 in 100. This fraction of crystals are suitable for such stereo analysis.

Due to the tilt limits of the specimen holder in our microscope, the first [001] zone image of the WC_{1-x} nano-crystal A had to be taken at a nonzero θ_1 orientation. Therefore the specimen rotation axis is no longer parallel to the optical axis/the [001] zone. Any specimen rotation will swerve the [001] zone away from the optical axis. One

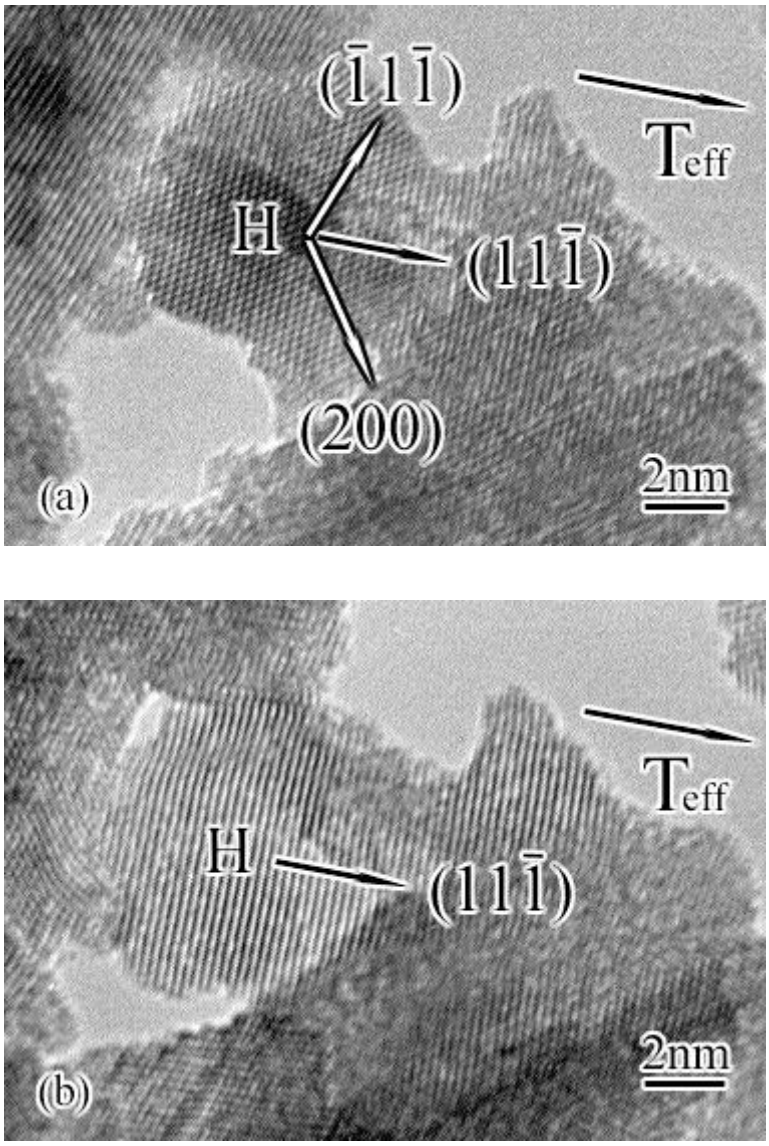

Figure 2-12. HRTEM images of a set of (1, 1, -1) lattice fringes perpendicular to the effective tilt axis and thus remaining visible after the double tilt from (θ_1 = 15.0°, θ_2 = 9.7°), as shown in (a), to (θ_1 = -15.0°, θ_2 = -9.7°), as shown in (b). The (1, 1, -1) reciprocal lattice vector remained to be in Bragg condition after tilt.

solution is to find a [001] nano-crystal whose (2, -2, 0) reciprocal lattice vector happens to be parallel to the effective tilt axis, subsequent tilting of the crystal to the 2nd orientation will lead to the [112] zone axis. In the experiment here, nanocrystal A was identified to have the appropriate azimuth upon the first encounter.

The fractions of nano-crystals from which the targeted three reciprocal lattice vectors can be acquired are different in these two approaches, with that in the first one being about three times as high. This result, as well as the genaral quantification of probabilities for success in data acquisition, will be presented in Chapter 4.

2.6.3. **Current and Potential Impacts of This Technique** In this section we will discuss different aspects concerning the influence of this stereo analysis technique. These include its influence on the characterization of the tungsten carbide specimen, a revision that can be made to improve the sampling rate, the potential contribution of it to another characterization method, the range of crystalline materials within which it is applicable, and improvement of performance with computer support. We will begin with a discussion of the results obtained from the stereo analysis of nanocrystal A, in the context of characterization of the tungsten carbide specimen.

Some chemical composition analysis of the sample has been performed prior to our study here. Electron and X-ray diffractions indicated that the non-stoichiometric f.c.c. WC_{1-x} with a = 4.248 Å is the dominant diffracting phase in the film (Qin,1998; James, 1998). Auger electron spectral analysis suggested a value of x between 0.4 and 0.8 (James, 1998). Even more recently a statistical survey of the zone images of nanocrystals in the sample that are free of overlap with others revealed the "finger-print" of WC_{1-x} crystal lattice, as will be discussed in Chapter 4.

The determination and identification of the WC_{1-x} lattice structure of nanocrystal A as described in this chapter supports all these previous analyses, yet in a manner that is specific to one certain nanocrystal. This result demonstrates 3D crystallographic analysis of individual nanocrystals. However, the high resolution of the technique also brings to focus the poor sampling rate in our experiment. To make an improvement in the sampling capability, a revised version of the technique based on 3D lattice-correlation darkfield analysis has been proposed by Fraundorf. This is applicable to polycrystalline specimens and can be illustrated with an example as follows.

Using the f.c.c. protocol given in Table 2-1, three arcs, denoted as a, b, and c as shown in Figure 2-13, along the {002} and {111} diffraction rings can be chosen by the

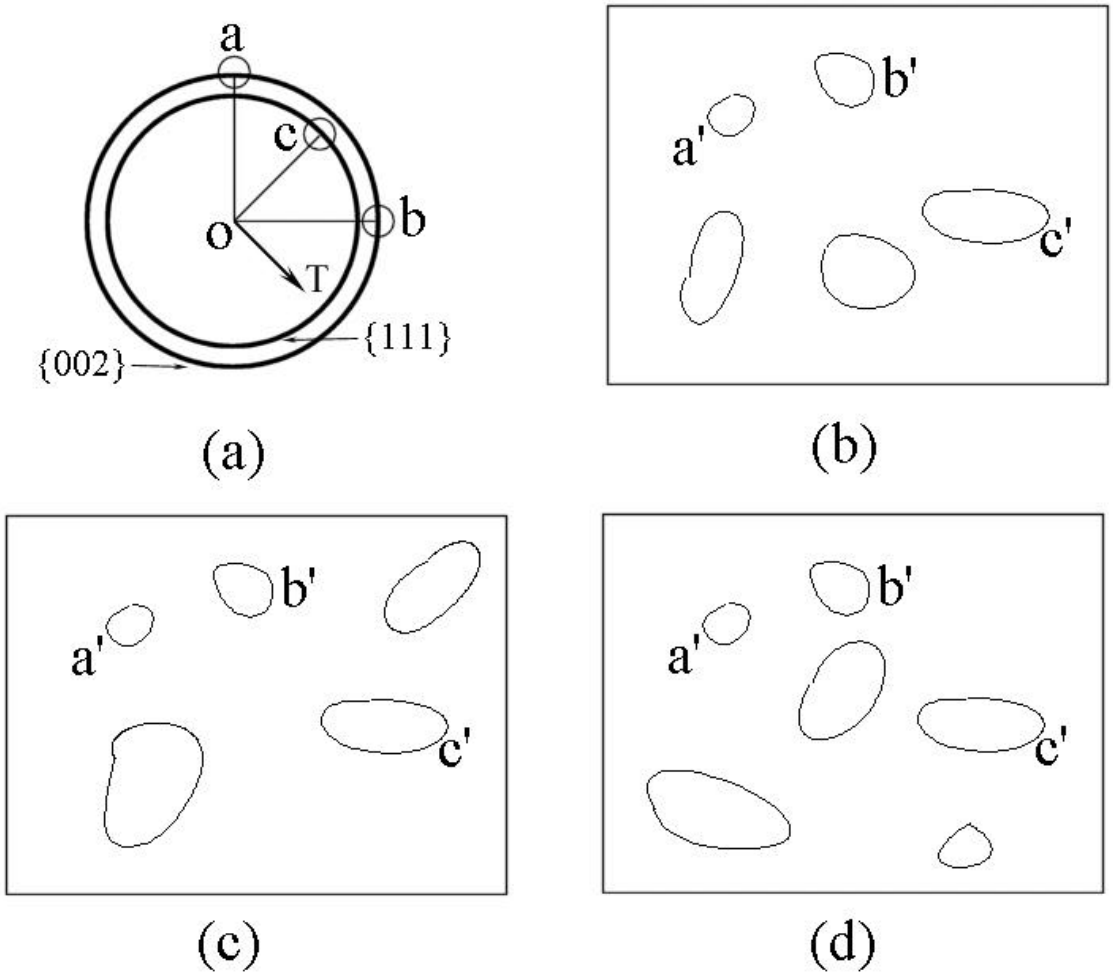

Figure 2-13. Schematic illustrating 3D lattice-correlation darkfield analysis of an f.c.c. polycrystalline specimen using the protocol given in Table 2-1. The (a) inset is an electron diffraction pattern showing only the {111} and {002} rings. The arcs chosen by the small circles centered at a, b and c denote the diffraction intensities selected by the objective aperture. The arcs a and b are chosen at one specimen orientation, and oa⊥ob. The specimen is then tilted 35.3° away, and the tilt axis T is 45° below ob. The arc c is then so chosen that oc⊥T. It can be seen that the three arcs satisfy the same spatial relationship of the three reciprocal lattice vectors in the protocol. The (b), (c) and (d) insets are the corresponding darkfield images. All the crystals lit up in the three darkfield images, a', b', and c' in the figure, are of the same f.c.c. lattice.

objective aperture to form darkfield images. The arcs a and b are chosen in one specimen orientation, and c is chosen in another which is 35.3° away. These three arcs are so chosen as to satisfy the same spatial relationship as those three targeted reciprocal lattice vectors in the protocol. It can be concluded that all the crystals that light up in all three darkfield images are of f.c.c. crystal lattice.

Although this analysis may never allow precise lattice parameter determination given limits on the objective aperture size, it may be an efficient way to look for multiple crystals correctly-oriented and of correct type for one of the protocols. Moreover, because such lattice-correlations in 3D contains information beyond the pair-correlation function, they may be able to support the new techqniue of fluctuation microscopy in studying paracrystalline specimens with order-range too small for detection by other means (Treacy, 1993; Treacy 1996; Gibson, 1997; Gibson, 1998).

Another subject of interest is the range of materials to which the technique applies. It becomes obvious from Figure 2-2 that with a tilt range of at least 35.3°, and a point resolution of 1.9 Å, determination of the 3D crystal lattice can be done in a TEM for any cubic crystal whose cell side is greater than 2×1.9 Å = 3.8 Å. This covers a wide range of materials, which include more than 85% of the cubic close packed crystals and nearly 40% of the elemental b.c.c crystals tabulated in Wyckoff, and of course most cubic crystals with asymmetric units comprised of more than one atom (Wyckoff, 1982).

Computer-supported and automated tilt/rotation will make this technique more accurate and widely accessible.

2.7. CONCLUSION

Here a technique has been presented to determine the 3D lattice of a single crystalline particle from HRTEM images taken along two low index zones. This technique expands crystal lattice structure information obtained from individual HRTEM images to 3-dimension through 3D reconstruction, and posesses atomic-resolution. Such a high-resolution enables studying nanocrystals individually.

Due to the finite resolution of a typical HRTEM, the possibilities to resolve a compact crystal lattice are limited and hence can be enumerated. Corresponding to each of such possibilities, there exists a data acquisition protocol. Each protocol invloves tilting between two low-index zones, along which three sets of linearly-independent lattice planes can be resolved. The three corresponding reciprocal lattice vectors must lie in the first passband of the contrast transfer function. This is required so as not to miss reciprocal lattice vectors shorter than the longest among the three, and possibly

suppressed by a zero in the contrast transfer function. Utilization of frequencies in higher passbands through defocus adjustment makes this technique still applicable to crystal lattices where spatial frequencies of interest are beyond the first passband. The "one angstrom microscope" at the national center in Berkely is a candidate for this extension. In order to tilt to the 2nd zone axis, the protocol also specifies the azimuth of the crystal relative to the tilt axis when the 1st zone image is formed. The tilt protocols vary with lattice type, therefore information about crystal phase must be obtained in advance, usually from chemical composition analysis and other microscopy techniques. For f.c.c. and b.c.c. lattices with lattice constants $a>2r_{Sch}$, and s.c. lattice with a $>\sqrt{3}r_{Sch}$, it has been found that 35.3°, 30° and 19.5° of tilts, respectively, are sufficient to infer the 3D lattices. For graphite as an example of hexagonal lattice, the lowest amount of tilt involved is about 14.6° with a TEM of r_{Sch} =1.9 Å. In the example presented the lattice parameters of a 10 nm WC_{1-x} nano-crystal have been determined, with less than 1.4% spatial and 1.4° disagreements from literature values.

Before this technique can be applied, the projections of the tilt axes on HRTEM images must be determined. Any reciprocal lattice vectors parallel or antiparallel to the effective tilt axis direction, and perpendicular to the electron beam in a double tilt remains at Bragg condition only at the initial and final specimen orientations. Care must be taken not to interpret such redundant frequencies as new lattice structure features.

Three-dimensional lattice-correlation darkfield analysis using the same protocols can be applied to identify multiple crystals of the same lattice structure in polycrystalline specimens. This will greatly improve the sampling rate.

We have found that this technique is accessible to a very wide range of crystalline materials. For example, with a TEM of r_{Sch} = 1.9 Å, and a tilt range of at least 35.3°, more than 85% of the cubic close packed crystals and nearly 40% of the elemental b.c.c crystals tabulated in Wyckoff, and most cubic crystals with asymmetric units comprised of more than one atom can be subjected to the stereo analysis. An instrumentation improvement to include ±35.3° of tilt, and the use of a tilt/rotate specimen holder, will increase the fraction of crystals suitable for the stereo analysis to about three times as high. Computer-supported specimen orientation adjustment can further enhance the chance to be successful.

3. LATTICE FRINGE VISIBILITY AFTER TILT

3.1. INTRODUCTION

High-resolution transmission electron microscopy (HRTEM) is a powerful tool for structure studies (Spence, 1988c). Information easily interpretable in lattice images includes lattice plane spacing, local crystal orientation and structures such as interface, grain boundary, and dislocation (Williams, 1996j). However, in many other cases, the complexity of the image formation process warrants caution be taken in order for reliable conclusions, e.g., with regard to fringe intensities and positions (Hirsch, 1977e). Generally the positions of lattice fringes bear no simple relation to the atomic planes. In extremely thin (kinematical) specimens under “two-beam condition” (only one diffracted beam is strongly excited, in addition to the direct beam), the lattice fringe visibility is easily shown to depend on crystal orientation and thickness (Hirsch, 1977b). Thickness variation can also cause fringe shift, bend and even spacing change (Menter, 1958; Chadderton, 1961). Among recent image simulation studies of small metal particles, it has been demonstrated that for a 2.8 nm Pd particle rotated over 90° and tilted up to 45° from the [011] zone axis, deceptive lattice fringes that are "Moires" instead of direct representations of the lattice planes may be formed, as a result of low-pass filtering by the microscope of dense projected atom positions (Malm, 1997). In addition to the complicated effects arising from crystal orientation, size, and instrument response, the lack of depth sensitivity imposes another serious obstacle to interpretation of lattice images. In typical cases atoms can be displaced by distances of 20 Å or more in a direction parallel to the electron beam without changing the images (Hirsch, 1977f). Recently a technique has been developed to remove lattice parameter ambiguities associated with the problem of projection (Qin, 1999). This is realized by determining the lattices of individual crystals in 3D from HRTEM images taken at two tilts. During operation of this technique, tilting is applied to look for 3 linearly independent reciprocal lattice vectors. When the crystals are a few nanometers in size, the reciprocal lattice spots expand significantly in reciprocal space. As a result, lattice fringes stay visible for large deviations from the Bragg condition, and hence are more abundant in images. The

convergence of incident electrons further enhances this effect. For example, a subset of the fringes in an image remained "still-visible" after large (e.g., 35°) single or double axis tilts (Qin, 1998). When one looks for new lattice fringes from the same crystal through orientation adjustment, rules for recognizing redundant fringes are helpful as well. In this chapter we present a semiempirical model for predicting the visibility of lattice fringes after tilt.

3.2. EXPERIMENTAL SETUP

The same tungsten carbide nanocrystalline thin film sample as described in Chapter 2 was used in the TEM study. HRTEM imaging was performed in a Philips EM430 ST TEM with both a Philips single tilt holder and a Gatan double tilt holder.

A coordinate system (different from that used in Chapter 2) whose xy plane coincides with the micrograph plane was set up. As will become clear, what matters in predicting lattice fringe visibility is the absolute value of the azimuthal angle between a lattice fringe vector and the tilt axis. Consequently the coordinate system can be simply defined as follows. With the micrograph placed in the microscope, the x axis points from the left to the right of the microscope operator, and the z axis is along the electron beam direction. Counterclockwise is defined as the positive azimuth direction in the xy plane. The HRTEM images are of a magnification of 700K. In this coordinate system, the azimuths of the projections of T_1 and T_2 on HRTEM images are -156.9° and 113.1°, respectively, as shown in Figure 2-6.

3.3. RESULTS

3.3.1. Fringe Visibility Confirmation of Tilt Axis Projection In an earlier work to correlate the determined azimuth of the T_1 projection with HRTEM observation, lattice images of the specimen at different orientations were taken by tilting around T_1 using the single tilt holder (Qin, 1998). Two pairs of such HRTEM images are shown in Figure 3-1 and Figure 3-2.

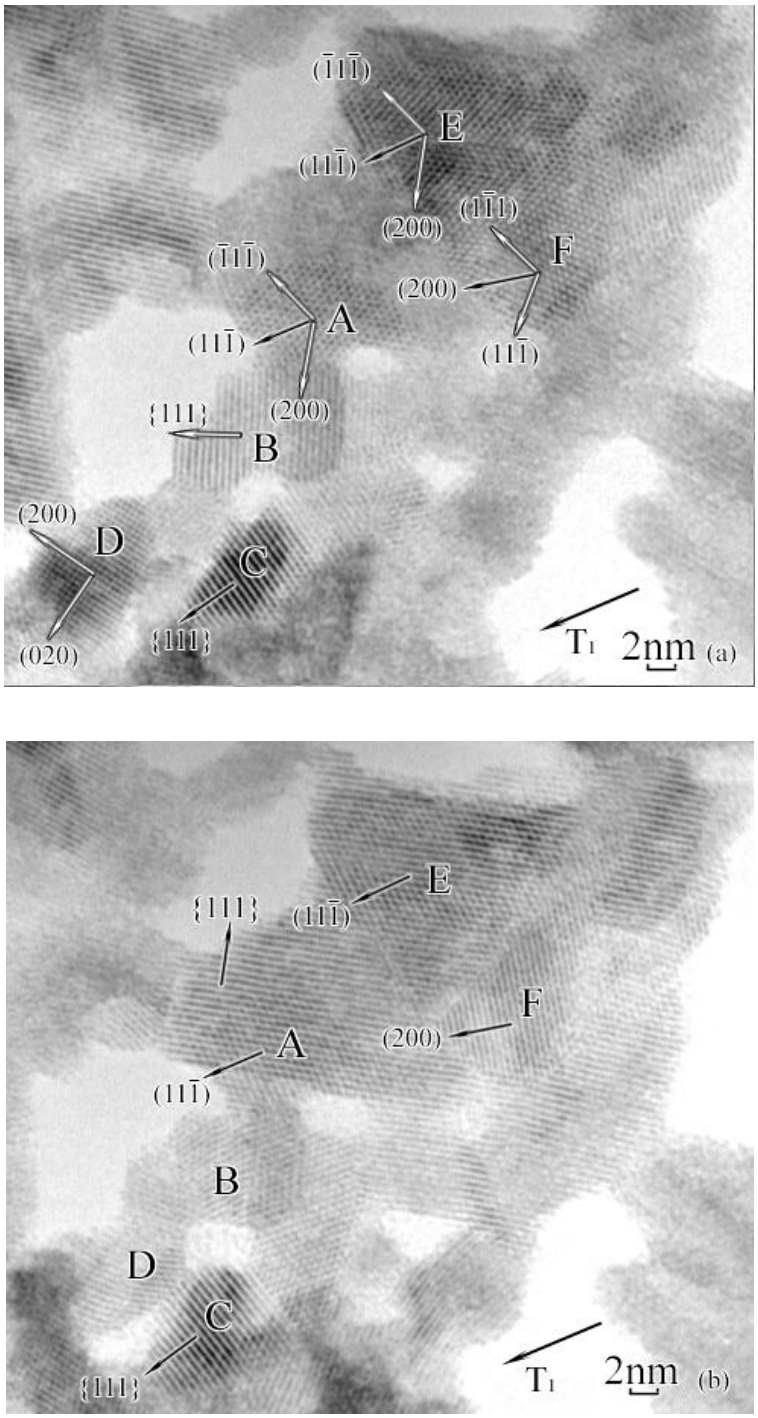

Figure 3-1. HRTEM images of six WC_{1-x} nanocrystals showing lattice fringes that become invisible and remain visible after a single tilt. The image in the (a) inset was taken at the specimen orientation of θ_1=14.5°, and that in the (b) inset at θ_1=0.0°, where θ_1 is the reading of the side-entry goniometer tilt axis. The projection direction of the side-entry goniometer tilt axis is marked. Each lattice plane set has been labeled with both Miller indices and an arrow representing the lattice fringe vector. The length of the arrow is proportional to that of the lattice fringe vector. In the (a) inset, hollow arrows are used for lattice fringes that are predicted to become necessarily invisible, and solid arrows for those with certain propabilities to do so, in the second specimen orientation as shown in the (b) inset.

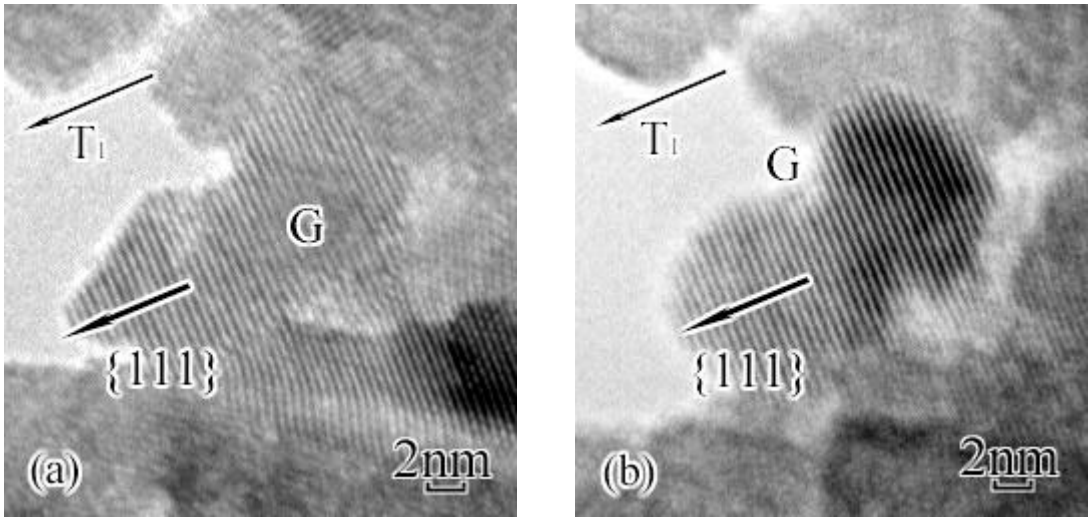

Figure 3-2. HRTEM images of a WC_{1-x} nanocrystal G showing one set of {111} lattice fringes which remains visible after a single tilt of 30.2°. The image in the (a) inset was taken at the specimen orientation of θ_1= -14.9°, and that in the (b) inset, θ_1=15.7°. The projection of the side-entry goniometer tilt axis is marked in both insets. The {111} fringe set is perpendicular to the side-entry goniometer tilt axis and therefore remains visible, and unchanged in its spacing and azimuth throughout the tilt.

In each figure, the a and b insets are images of the same field of view at different specimen orientations. The tilts are 14.5° apart in Figure 3-1, and 30.6° in Figure 3-2. The crystals are labeled A~G. In a single tilt, under eucentric condition, T_1 is parallel to the image plane. It is therefore expected that any lattice fringe set perpendicular to T_1 will remain visible, and unchanged in its spacing and azimuth throughout the tilt. Such lattice fringe sets have been found. They are the (1,1,-1) fringes of crystal A in Figure 3-1, and the {111} fringes of crystal G in Figure 3-2. For example, the azimuths and magnitudes of the (1,1,-1) lattice fringe vector of crystal A in the a and b insets of Figure 3-1 are –157.2°, 1 / (2.45 Å), and –156.5°, 1/ (2.43 Å), respectively. They deviate from being parallel to the projection of T_1 by only –0.3° and 0.4°, respectively. The lattice fringe spacing has a small variation of about 0.8% only.

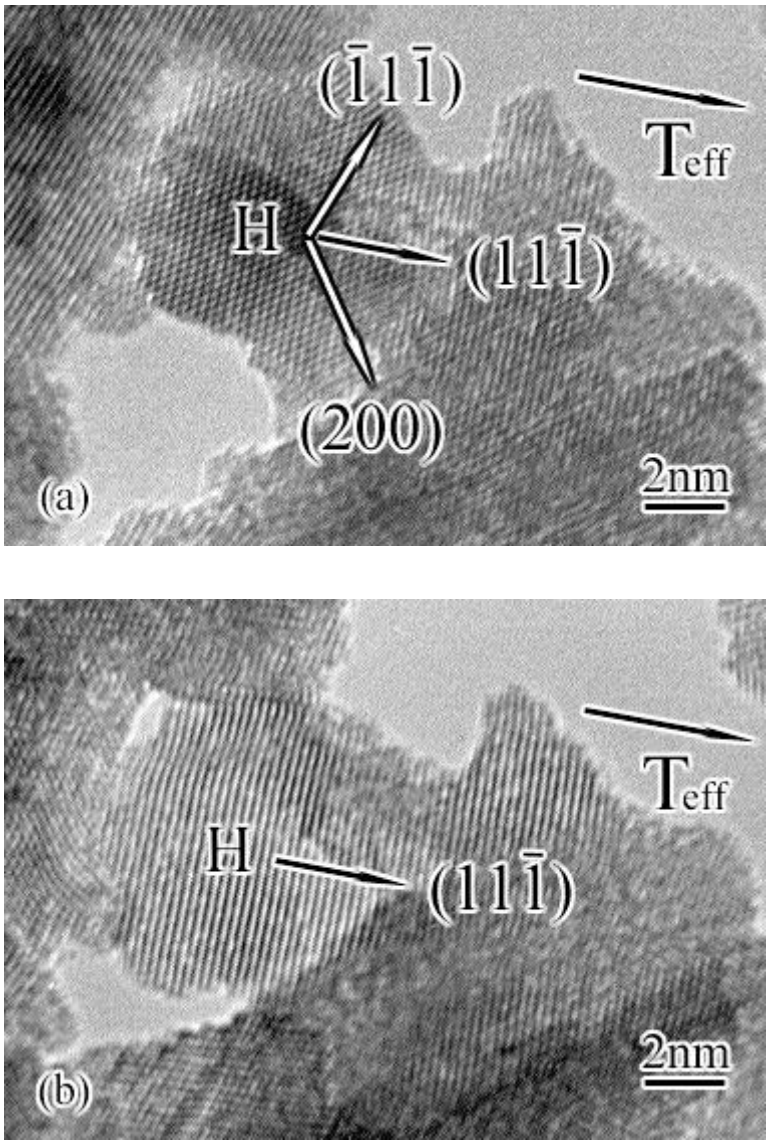

Figure 3-3. HRTEM images of a WC_{1-x} nanocrystal H showing a persistently visible (1, -1, 1) lattice fringe set before and after a double tilt of 35.3°. The lattice fringe set is perpendicular to the effective tilt axis. The image in the (a) inset was taken at the specimen orientation of (θ_1= 15.0°, θ_2= 9.7°), and that in the (b) inset at (θ_1= -15.0, θ_2= -9.7°). The (1, 1, -1) lattice fringe set also remains unchanged in both its spacing and azimuth after tilt.

The determined T_2 projection has been similarly correlated with HRTEM observation in double-tilt experiments. The images shown in the (a) and (b) insets of Figure 3-3 were taken at the specimen orientations of (θ_1 = 15.0°, θ_2 = 9.7°) and

(θ_1 = -15.0°, θ_2 = -9.7°), respectively. The effective tilt axis is along -10.4°.[♣] The normal of the (1, 1, -1) lattice fringes in crystal H is along –11.0° in both a and b insets. They deviate from the effective tilt axis by only –0.6°.

3.3.2. A Theory of Lattice Fringe Visibility After Tilt From the large relaxation of Bragg condition for small crystals, it can be expected that a set of lattice fringes does not have to be azimuthally so close to being perpendicular to the tilt axis as those mentioned above, in order for it to remain visible after tilt. Instead, a certain limit of deviation of the lattice fringe vector from the tilt axis exists. Within such a limit, the position variation of the corresponding reciprocal lattice spot caused by tilting is not large enough for the spot to lose intersection with the Ewald sphere after tilt.

In the following discussion the crystal is assumed to be spherical, and only one set of lattice planes is considered. Quantities used to specify the geometry of the nanocrystal diffraction are described as follows: The radius of a reciprocal lattice spot is $g_t = f / t$, where t is the diameter of the crystal and f is a signal to noise ratio empirically adjusted to visualize fringes (experimentally determined to be 0.7902 for AuPd particles sputtered on a thin carbon film, as will be shown in Chapter 4) (Qin, 2000b). Also in what follows, d is the lattice spacing and $g_\lambda = 1/\lambda$ is the radius of the Ewald sphere, where λ is the electron wavelength.

The lattice fringe visibility model was first developed by Qin based on an assumption of a flat Ewald sphere. Fraundorf later provided insight on the mirror symmetry in the problem, built a model which takes into account the Ewald sphere curvature, and introduced the concept of “visibility band”. The model developed by Fraundorf is presented here.

3.3.2.1 A Mirror Symmetry As the first step in predicting lattice fringe visibility after tilt, note that there is a mirror symmetry for the electron beam relative to the lattice plane set. The mirror plane can be any one that is parallel to the lattice plane set. An

---

[♣] In the coordinate system used in Chapter 2, the azimuth of the effective tilt axis is 123.5°, which is 123.5°-113.1° =10.4° below the x-axis in the coordinate system used here.

electron beam incident from one side of the mirror plane will produce fringes identical to those produced by another electron beam that is mirror-symmetric with it. A schematic illustration is given in Figure 3-4. In this figure, A'B' is the intersection of the mirror plane with the plane shown on the top and perpendicular to the lattice plane set. The electron beams incident from both sides of A'B' are mirro-symmetric with each other and will have the same diffraction effect.

Based on the symmetry, we can focus on only one side of the mirror plane in investigating the diffraction geometry, and hence only one reciprocal lattice spot (on the same side of the mirror plane) out of the two. As will be seen, we will start tilting the lattice plane set from the configuration in which the electron beam is parallel to the mirror plane, i.e., along a direction that is parallel to the line A'B' as shown in Figure 3-4 , or equally stated, the incidence is perpendicular to the reciprocal lattice vectors, to explore the relative angular range of the electron beam within which the lattice fringes are visible. In the following discussion, we will refer to this configuration as the starting configuration, unless otherwise specified.

3.3.2.2 The Geometry Figure 3-5 shows the general configuration of diffraction of a lattice plane set. Here the lattice fringes are visible and accordingly a reciprocal lattice spot intersects the Ewald sphere. The intersection of either reciprocal lattice spot, C or D as shown in the figure, with the Ewald sphere identically results in lattice fringe visibility. Therefore as the crystal is tilted, the relation between either spot and the Ewald sphere must be considered (In this figure, the tilt axis is chosen to point into the paper so that we can just focus on spot C relative to the Ewald sphere). Beginning from the starting configuration, as BC = g is tilted toward A, BD = -g is tilted away from A. Since the Ewald sphere curves up, spot C is always going to lose intersection with the Ewald sphere later than spot D does. Therefore the upper limit of tilt is determined by the position of spot C relative to the Ewald sphere only (when we focus on the left side of AB).

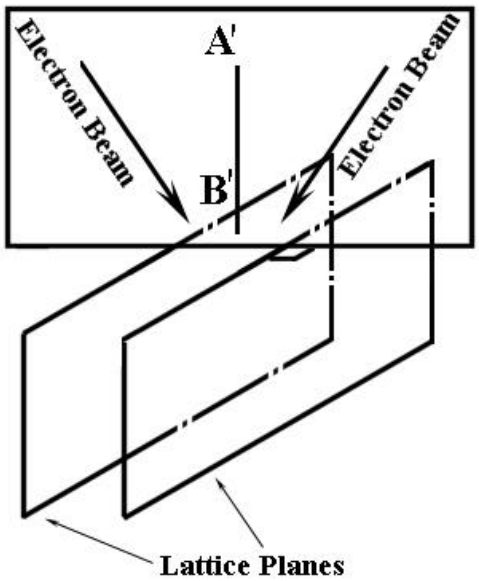

Figure 3-4. A schematic illustration of the mirror symmetry of the electron beam relative to a diffracting lattice plane set. The mirror plane can be any one that is parallel to the lattice plane set. A'B' is the intersection of the mirror plane with the plane shown on the top and perpendicular to the lattice plane set. The electron beams incident from both sides of A'B' are mirro-symmetric with each other, and hence will produce identical consequences.

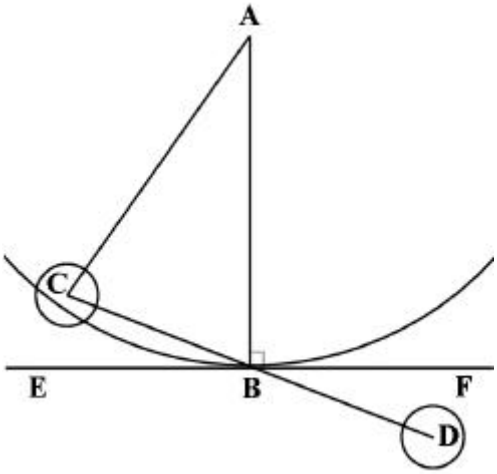

Figure 3-5. Schematic illustrating the configuration of the diffraction of a lattice plane set in which a reciprocal lattice spot intersects the Ewald sphere, hence the lattice fringes are visible. The arc centered at A represents part of the Ewald sphere. Segments BC and BD represent the reciprocal lattice vectors, i.e., BC = **g** and BD = -**g**. The circles centered at C and D represent the reciprocal lattice spots.

3.3.2.3 The Upper Limit of Transverse Tilt By "transverse tilt', we refer to one with the tilt direction perpendicular, or equally stated, the tilt axis parallel to, the lattice planes. Based on the above discussion, in tilting the crystal clockwise from the starting configuration, spot C will finally become tangent with the Ewald sphere from the inside of the Ewald sphere as shown in Figure 3-6, and be about to lose intersection with the Ewald sphere. The tilt thus reaches a critical value of $\angle EBC = \alpha_{max}$, which is the upper limit of transverse tilt and can be expressed as

$$a_{\max} = \sin^{-1}\left[\frac{df}{t} + \frac{l\,d}{2}\left(\frac{1}{d^2} - \frac{f^2}{t^2}\right)\right]. \tag{3-1}$$

Derivation of (3-1) is given in Appendix B1.

3.3.2.4 The Lower Limit of Transverse Tilt Again we will begin tilting from the same starting configuration as discussed in 3.3.2.1 in order to quantify the lower limit of transverse tilt. Together with the upper limit given in (3-1), the angular range for a transverse tilt within which lattice fringes are visibile can be specified.

3.3.2.4.1 ***Zero Lower Limit*** In the starting configuration, for any crystal whose diameter is below a certain limit, the reciprocal lattice spot is large enough to intersect (not necessarily be tangent with) the Ewald sphere, and the lattice fringes will be visible. Such an upper limit of crystal diameter is given as

$$t_0 = \frac{fd\,l}{\sqrt{d^2 + l^2} - d}. \tag{3-2}$$

Derivation of (3-2) is given in Appendix B2. When the crystal diameter is equal to t_0, i.e., $t = t_0$, the reciprocal lattice spots are tangent with the Ewald sphere from the outside, as shown in Figure 3-7. With smaller diameter, i.e., $t < t_0$, the reciprocal lattice spots intersect the Ewald sphere, as shown in Figure 3-8.

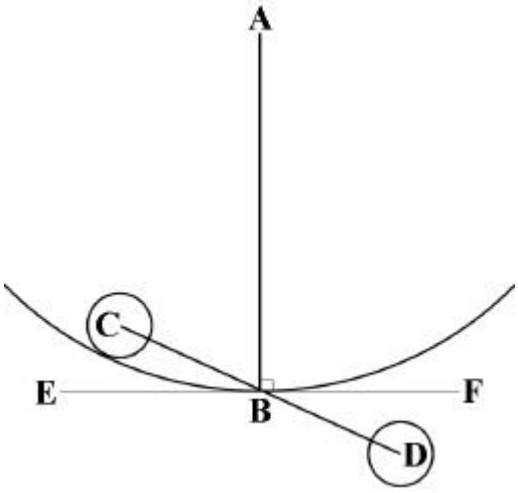

Figure 3-6. Schematic illustration of a configuration in which the reciprocal lattice spot considered becomes tangent with the Ewald sphere from the inside after tilt. The tilt axis points into the paper. The arc centered at A represents part of the Ewald sphere. Segments BC and BD represent the reciprocal lattice vectors, i.e., BC = **g** and BD = **-g**. The circles centered at C and D represent the reciprocal lattice spots.

In these two cases, the lower limits of transverse tilt are both zero. Lattice fringes are visible in the starting configuration, and will remain visible throughout a clockwise tilt, until the upper limit of transverse tilt, as given in (3-1), is reached. From the mirror symmetry discussed in 3.3.2.1, lattice fringes are also visible when the lattice plane set is tilted counterclockwise by an amount that is not greater than the upper limit of transverse tilt, α_{max}. Therefore the angular range of the incident electron beam relative to the lattice plane set within which the lattice fringes are visible is $2\alpha_{max}$ and continuous.

3.3.2.4.2 ***Non-Zero Lower Limit*** When the crystal diameter t is greater than t_0, i.e., $t > t_0$, the reciprocal lattice spots are so small that neither of the two spots intersects the Ewald sphere in the starting configuration, as shown in Figure 3-9 (a). The crystal has to be tilted clockwise until the reciprocal lattice spot C becomes tangent with the Ewald sphere, as shown in Figure 3-9 (b), in order for the lattice fringes to become

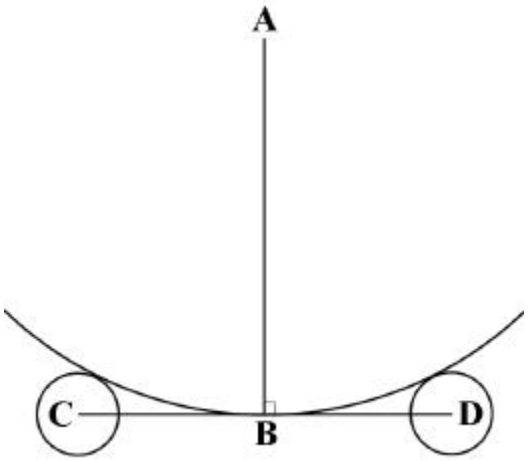

Figure 3-7. Schematic illustration of a configuration in which the electron beam is parallel to the lattice plane set and the reciprocal lattice spots are tangent with the Ewald sphere from the outside. The arc centered at A represents part of the Ewald sphere. Segments BC and BD represent the reciprocal lattice vectors, i.e., BC = **g** and BD = -**g**. The circles centered at C and D represent the reciprocal lattice spots. It is obvious that the relationship of CD⊥AB is true.

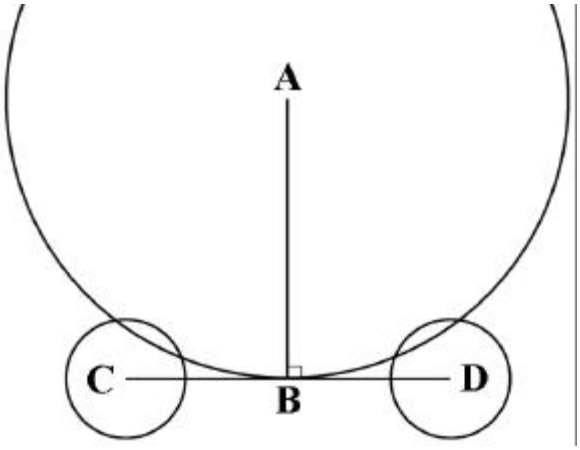

Figure 3-8. Schematic illustration of the configuration in which the electron beam is parallel to the lattice plane set and the reciprocal lattice spots intersect the Ewald sphere. The arc centered at A represents part of the Ewald sphere. Segments BC and BD represent the reciprocal lattice vectors, i.e., BC = **g** and BD = -**g**. The circles centered at C and D represent the reciprocal lattice spots.

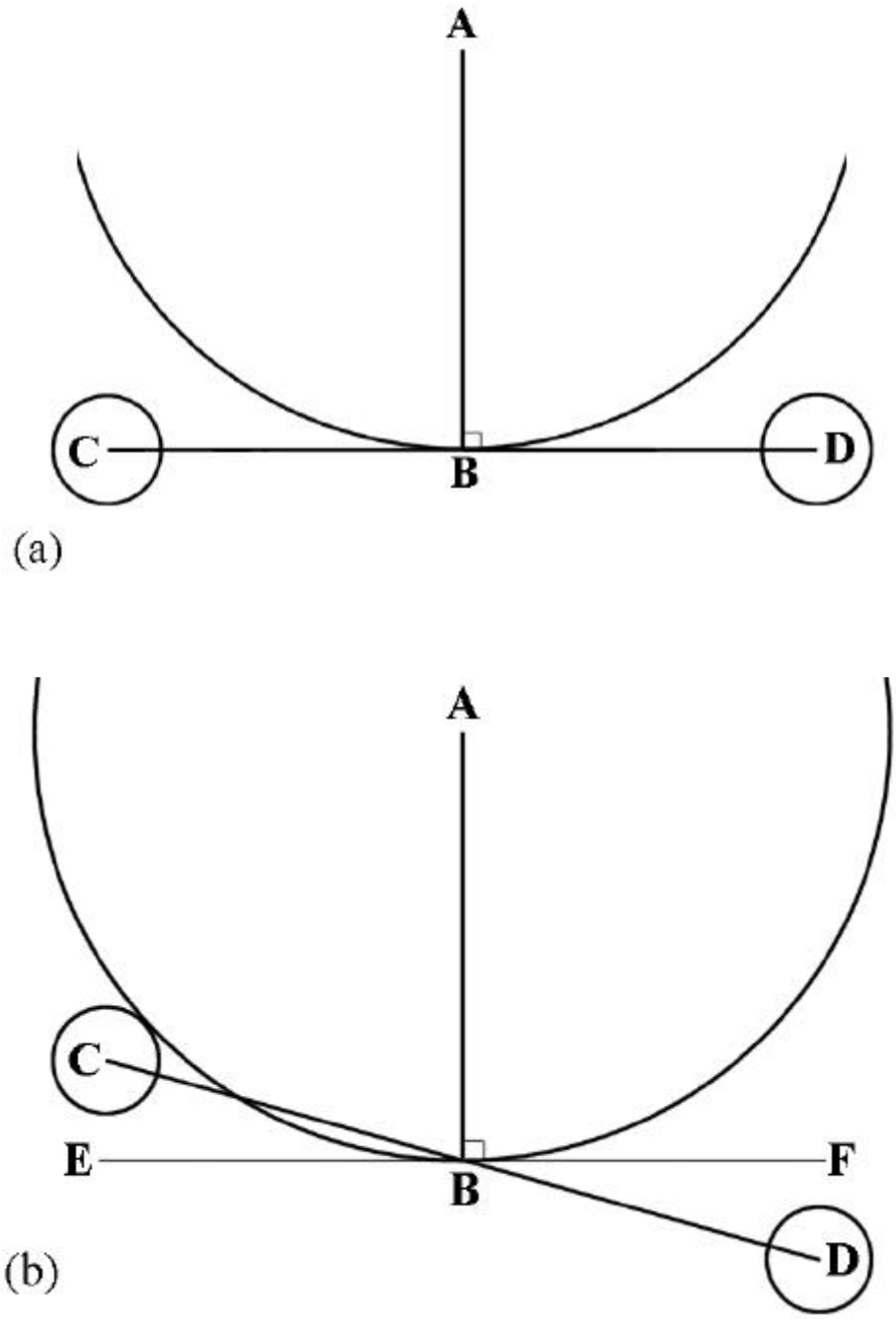

Figure 3-9. Schematic illustrating a non-zero lower limit of transverse tilt in order for the lattice fringes to become visible. The arc centered at A represents part of the Ewald sphere. Segments BC and BD represent the reciprocal lattice vectors, i.e., BC=**g** and BD=-**g**. When the electron beam is perpendicular to the reciprocal lattice vectors, i.e., AB ⊥ BC as shown in the (a) inset, neither of the reciprocal lattice spots, represented as spheres centered at C and D, intersects the Ewald sphere. Lattice fringes are hence invisible. Only when the lattice plane set is tilted clockwise until the reciprocal lattice spot C becomes tangent with the Ewald sphere, as shown in the (b) inset, will the lattice fringes begins to appear. The amount of tilt, which is equal to ∠EBC as shown in the (b) inset, is the lower limit of the transverse tilt.

visible. This lower limit of transverse tilt, denoted as α_{min}, can be expressed as

$$a_{\min} = \angle EBC = \frac{p}{2} - \angle ABC = \frac{p}{2} - \cos^{-1}\left(\frac{l t^2 - l f^2 d^2 - 2 ftd^2}{2dt^2} \right). \qquad (3\text{-}3)$$

Derivation of (3-3) is given in Appendix B3.

This is different from the above two cases in that the lattice fringes are *invisible* from the starting configuration, up to one when the amount of tilt reaches α_{min}, i.e., $\angle$EBC = α_{min} as shown in Figure 3-9 (b). Lattice fringe visibility is attained when the amount of tilt falls in between α_{min} and α_{max}, i.e., $\angle$EBC $\in$ [α_{min}, α_{max}], on either side of AB. Therefore the visibility range splits into two branches, each of which has a width of (α_{max} -α_{min}), and the amount of separation is 2α_{min}.

3.3.2.5 Visibility Band and Visibility Band Map Based on the above discussion, the concept of visibility band for a set of lattice planes can be introduced. A "visibility band" is defined on a sphere (on which every point represents a radially inward direction of the electron beam) such that, when the electron beam direction lies in the band, the lattice fringes are visible. The trace of the lattice plane set is represented as a great circle, which is a projection of the lattice plane set on the sphere. The trace runs through the middle of a visibility band, i.e., the visibility band is symmetric about the trace of the lattice planes. There are two kinds of visibility bands of a lattice plane set, a continuous one and a two-branch one, which will be discussed as follows.

In the case where the crystal diameter is not greater than the upper limit given by (3-2), i.e., t£ t_0, the visibility band is continuous and has a half width of α_{max}, as shown in Figure 3-10; Otherwise, the visibility band splits into two branches, which are symmetric about the lattice plane trace, as shown in Figure 3-11. The distance from the trace to the inner edge of a branch is α_{min}, while that to the outer edge is α_{max}. Thus each branch has a width of α_{max} - α_{min}.

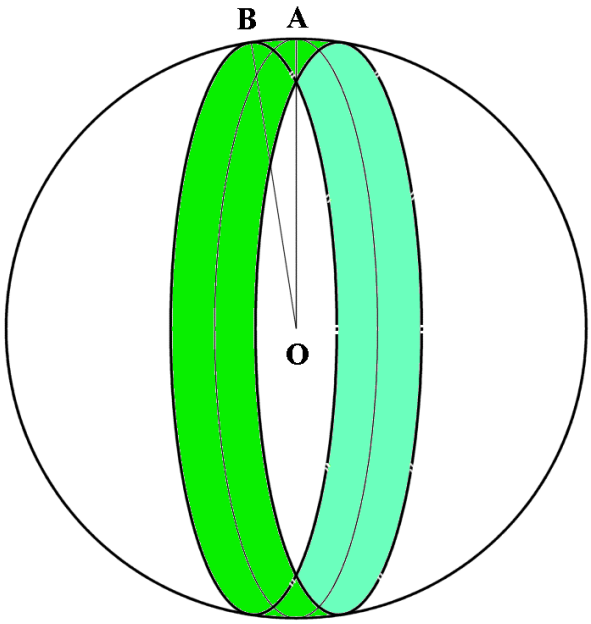

Figure 3-10. The visibility band (shaded) of a set of lattice planes in a spherical crystal. Such a band is so defined on a sphere that when the electron beam direction lies in it, the lattice fringes are visible. The great circle running through A is the trace of the lattice plane set. The crystal diameter is not greater than that given by (3-2), so that the band is continuous. The trace runs through the middle of a visibility band, i.e., the visibility band is symmetric about the trace. As the electron beam is tilted from any point along the trace in a plane perpendicular to the trace circle by an angle greater than $\angle AOB = \alpha_{max}$ as given by (3-1), the lattice fringes become invisible. Therefore this visibility band has a half-width of α_{max}.

From (3-1) the following approxiamation can be made

$$a_{\max} \cong \sin^{-1}\frac{df}{t} \cong \frac{df}{t} \propto d\ .$$

Therefore a visibility band is different from a Kikuchi band in that the band width is approximately proportional to the lattice spacing, which is one attribute of “direct space

The ensemble of the visibility bands of a spherical crystal can be drawn on the sphere of all possible directions, forming a “visibility band map
reveals the crystal lattice symmetry and spacing, but also is TEM-specific, i.e., only resolvable lattice plane sets have their bands on the map. Figure 3-12 shows a visibility

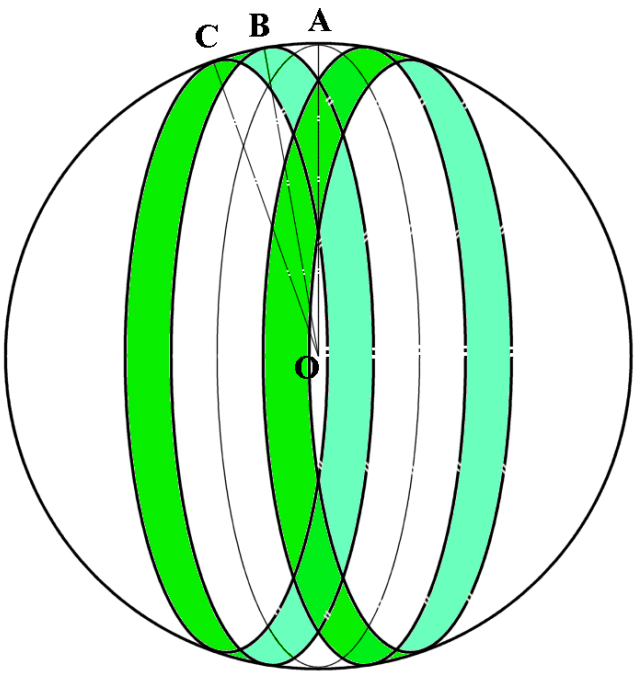

Figure 3-11. The visibility band of a set of lattice planes in a spherical crystal. The great circle running through A is the trace of the lattice plane set. The crystal considered here has a diameter greater that that given by (3-2), so that when the electron beam lies at any point along the trace the lattice fringes are invisible. However, as the electron beam is tilted away from the trace in a plane perpendicular to the trace circle, by an angle between α_{min} and α_{max}, where α_{min} and α_{max} are given in (3-1) and (3-3), respectively, the lattice fringes become visible. In the figure, $\angle AOB = \alpha_{min}$, $\angle AOC = \alpha_{max}$. Therefore the visibility band splits into two branches, which are symmetric about the lattice plane trace. The distance from the trace to the inner edge of a branch is α_{min}, while that to the outer edge is α_{max}. Thus each branch has a width of $(\alpha_{max} - \alpha_{min})$.

band map. Some examples to appreciate crystallographic information from such a visibility band map are given as follows.

In the figure, four crystal directions are marked. All the bands shown are continuous. The band perpendicular to the crystal direction of [010] is that of the (020) lattice planes, and that perpendicular to [001] is the zone of the (002) lattice planes, etc. The map contains bands of the {111}, {002} and {022} lattice planes, with those of the

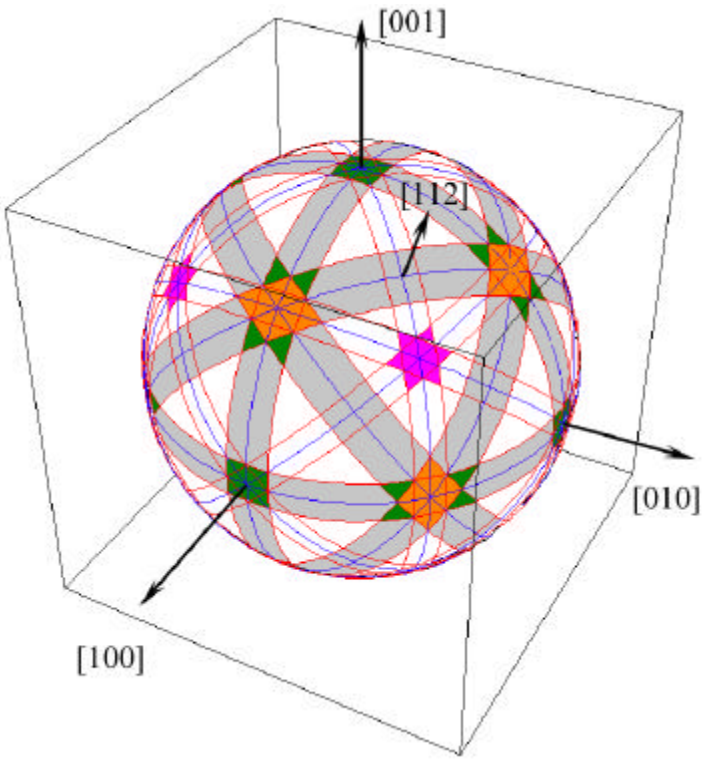

Figure 3-12. A visibility band map of a spherical fcc crystal. All the bands are continuous. Each band width is approximately proportional to the corresponding lattice spacing and the reciprocal lattice spots size. The band perpendicular to the [010] zone is that of the (020) lattice planes, and that perpendicular to the [001] zone is the band of the (002) lattice planes, and so on. Like a Kikuchi map, a visibility band map reveals crystal symmetry and can be used as a "roadmap" to guide (nano)crystallographic analyses in direct space. For example, the protocol used in Chapter 2 can easily be obtained from the map as to involve tilting from the [001] zone to the [112] zone. For a randomly oriented crystal, the solid angle subtended by each band is proportional to the probability for the corresponding lattice fringes to be visible, and the solid angle subtended by the cross-section of any two bands is proportional to the probability to get cross-lattice fringes from the corresponding lattice plane sets.

first two classes of lattice plane sets drawn as shaded. From the map it is obvious that the smallest lattice spacing of the crystal that can be resolved by the TEM is d_{220}.

3.3.2.6 General Visibility Range In general, T is not parallel to the lattice planes. The direction of T can be specified by the angle φ it makes with the reciprocal lattice vector g. Under such circumstances, the "visibility angular range" of the electron beam relative to the lattice planes is greater than the width of the visibility band. We will focus on the "visibility angular range" of a lattice plane set whose visibility band is continuous,

as discussed in 3.3.2.5 and shown in Figure 3-10. The study here will form the basis to predict lattice fringe visibility of the {111} and {002} lattice planes of the WC_{1-x} nanocrystals examined in the tungsten carbide thin films, since they all have continuous visibility bands, as will be shown in 3.3.3. Figure 3-13 shows a segment of such a visibility band.

In this figure, A'C' is the trace of the lattice plane set. A' is the starting electron beam direction. T is the tilt axis, **g** is the reciprocal lattice vector. T and **g** make an angle of φ. A'B' is the tilt path of the electron beam direction, and is half the total angular range θ of the electron beam within which the lattice fringes are visible (the other half is symmetric with A'B' about A'). Therefore it is denoted that A'B' = θ/2. Since A'B' is perpendicular to T, i.e., A'B'⊥T, it can be obtained that ∠B'A'C' = φ. B'C' is perpendicular to A'C', i.e., B'C'⊥A'C'. B'C' = α_{max} is equal to the half-width of the band. A'B', B'C', and C'A' are three arcs of three great circles, therefore it is true that

$$\sin B'C' = \sin j \ \sin\frac{q}{2},$$

i.e.,

$$\sin a_{max} = \sin j \ \sin\frac{q}{2}, \qquad (3\text{-}4)$$

where α_{max} is given in (3-1). Note that all the three angles, α_{max}, φ and θ, have positive values.

3.3.3. **Testing The Model** In the (a) insets of Figure 3-1, Figure 3-2 and Figure 3-3, the lattice fringes observed are those of the WC_{1-x} {111} and {002} lattice planes. In order to use equation (3-4) to predict their visibility after tilt, the crystal diameters must be respectively smaller than the upper limits predicted by (3-2), which are

$t_0(d_{111}$= 2.45 Å, f = 0.7902) = 482.6 Å, and

$t_0(d_{002}$= 2.12 Å, f = 0.7902) = 361.8 Å.

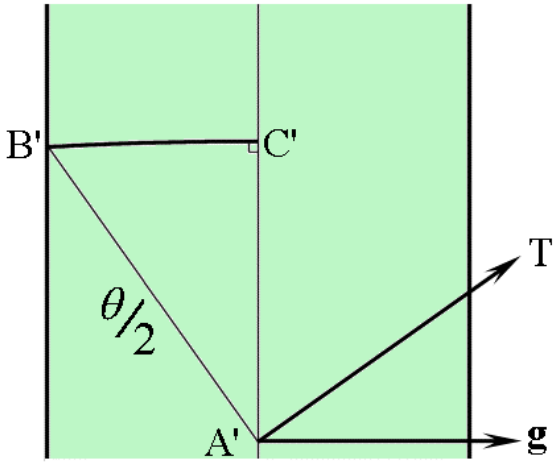

Figure 3-13. A segment of a continuous visibility band. A'C' is the trace of the lattice plane set. A' is the starting electron beam direction. **T** is the tilt axis, **g** is the reciprocal lattice vector. **T** and **g** make an angle of φ. B'C' = α_{max} is the half-width of the zone. A'B' is the tilt path of the electron beam direction, and is half the total angular range within which the lattice fringes are visible (the other half is symmetric with A'B' about A').

Both values are an order higher than those of the crystals shown in the (a) insets. Therefore all the fringes are within the application range of (3-4).

Lattice fringe invisibility after tilt can be predicted as follows. (3-4) is modified as

$$j = \sin^{-1}\left(\frac{\sin a_{\max}}{\sin\frac{q'}{2}}\right), \tag{3-5}$$

where the visibility angular range θ is replaced with θ', which denotes the amount of tilt used in the experiment. Corresponding to each θ', (3-5) outputs an upper limit of deviation of a reciprocal lattice vector from the tilt axis. If the actual deviation φ' as measured from the image is greater than φ, the lattice fringes are are predicted to be necessarily invisible after tilt. The implication of the analysis is that the reciprocal lattice vector deviates from the tilt axis so much that the reciprocal lattice spot necessarily loses intersection with the Ewald sphere after tilt.

Take those three sets of lattice fringes of crystal A shown in Figure 3-1(a), which are those of the WC_{1-x} (-1, 1, -1), (1, 1, -1) and (2, 0, 0) lattice planes, as examples. The average projection size of crystal A is about 48 Å. Euqation (3-5) predicts that for the given amount of tilt θ' = 14.5°,

$$\varphi(\, f = 0.7902,\ d_{111}=2.453\ \text{Å},\ 48\ \text{Å}, \theta' = 14.5°) = 20.6°, \text{ and} \qquad (3\text{-}6)$$

$$\varphi(\, f = 0.7902,\ d_{002}=2.124\ \text{Å},\ 48\ \text{Å}, \theta' = 14.5°) = 18.3°. \qquad (3\text{-}7)$$

The three lattice fringe vectors deviate from the projection of T_1 by 69.1°, 0.3°, 56.6°, respectively. Among them the first and the third are larger than their counterpart limits obtained in (3-6) and (3-7). Therefore, the (-1, 1, -1) and (2, 0, 0) lattice fringes are predicted to become invisible in Figure 3-1 (b). This is shown to be true. This way the invisibility of eleven lattice fringe sets are predicted, which is consistent with the HRTEM observation. The results are shown in Table 3-1.

In the (a) insets of the three figures, the eleven lattice fringe sets which are predicted to become invisible after tilt are labeled with hollow arrows. Please notice that all these lattice fringe sets disappear in the (b) insets, which is an indication of the consistency of the model with the HRTEM observations.

As an alternative to present the above results, Figure 3-14 shows two plots of $\varphi(f = 0.7902,\ d_{111}=2.453\ \text{Å},\ t, \theta' = 14.5°)$ and $\varphi(f = 0.7902,\ d_{002}=2.453\ \text{Å},\ t, \theta' = 14.5°)$. Also shown in the figure are the experimental data from Figure 3-1 (a). Hollow symbols are used to label lattice fringe sets that are observed to become invisible after tilt as shown in the (b) inset, and solid symbols for the rest. A consistency between the model and experimental observation is indicated, since all the hollow symbols are above their corresponding curves.

In contrast with the use of hollow arrows for lattice fringe sets that are predicted to become invisible after tilt, solid arrows are used to label the rest lattice fringe vectors in Figure 3-1, Figure 3-2, and Figure 3-3. Each of these lattice fringe vectors deviates from T by φ'which is measured from the images. The corresponding lattice fringe set has a certain probability to become invisible after tilt. The probability can be quantified as

Table 3-1. Correlating equation (3-5) in predicting lattice fringe invisibility after tilt with HRTEM observation as shown in Figure 3-1, Figure 3-2 and Figure 3-3. Quantities in the third and the fifth columns are obtained from the (a) insets in the figures.

Crystal	θ'(°)	t(Å)	Lattice Fringe Set	φ (°)	φ(°)	φ >φ ?	Predicted Invisible after Tilt?	Invisible in (b) Insets?
A	14.5	48	(1, 1, -1)	0.3	20.6	No	No	No
			(-1, 1, -1)	69.1		Yes	Yes	Yes
			(200)	56.6	18.3	Yes	Yes	Yes
B		56	{111}	24.6	17.8	Yes	Yes	Yes
C		42	{111}	11.8	23.4	No	No	No
D		46	(200)	57.5	19.0	Yes	Yes	Yes
			(020)	32.5		Yes	Yes	Yes
E		70	(1, 1, -1)	2.2	14.5	No	No	No
			(-1, 1, -1)	65.0		Yes	Yes	Yes
			(200)	58.2	13.1	Yes	Yes	Yes
F		48	(1, -1, 1)	67.1	20.6	Yes	Yes	Yes
			(1, 1, -1)	43.9		Yes	Yes	Yes
			(200)	11.8	18.3	No	No	No
G	30.6	76	{111}	0.5	6.4	No	No	No
H	35.26	100	(1, 1, -1)	0.6	4.4	No	No	No
			(-1, 1, -1)	68.4		Yes	Yes	Yes
			(200)	45.7	4.1	Yes	Yes	Yes

Notation used:

t: Average projection dimension of a crystal

follows. Equation (3-4) can be similarly modified as

$$q = 2\sin^{-1}\left(\frac{\sin a_{\max}}{\sin j'}\right), \tag{3-8}$$

where φ is replaced by φ'. Corresponding to each φ', (3-8) outputs an upper limit of

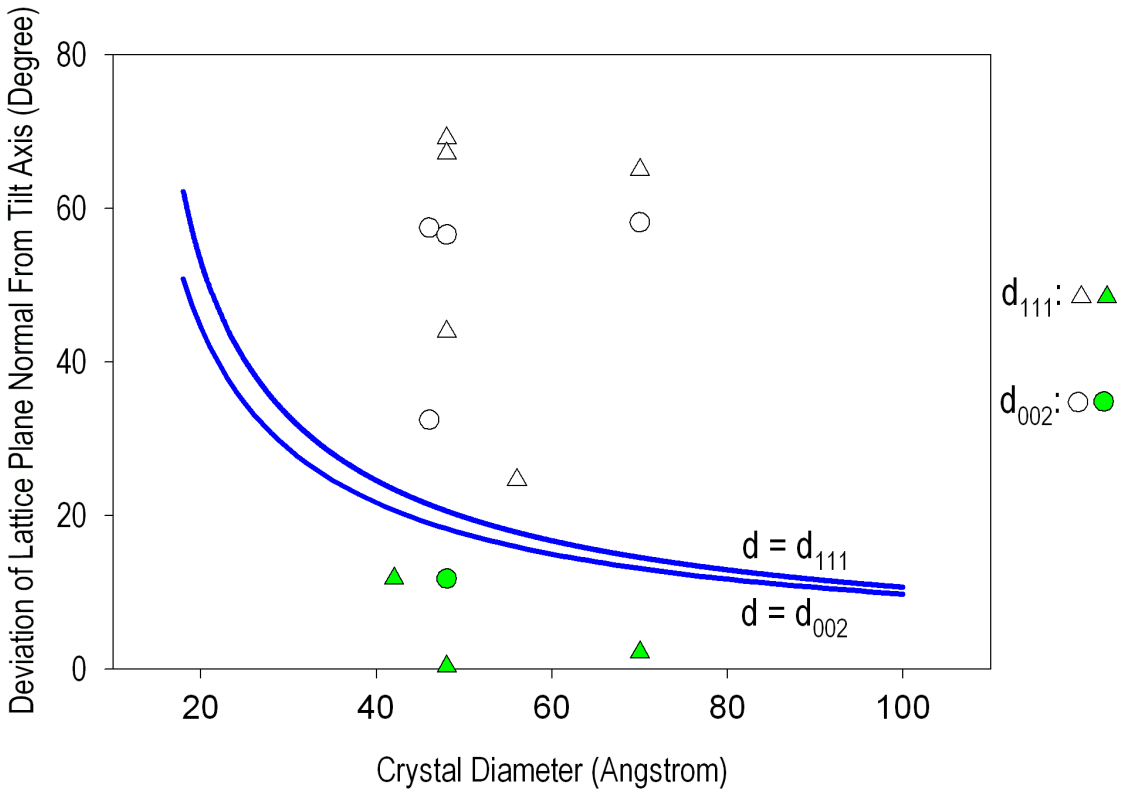

Figure 3-14. A plot of the maximum angular deviation of a reciprocal lattice vector from the tilt axis as given by (3-5), over crystal size. Above such a limit the reciprocal lattice spot necessarily loses intersection with the Ewald sphere after tilting the crystal by 14.5°. Experimental data from Figure 3-1(a) are also shown. The hollow symbols, including both circles and triangles, are used to denote the lattice fringe sets which are *observed* to become invisible after tilt as shown in Figure 3-1(b), and solid symbols for the rest lattice fringe sets. A consistency between the model and the HRTEM observation exists since all the hollow symbols are above their corresponding curves.

"visibility" angular range θ. If the actual amount of tilt θ' used in the experiment is greater than θ, the electron beam will be necessarily out of the "visibility" range after tilt, and the lattice fringes become invisible. This is equivalent to saying that fringes are only visible when the electron beam is perpendicular to any patch of the visibility band. In addition, since seeing the lattice fringes only means that the electron beam lies somewhere in the "visibility" range, but it is unknown exactly where the beam is in this range, the probability for the lattice fringes to become invisible after tilt can hence be quantified as

$$p_{invisible} = 0 \text{ , if } \theta = 180°; \text{ and}$$

$$p_{invisible} = \min\left[\frac{q'}{q},\ 1\right], \text{ otherwise.} \qquad (3\text{-}9)$$

Two examples of calculating pinvisible are given as follows. For the (1, 1, -1) lattice fringe vector of crystal A previously discussed, (3-8) gives

$$\theta(f = 0.7902,\ d_{111}=2.453\ \text{Å},\ t = 48\ \text{Å}, \varphi' = 0.3°) = 180°.$$

This means no matter how much the tilt is, the lattice firnges will never be invisible after tilt. Hence $p_{invisible} = 0$. For the (-1, 1, -1) lattice fringe vector of crystal A, equation (3-8) gives

$$\theta(f = 0.7902,\ d_{111}=2.453\ \text{Å},\ t = 48\ \text{Å}, \varphi' = 69.1°) = 5.4°,$$

Equation (3-9) in turn gives

$$p_{invisible} = \min\left[\frac{14.5^\circ}{5.4^\circ},\ 1\right] = 1.$$

Since the amount of tilt of 14.5° is greater than the visibility range of 5.4°, the electron beam is necessarily out of the visibility range after tilt, hence the lattice fringes will become invisible. This conclusion is consistent with that obtained through comparison of φ and φ' as presented before.

Similar analysis has been performed for all the rest of the fringe sets in Figure 3-1, Figure 3-2, and Figure 3-3. A consistency between the model and the HRTEM observations exists. The results are summarized in Table 3-2.

A new set of {111} fringes appears in Figure 3-1 (b). It is close to running horizontally. It is associated with another crystal overlapping with A and E. This crystal is bigger than both A and E in projection, since the fringe set expands beyond the perimeters of A and E after tilt. It has also been noticed from Figure 3-1 (a) that crystal E and F are twinned along one of their {111} planes.

Table 3-2. Correlating (3-8) and (3-9) with the HRTEM observation of lattice fringe visibility after tilts, as shown in Figure 3-1, Figure 3-2, and Figure 3-3. Quantities in the second and the fourth columns are obtained from the (a) insets in the figures.

Crystal	t(Å)	Fringe Set	φ (°)	θ (°)	θ(°)	θ > θ	$p_{invisible}$	Invisible in (b) Insets?
A	48	(1, 1, -1)	0.3	14.5	180	No	0	No
		(-1, 1, -1)	69.1		5.4	Yes	1	Yes
		(200)	56.6		5.4	Yes	1	Yes
B	56	{111}	24.6		10.6	Yes	1	Yes
C	42	{111}	11.8		28.4	No	0.51	No
D	46	(200)	57.5		5.6	Yes	1	Yes
		(020)	32.5		8.8	Yes	1	Yes
E	70	(1, 1, -1)	2.2		111.3	No	0.13	No
		(-1, 1, -1)	65.0		4.0	Yes	1	Yes
		(200)	58.2		3.9	Yes	1	Yes
F	48	(1, -1, 1)	67.1		5.5	Yes	1	Yes
		(1, 1, -1)	43.9		7.3	Yes	1	Yes
		(200)	11.8		22.3	No	0.65	No
G	76	{111}	0.5	30.6	180	No	0	No
H	100	(1, 1, -1)	0.6	35.3	180	No	0	No
		(-1, 1, -1)	68.4		2.9	Yes	1	Yes
		(200)	45.7		3.4	Yes	1	Yes

Notation used:

t: Average projection dimension of a crystal

3.4. DISCUSSION

3.4.1. **Potential Application of the Visibility Bands** We have investigated lattice fringe visibility after tilt. In this process the size of a reciprocal lattice spot is used, and the concepts of visibility band and visibility band map are introduced. A visibility band map contains information about not only the crystal, but also the TEM. The information incudes lattice symmetry, lattice spacing (as mentioned in 3.3.2.5), crystal size and shape [please refer to equation (3-1) and (3-3)], electron wavelength and point resolution. In short, like a Kikuchi map, a visibility band map is a "roadmap" to guide 3D (nano)crystallographic analyses in direct space. Two examples to use the visibility band map are given as follows.

3.4.1.1 Outputting Stereo Analysis Protocols Since both visibility bands of the resolvable lattice plane sets and crystal directions are shown in the map, stereo analysis protocols can be obtained from the map. For example, if we consider the map shown in Figure 3-12 as that of the 100 Å WC_{1-x} crystal A shown in Chapter 2, then the map will contain only the (shaded) {111} and {002} bands (since d_{220} is shorter than the point resolution). The protocol used in the tilt experiment described in Chapter 2 can then be easily obtained from the visibility band map.

3.4.1.2 Quantifying Probabilities For a randomly oriented crystal, the solid angle subtended by each visibility band is proportional to the probability for the corresponding lattice fringe set to be visible. Similarly the solid angle subtended by the cross-section of any two bands is proportional to the probability of obtaining the corresponding zone-images. Both can be quantified. For example, the probability of obtaining a [001] zone image is proportional to the solid angle of the cross-section of the (200) and (020) visibility bands, which is the "spherical square" that faces up as shown in Figure 3-12.

In Chapter 4 the probability of obtaining a [001] zone-image from a randomly oriented 100 Å WC_{1-x} crystal is calculated, but with a simplified treatment and hence the calculation is approximate. In this treatment, a spherical circle circumscribing the

above-mentioned “spherical square” is used. We have obtained no analytical solution for the solid angle subtended by the “spherical square”.

3.5. CONCLUSION

Here we present a model for predicting the visibility of a set of lattice fringes after tilt. This model was built based on the geometry between the reciprocal lattice spot and the Ewald sphere before and after tilt. It also employs a new concept of visibility band. Taking the reciprocal lattice spot size and the angle between the lattice fringe vector and the tilt axis into account, the model enables a determination of the total angular range of the incident electron beam relative to the lattice plane set within which the lattice fringes remain visible.

The model has been tested against the visibility variation of 17 sets of lattice fringes in two single-tilt and a double-tilt experiments. Two methods to predict the invisibility of lattice fringes after tilt have been used. In one of them, the experimentally used tilt is taken as the “visibility” angular range of the incident electron beam relative to the lattice plane set. The model subsequently outputs the maximum angular deviation of the lattice fringe vector from the tilt axis within which the lattice fringes will remain visible after tilt. Lattice invisibility is predicted through comparing the maximum angular deviation with the experimental data. In the second method, the angular deviation of the lattice fringe vector from the tilt axis is used to output the “visibility” angular range of the electron beam. The probability for the lattice fringe set to become invisible after tilt can be quantified as the ratio of the experimentally used tilt with the “visibility” angular range. Conclusions drawn by using these two methods are consistent with the experimental observations.

Only a HRTEM-resolvable lattice plane set has a visibility band. The band width is approxiately proportional to the size of the reciprocal lattice spots, and the lattice spacing. The solid angle subtended by the visibility band of a set pf lattice planes is proportional to the abundance of the lattice fringes. The visibility band map of a crystal carries the crystallographic information. It can be used as a roadmap in direct space crystallography. We have given two examples of the applications of the visibility band,

which are outputting the stereo analysis protocols, and quantifying the abundance of a certain lattice fringe set as well as that of a certain zone-image, which will be the subject of the next chapter. The persistent appearance of lattice fringes perpendicular to the (effective) tilt axis after different tilts supports the calibration of the projections of the tilt axes on HRTEM images.

4. PROBABILITY AND UNCERTAINTY IN STEREO LATTICE IMAGING

4.1. INTRODUCTION

Three-dimensional reconstruction in TEM is an established technique in both electron diffraction crystallography and electron tomography. These techniques share a common underlying principle in that each projection yields a single central plane of the examined object's 3D Fourier transform. Projections of the object along different views are combined to enable Fourier synthesis, after which 3D reconstruction is performed. Intrinsic symmetries of an object generally reduce the total number of necessary projections and the maximum tilt angle required (Frank, 1992b; DeRosier, 1968). Indeed, periodic lattices and quasi-periodic crystals offer one form of such simplifying symmetry (Hoppe, 1976). As a result, transmitted electron diffraction data at two tilts are often sufficient for inferring a 3D crystal lattice (Fraundorf,1981). With the availability of HRTEM, 3D crystallography in direct space became possible (Fraundorf, 1987). This technique has recently been applied in Chapter 2. There the 3D lattice parameters of a 10 nm f.c.c. WC_{1-x} crystal were measured by applying one of a finite set of data acquisition protocols (Qin, 1999; Qin, 2000a). In this protocol, the (002) and (020) lattice fringe vectors were acquired along the [001] zone, and (1, 1, -1) along the [112] zone.

For small crystals, reciprocal lattice spots expand broadly. This, in combination with the convergence of the incident electron beam, increases the chance to visualize lattice fringes as crystal orientation is varied (Qin, 2000c). Accordingly, the probabilities of success in each of the two data acquisition steps, and hence that for the overall experiment become higher. In HRTEM images each of which contains hundreds of nearly randomly oriented nanocrystals, this means that a significant fraction of crystals are already "correctly" oriented to present [001] zone images (from which two out of the three targeted reciprocal lattice vectors can be acquired). Acquisition of the third lattice fringe vector can be subsequently performed by adjusting the crystal azimuth, while retaining the [001] zone image configuration, then tilting to the [112] zone. By quantifying the probabilities of success, the feasibility of this technique for a given type

of specimen can be evaluated. Of course, the broadening of reciprocal lattice spots also introduces uncertainties in the corresponding reciprocal lattice vectors, as well as in the measured interplanar angles. Both the probabilities of success, and the resulting uncertainties, are of interest in the stereo lattice imaging of crystals and quasicrystals. In this paper we present semiempirical models for quantification of both.

4.2. EXPERIMENTAL DETAILS

The same gold/palladium specimen described in Chapter 3 was used to determinie the visibility factor f. HRTEM images of the same tungsten carbide thin film specimen described in Chapter 2 were used in analyzing probabilities and uncertainties. It is assumed that the WC_{1-x} nanocrystals have the same visibility factor.

4.3. RESULTS AND DISCUSSION: PROBABILITIES

Here there are two subsections. They concern the probabilities and uncertainties in stereo lattice imaging, respectively. Each subsection covers theory, observation, analysis and discussion.

4.3.1. Results

4.3.1.1 Theory: Cross-fringe Probability In the data acquisition protocol discussed, the overall probability of success is a product of those in the two data acquisition steps: find cross-fringes, then find a third set of fringes. For randomly oriented crystals, the bigger the corresponding reciprocal lattice spots are, the more likely they will intersect the Ewald sphere. Hence the probability of finding three linearly independent lattice fringe vectors increases. In section 2.6.2, two approaches to identify the basis triplet of a crystal lattice were mentioned.

In the first approach, any cubic crystal showing [001] zone cross-fringes is rotated (if necessary) until its (2, -2, 0) lattice planes become perpendicular to the tilt axis. It is then tilted over to the [112] zone. In this case the probability of success for any

randomly-oriented crystal is that of getting cross fringes along the [001] zone to begin with. The simultaneous tangent of the Ewald sphere with any two (which must be linearly independent of each other) of the four {002} reciprocal lattice spots along the [001] zone defines a maximum half angle θ_t between the electron beam and the zone axis. The solid angle, denoted as σ, subtended by a cone with this half-angle is proportional to the probability p_x that a randomly-oriented crystal will show the cross-fringes along the zone. A schematic, illustrating the principle to calculate the probability, is given in Figure 4-1. The probability p_x is actually proportional to the solid angle subtended by the cross-section of the (200) and (020) visibility bands, which is the "spherical square" that faces up and "normal" to the [001] direction in the visibility band map on the front page. An exact analytical solution for this has not yet been obtained. The above principle instead approximates the solid angle of the "spherical square" to that of a "spherical

For simplicity, we consider the case where the particle thickness in the electron beam direction, t, is fixed as the crystal orientation changes (e.g., as would be the case for spherical and/or equant crystals). The radius of a reciprocal lattice spot can then be expressed as

$$g_t = f/t\,,$$

where f is the visibility factor. As will be seen, g_t (and ultimately f) is the key quantity underlying all the subjects of discussion here. It affects the probabilities of success, the uncertainties of reciprocal lattice vectors and interplanar angles in stereo lattice imaging.

The probability of seeing <001> zone cross lattice fringes from a spherical crystal with a cubic lattice is

$$p_x(l,\,\mathrm{d},\,\mathrm{f}) = \frac{ns}{4p} = \frac{n}{2}(1-\cos q_t)\,, \qquad (4\text{-}1)$$

where n is the multiplicity of the zone (e.g., equal to 6 for <001> in cubic lattice). Derivations of (4-1), and the equations for σ and θ_t, which are given in (C-3) and (C-2), respectively, are in Appendix C1.1.

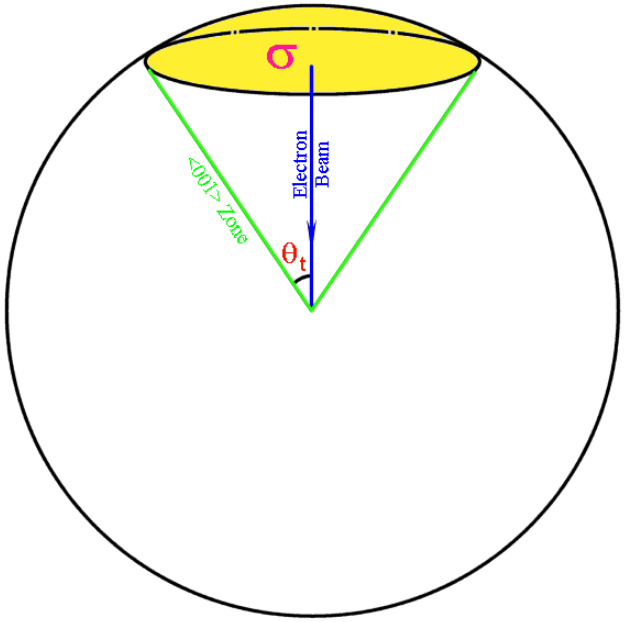

Figure 4-1. Schematic illustrating the principle to calculate the probability of seeing cross-fringes along the [001] zone axis of a randomly oriented crystal in HRTEM image. The upper limit for the deviation of crystal orientation from the exact Bragg condition, without losing cross fringes down the zone axis, is expressed as the maximum half-angle θ_t between the zone axis and the electron beam. The solid angle σ subtended by a cone with this half-angle is proportional to the probability that a randomly-oriented crystal will show the cross-fringes associated with that zone axis.

4.3.1.2 Observation: Cross-fringe Probability In determining f, three HRTEM images of the Au/Pd specimen were analyzed. An example image is shown in Figure 4-2. Please notice that in each "shaded region" there exists more than one single crystal, as is evident from the lattice fringes each of which spans an area that is smaller than the whole "shaded region".

It is assumed that each Au/Pd crystal in the images is spherical and randomly oriented and that its thickness in the electron beam direction is similar to its lateral size (this assumption is supported by the fact that only about 6.7% of the crystals have aspect ratios higher than three, and less than 1% above four). Two hundred and sixty-six nanocrystals were identified from the appearance of lattice fringes, and their projection

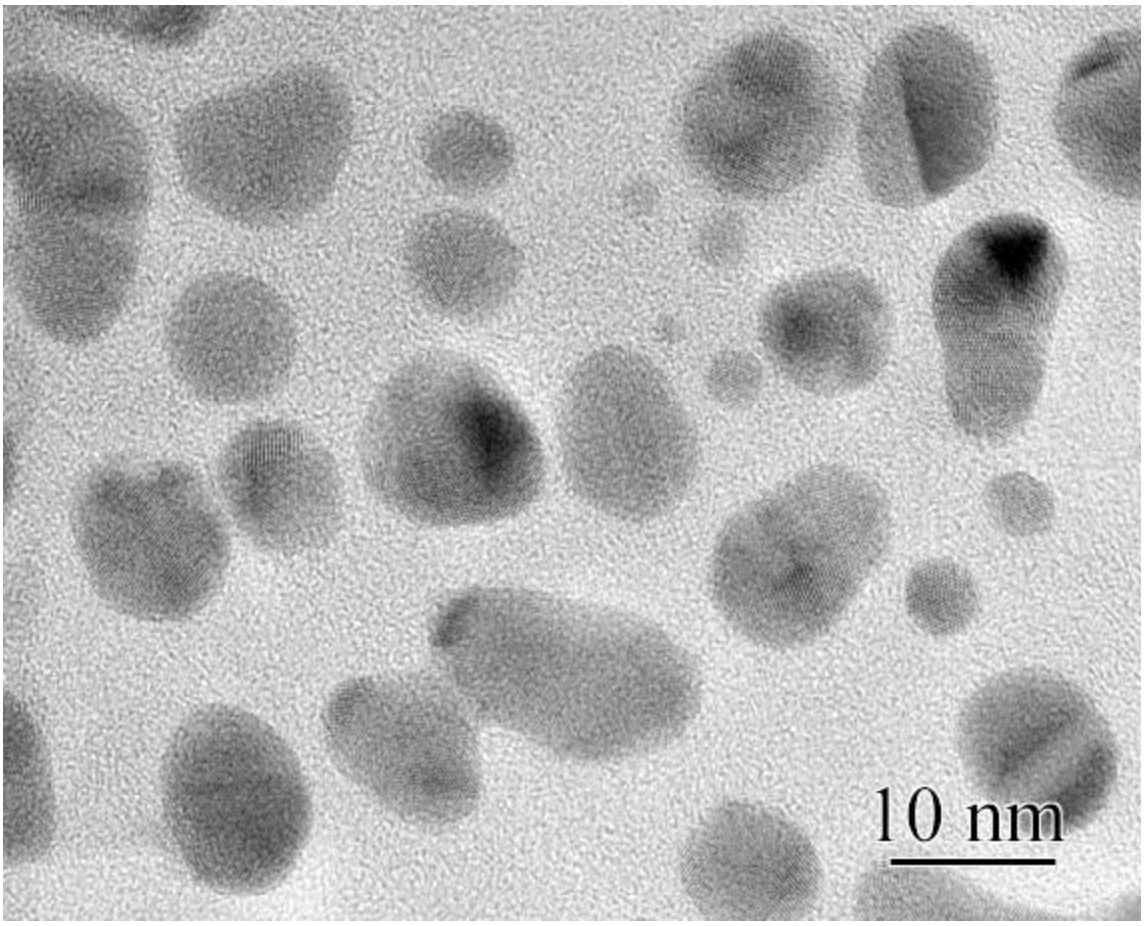

Figure 4-2. An HRTEM image of Au/ Pd sputtered on a thin carbon film. Images like this were used to empirically determined the proportionality coefficient in the relationship between a reciprocal lattice spot size and the radius of the corresponding crystal.

sizes range from 2 nm to 6 nm. Among them 6 show {002} cross fringes along <001> zones. The number of the remaining crystals could not be counted exactly due to the invisibility of lattice fringes. Their presence was identified through the mass-thickness contrast, i.e., the presence of the "shaded regions" against the carbon film background. The total area they cover is about twice that of the area showing lattice fringes. Therefore the total number of nanocrystals is estimated to be three times as high, i.e., 3×266=798. The statistics are shown in the following Table 4-1.

Table 4-1. Statistics of crystals showing <001> zone fringes in three HRTEM images of a Au/Pd/C specimen.

t(Å)	$\bar{t}$ (Å)	σ_t(Å)	N	$n_{<001>}$	$p_x = \frac{n_{<001.>}}{3n}$ (10^{-3})
[20, 40]	31.2	5.7	169	5	9.86
(40, 60]	50.0	5.9	97	1	3.43

Notations:

t: Average crystal dimension

σ_t: Standard deviation of crystal diameter

$n_{<001>}$: Number of crystals showing <001> fringes

n: Number of crystals showing lattice fringes and hence each of which is identified as a crystal

p_x: Estimated fraction of crystals showing <001> zone fringes

4.3.1.3 Analysis: Cross-fringe Probability Equation (4-1) was used to least-square fit the values of p_x in Table 4-1 by adjusting f. In other word, f was adjusted so the relationships

$$p_x(t = \bar{t} = 31.2 \text{ Å}, \text{d} = 2.04 \text{ Å}, \text{f}) = 9.86 \times 10^3, \text{ and}$$

$$p_x(t = \bar{t} = 50.0 \text{ Å}, \text{d} = 2.04 \text{ Å}, \text{f}) = 3.43 \times 10^3$$

are true. The value of f thus determined is 0.79. With such a value of f, a plot of $\theta_t(t)$ is shown in Figure 4-3. it can be seen that θ_t rapidly decreases over increasing crystal diameter. It drops down to less than ten degrees for t > 1.4 nm. Therefore in this size range, the maximum deviation of the zone axis from the electron beam must be on the order of 1^o in order for the cross-fringes to be visible. For example, θ_t equals 4.75° when t equals 3 nm. θ_t equals 1.84^o when t equals 9 nm. As a result, the solid angles subtended and hence the probabilities of finding cross-fringes along the [001] zone become very small. For example, the probability p_x is less than 5% for t > 1.4 nm, as will be seen in the following discussion.

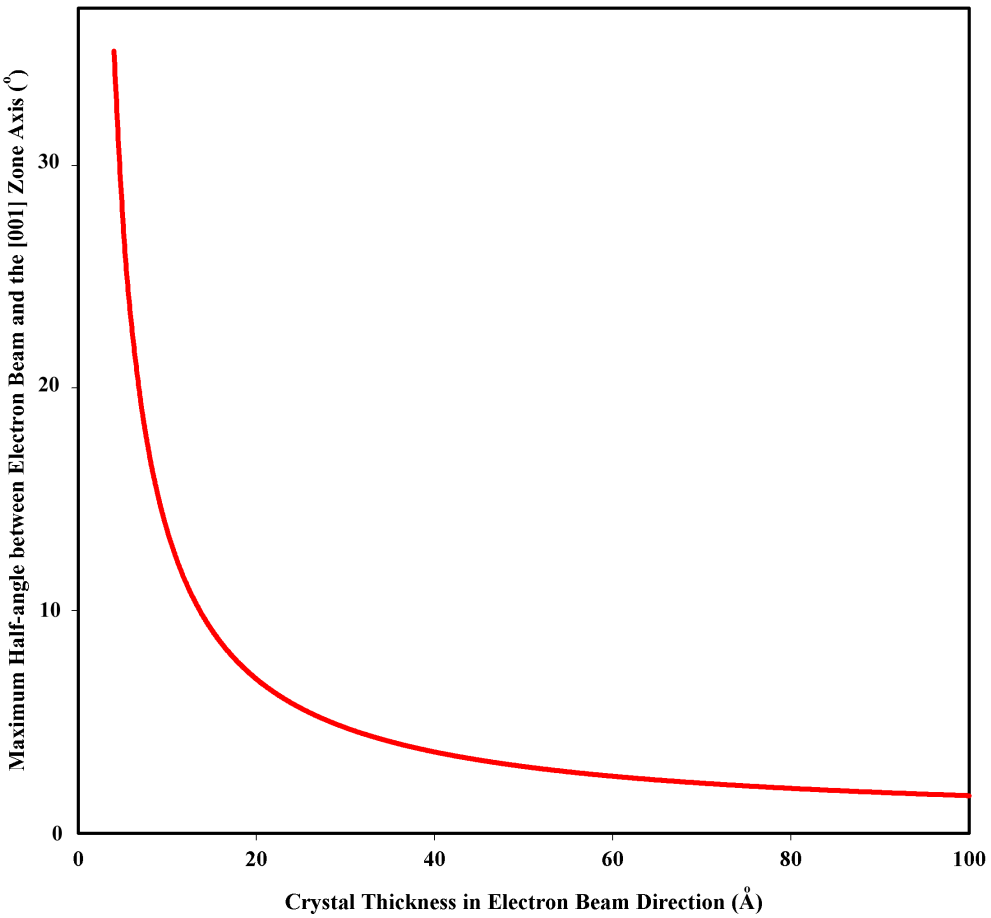

Figure 4-3. The maximum half-angle, θ_t, between the [001] zone of a spherical cubic nanocrystal and the electron beam as a function of crystal diameter. When the [001] zone deviates from the electron beam by an amount that is not greater than θ_t, cross lattice fringes along the [001] zone will be visible.

A plot of the probabilities of seeing <001> zone cross-fringes ($d_{\{002\}}$ = 2.04 Å) from Au/Pd crystals on the thin carbon film, as a function of crystal diameter t, together with the two experimental data points, is shown in Figure 4-4. As is evident from the figure, the probability of encountering cross-fringes improves greatly as crystallite size decreases toward a nanometer. However, this “reciprocal lattice broadening" is accompanied by an increase in the uncertainties of lattice fringe spacings and interplanar angles as well.

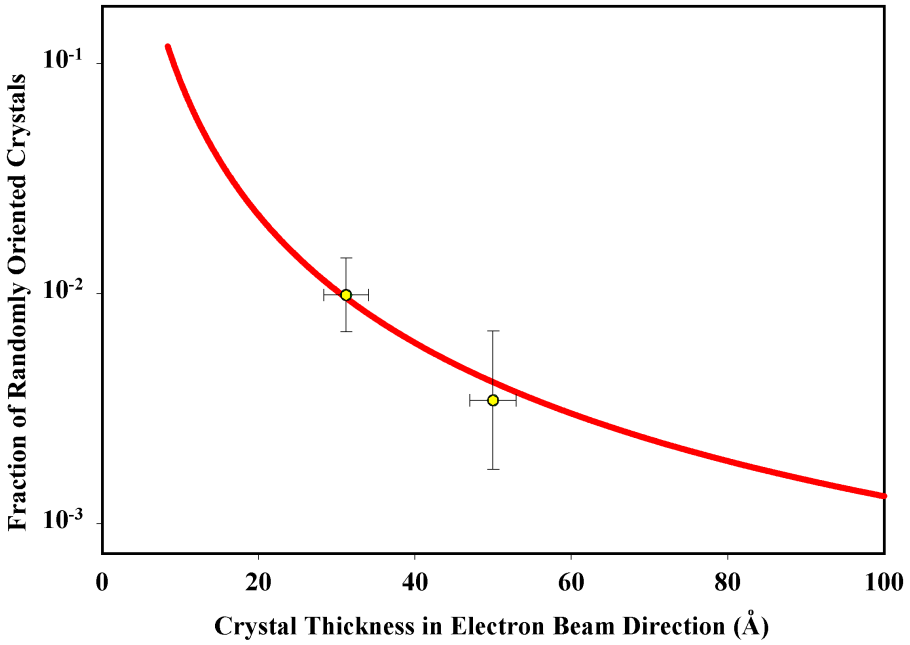

Figure 4-4. Fraction of spherical Au/Pd crystals showing cross lattice-fringes along a <001> zone as a function of crystal diameter, together with the experimental data points obtained from HRTEM images of Au/Pd particles evaporated on a thin carbon film.

Corresponding to each crystal diameter t, there exists a maximum percent difference δ between the lattice spacing d and the observed fringe spacing d', i.e., δ is such that the following relationship

$$d = \left|d' - d\right| / d$$

is satisfied.

For spherical nanocrystals, t and δ obey the following relationship of

$$g' = \frac{1}{d'} = \frac{g}{1+d} = \sqrt{\frac{g^2 - g_t^2}{1 - \frac{g_t}{g_l}}}\,. \qquad (4\text{-}2)$$

Derivation of (4-2) is given in Apendix C1.2. It can equally be stated that when a certain upper limit of tolerable percent difference δ is imposed, there exists a corresponding lower limit of crystal diameter t_{min}. Below such a lower limit of t_{min}, the reciprocal lattice spots are so large that the maximum percent difference between lattice spacing d and the

observed fringe spacing d' will be greater than δ. In plotting Figure 4-4, δ = 2% is imposed, equation (4-2) yields t_{min} = 8.0 Å. The curve thus begins from t = 8.0 Å.

Another plot of the probability of seeing <001> zone cross lattice-fringes of WC_{1-x} crystals, as a function of crystal diameter is shown in Figure 4-5. With the same amount of δ = 2% imposed, (4-2) yields t_{min} = 8.3 Å. The curves thus begins from t = t_{min} = 8.3 Å.

In order for the equation (4-1) to be valid in quantifying the probability p_x, the four {002} reciprocal lattice spots along a <001> zone must be large enough so that when the zone axis is parallel to the electron beam, the Ewald sphere still intersects these reciprocal lattice spots. This imposes an upper limit of the crystal diameter. Such an upper limit has the form of

$$t_{\max} = \frac{fd^2}{l} + fd\sqrt{\frac{d^2}{l^2}+1}\,. \qquad (4\text{-}3)$$

Derivation of (4-3) is given in Appendic C1.3. For WC_{1-x} crystals, t_{max} is predicted to be about 320 Å.

Equation (4-1) predicts the probability of seeing <001> zone fringes from a 10 nm WC_{1-x} crystal as

$$p_x(l = 100\ \text{Å},\ \text{d} = 2.12\ \text{Å},\ \text{f} = 0.79) = 1.377\times 10^{3} \simeq \frac{1}{726},$$

i.e., one out of about seven hundred 10-nm crystals shows cross fringes along <001>. This is also the probability of success in a TEM with a single-axis tilt of at least ±35.3° and a stage capable also of 90° rotation as discussed previously.

4.3.1.4 Theory: Probability of Finding a Third Lattice Fringe Set The second approach to determining a basis triplet, mentioned in section 2.6.4, works when the microscope tilt limitations do not allow choice of the tilt axis direction from the cross-fringe position. For the probability of success, we must multiply p_x by that of viewing a set of {111} fringes *after* tilting a <001> crystal with a random aziumth by 35.3°. This

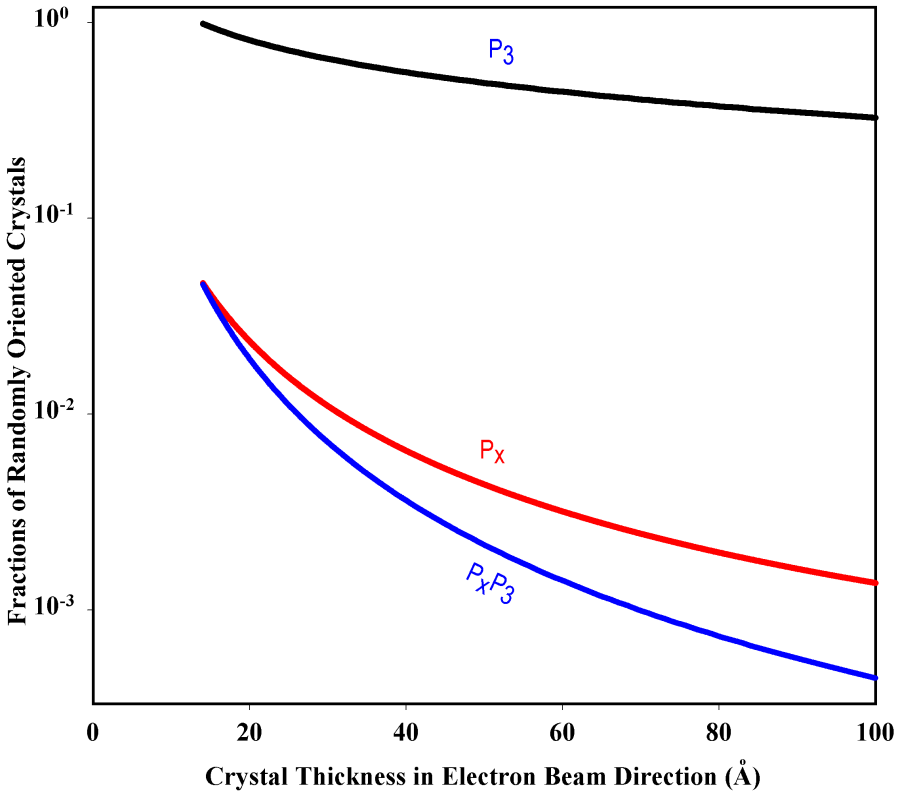

Figure 4-5. Different fractions of spherical WC_{1-x} crystals as functions of crystal diameter. These fractions of crystals include that of showing cross lattice-fringes along a <001> zone, p_x, that of showing the (1, 1, -1) lattice fringes after tilting a <001> WC_{1-x} crystals with random azimuth by 35.3°, p_3, and the product of p_xp_3. Such a product is the overall probability of success to acquire the three targeted reciprocal lattice vectors in a stereo lattice imaging protocol to infer the 3D lattice of a spherical f.c.c. crystal.

probability, denoted as p_3, is proportional to an "azimuthal tolerance half-angle" φ, which is an acute angle between the reciprocal lattice vector (2, -2, 0) and the tilt axis. When the reciprocal lattice vector (2, -2, 0) deviates from the tilt axis by an amount that is less than this "azimuthal tolerance half-angle", (1, 1, -1) lattice fringes will appear after a tilt of the azimuthally random <001> crystal by 35.3°. The probability p_3 has the form

$$p_3 = mj\ /p\ , \tag{4-4}$$

where m is the multiplicity of equivalent tilt direction (e.g., m = 4 for the (2, -2, 0) plane set in our experiment). An equation to determine φ is given in equation (C-14) in Appendix C2.1. When using the visibility band map on the front page, tilting an azimuthally random [001] crystal by 35.3° leaves the electron beam to a point in a circle

that is 35.3° away from the [001] zone axis. This circle will intersect the (1, 1, -1) visibility band. The ratio of the total length of arc of the circle within the (1, 1, -1) visibility band with the circumference of the circle is equal to the probability of getting the (1, 1, -1) lattice fringes after tilting. Such a probability multiplied by the multiplicity of 6 of a <001> zone is equal to the probability p_x. The result here, although obtained by a different approach, is still an exact solution.

The probability p_3 is also plotted in Figure 4-5, along with its product with p_x, i.e., $p_3p_x(t)$. Corresponding to each crystal diameter t, there similarly exists a maximum percent difference δ between the lattice spacing d and the fringe spacing d'. t and δ obey the following relationship of

$$g' = \frac{1}{1+d}\, g = \sqrt{g^2 + g_t^2 - g_t \frac{g^2 + g_t^2 + 2 g_l g_t}{g_l + g_t}}\,. \qquad (4\text{-}5)$$

A derivation of (4-5) is given in Appendix C2.2. A tolerance limit of $\delta = 2\%$ is also imposed in the plot pf $p_3(t)$. Similarly, the curve begins from $t = t_{min} = 8.7$ Å.

In order for expression (4-4) for p_3 to be valid, the (1, 1, -1) reciprocal lattice spot must be large enough to intersect the Ewald sphere after the 35.3° of tilt. This imposes an upper limit on the crystal diameter. Such an upper limit is of the form:

$$t_{\max} = \frac{fd^2}{l} + fd\sqrt{\frac{d^2}{l^2} + 1}\,. \qquad (4\text{-}6)$$

A derivation of (4-6) is given in Appendix C2.3. For WC_{1-x}, t_{max} here equals about 360 Å.

4.3.1.5 Analysis: the Overall Probability Based on the above discussion, the overall probability of success with the strategy adopted in our experiment, for the 10 nm WC_{1-x} crystals, can be quantified as $p_xp_3 = (1.377\times10^{-3})\times(0.325) = (1/726)\times(0.327) = 4.50\times10^{-4}$ @ 1/2221. Hence, only one in about every seven hundred crystals will show [001] cross fringes and one in about every two thousand will be suitably oriented for 3D lattice parameter determination. This is not inconsistent with our experience: The image of crystal A was recorded in one pair of negatives out of 22, while each negative provides a view of approximately 100 crystals.

4.3.2. Discussion

4.3.2.1 Probabilties in High-tilt-rotate TEM As discussed in 2.6.2, when the TEM is capable of both ±35.3° tilt and 90° rotation, lattice parameters could have been determined for any cubic crystals showing <001> zone cross-fringes when untilted. From Figure 4-5, the fraction of spherical particles, 3 nm in diameter oriented suitably for such analysis goes above 1%, i.e., $p_x(t = 3.0 \text{ nm}) = 1.1\%$. Moreover, with a goniometer capable of tilting by ±45° plus computer support for automated tilt/rotation from any starting point, each unobstructed nanocrystal in the specimen could have been subjected to this same analysis after a trial-and-error search for accessible <001> zones. Thus a significant fraction of crystals in a specimen become accessible to these techniques, with either a large enough range of computer-supported tilts, or if the crystals are sufficiently thin.

4.3.2.2 Probability of Finding a Third Lattice Fringe Set The following discussion is dedicated to the tilt dependence of p_3. Figure 4-6 shows a plot of p_3 as a function of the amount of tilt needed to bring the third reciprocal lattice spot to the image plane. Here the crystal diameter is t = 100 Å, and the third lattice spacing is d = 2.453 Å. It is assumed that after such an amount of tilt the spot will intersect the Ewald sphere. The function approaches 1 as the amount of tilt approaches zero. In the case of zero tilt, it means the third lattice fringe vector can be acquired without tilting, i.e., it is along the first zone axis. However, all three reciprocal lattice vectors being along the same zone does not enable the inference of the lattice of the imaged crystal in 3D since they are not linearly independent. This means the zero tilt case does not satisfy the condition of stereo lattice imaging, and shall thus be excluded in the plots. In the plot an open circle has been used to represent the zero-tilt point.

At the other extreme, when the tilt equals 90°, it is interesting to note that the probability is again equal to 1, i.e., $p_3 = 1$. This can be explained as follows. The tilt

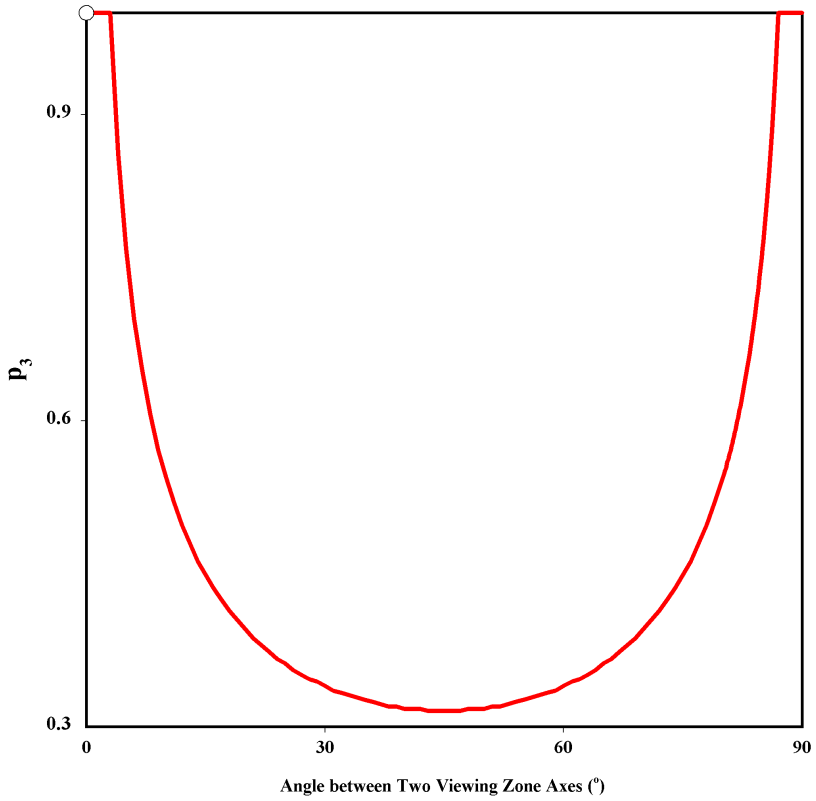

Figure 4-6. Fraction of spherical crystals showing one set of lattice fringes as a function of the amount of tilt to bring the corresponding reciprocal lattice vector to the image plane. Here the crystal diamtere is t = 100 Å, and the lattice spacing is d = 2.453 Å.

being equal to 90° means that the third reciprocal lattice vector is parallel to the electron beam before the tilt. Hence the crystal azimuth will make no difference in the position of this reciprocal lattice vector after tilting, i.e., the third reciprocal lattice vector will always be lying on the image plane after tiltnig no matter how the crystal is azimuthally oriented before the tilt. For this crystal with a diameter of t = 100 Å, the corresponding reciprocal lattice spot is large enough to intersect the Ewald sphere. Hence lattice fringes would be visible in HRTEM images regardless of the initial crystal azimuth, and consequently, the probability p_3 is equal to 1.

From Figure 4-6, it is apparent that the probability of acquiring the third lattice fringe vector is lowest for tilts that are most likely to be involved in crystallography, i.e., between 20° and 70°. In this tilt range, however, the probability of success is cut down from 1 by a factor of just less than 3, owing to the finite size of the reciprocal lattice spot.

4.4. RESULTS AND DISCUSSION: UNCERTAINTIES

Stereo diffraction analysis, and the typical size of diffraction broadening in TEM, suggest that the lattice spacing uncertainty from stereo experiments may in favorable circumstances be on the order of 1%, and angular errors on the order of 1° (Fraundorf, 1987). Experiments with stereo image analysis in Chapter 2, and a more detailed look at the theory here, now support this impression. We will focus the discussion again on spherical nanocrystals. The primary cause of the uncertainties is the expansion of a reciprocal lattice point, i.e., increasing relaxation in the Bragg condition, as crystal size gets smaller.

4.4.1. Results Similar to a treatment in the earlier work, the sources from which uncertainties (e.g., in orientation and camera constant) arise are assumed to be uncorrelated in our models (Fraundorf, 1987; Bevington, 1969). In the expressions below, we use subscript x to denote the component of a quantity in the horizontal image plane, and z, along the direction of the electron beam. The Ewald sphere is assumed to be flat. The angle θ is the amount of tilt to bring a reciprocal lattice vector to the horizontal image plane (hence Bragg condition), and λL is the camera constant of the digitized images.

4.4.1.1 Theory: Reciprocal Lattice Vector Uncertainty in Image Plane The three sources contributing to the uncertainty of a reciprocal lattice vector in the image plane are: the lateral uncertainty of the corresponding reciprocal lattice spot in the image plane, the uncertainty of the camera constant of the power spectrum, and the uncertainty of the reciprocal lattice spot along the electron beam direction, in order of decreasing relative effect. It is worth noting that such an uncertainty equals that of the corresponding lattice fringe spacing, i.e., the following relationship

$$\frac{d\,d}{d} = \frac{d\,g}{g} \tag{4-7}$$

is true and this is proved in Appendix C3.1. Also, we treat uncertainty of spot location in the plane perpendicular to the electron beam direction in a very simplified way here as equal to the reciprocal lattice spot radius. With the contributions from the above sources listed in order, the uncertainty of a reciprocal lattice vector has the form of

$$\left(\frac{dg}{g}\right)_x = \sqrt{\left(\frac{fd}{t}\right)^2 + \left[\frac{d(lL)}{lL}\right]^2 + \left[\frac{1}{2}\left(\frac{fd}{t}\right)^2\right]^2}\,. \qquad (4\text{-}8)$$

This equation is valid under the condition of $(fd/t)^2 << 1$, i.e., t >> fd. For the visibility factor of f = 0.79, the products of fd for WC_{1-x} nanocrystals are close to 2 Å, i.e., f $d_{111} \approx$ 2.0 Å, f $d_{200} \approx$ 1.8 Å. Therefore, in evaluating the uncertainties of $(dd/d)_{x,\,200}$ and $(dd/d)_{x,\,111}$, the equation is applicable when the crystal has a diameter of t >1 nm. Derivation of (4-8) is given in Appendix C3.2.

The sources of the uncertainty in camera constant are the magnification variations of both the microscope (operated at a certain magnification setting), and the image-digitizing process. Such an uncertainty, evaluated from the camera constants of 10 HRTEM images taken during a time period of eight months, is 0.5% for our microscope.

For the {111} lattice spacing (d_{111} = 0.245 nm) of WC_{1-x}, as the crystal diameter t increases from 1 nm to 10 nm, the uncertainty from the first source decreases from 0.19 to 0.019, and its ratio with that from the third source increases from about 10 to about 100. It follows that for nanocrystals most of the spatial measurement uncertainty arises from the lateral uncertainty of the reciprocal lattice spot in the image plane.

4.4.1.2 Theory: Reciprocal Lattice Vector Uncertainty out of Image Plane

Sources responsible for the uncertainty of a reciprocal lattice vector along the electron beam direction consist of those of the camera constant of the power spectrum and the goniometer tilt, and that of the reciprocal lattice spot along the electron beam direction. Our model predicts the following equation of

$$\left(\frac{dg}{g}\right)_z = \sqrt{\left[\frac{d(lL)}{lL}\right]^2 + \left(\frac{dq}{\tan q}\right)^2 + \left(\frac{fd}{t\sin q}\right)^2}\,, \qquad (4\text{-}9)$$

from the untilted orientation, respectively. The tilt uncertainties around both tilt axes are 0.5°, giving rise to an angular uncertainty of $\delta\theta = 0.7°$ around the effective tilt axis. Equaitons (4-8), (4-9), and (4-10) predict the following uncertainties of

$$\left(\frac{dg}{g}\right)_{200,x} = 1.75\%,$$

$$\left(\frac{dg}{g}\right)_{111,x} = 2.00\%,$$

$$\left(\frac{dg}{g}\right)_{111,z} = 7.48\%, \text{ and}$$

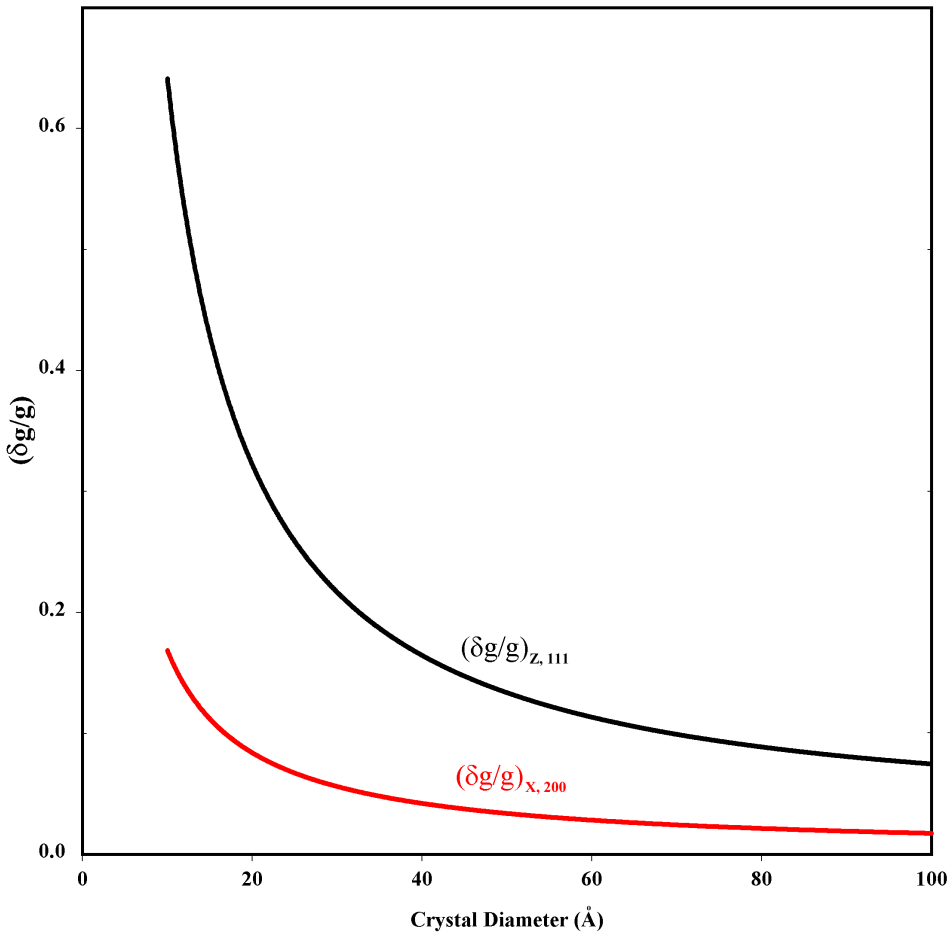

Figure 4-7. Uncertainties of the {200} reciprocal lattice vectors in the image plane and the vertical component of the {111} reciprocal lattice vectors along the electron beam direction in HRTEM images for spherical WC_{1-x} crystals as functions of crystal diameters.

$$(dj)_{200,\,x} = 1.92^{\circ},$$

where the three-number indices are the Miller indices of the reciprocal lattice vectors. The large "out-of-plane" uncertainty $(dg/g)_z$ predicted here is a result of the small tilt range available in our HRTEM. These values given above, together with the percent differences between their experimental counterparts and the literature values, the percent errors, are listed in Table 4-2. It can be seen that the model-predicted uncertainties are

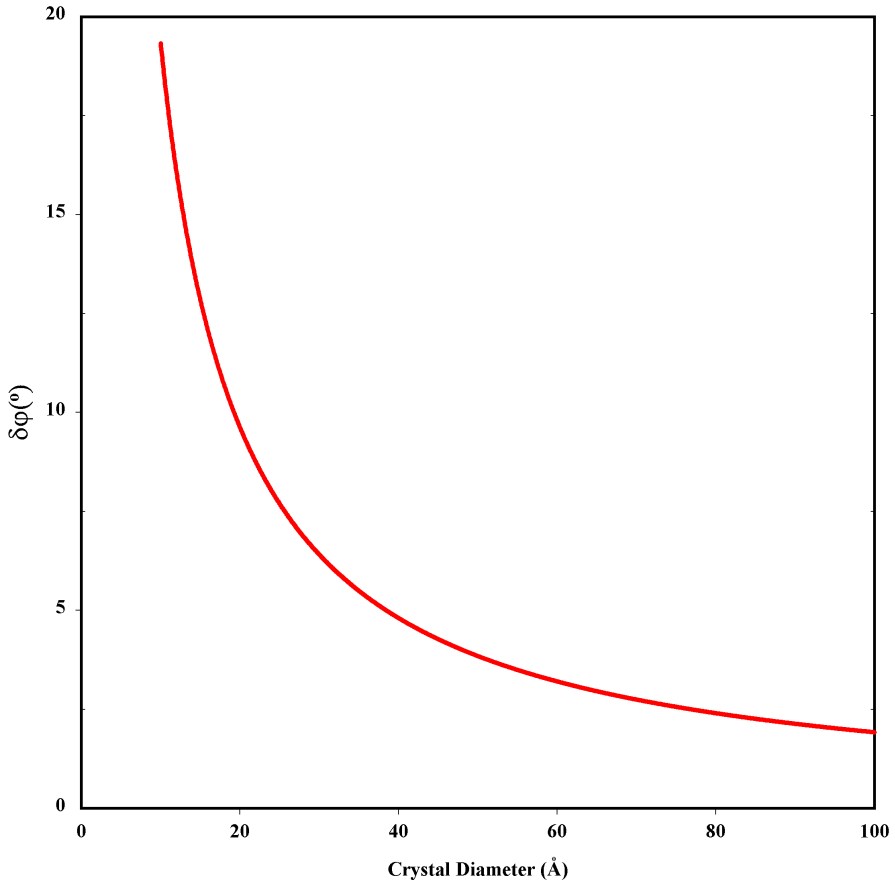

Figure 4-8. Uncertainty of the interplanar angle of the {200} cross-lattice fringes in HRTEM images of WC_{1-x} crystals as s function of crystal diameter. The source considered for such an uncertainty is the expansion of the reciprocal lattice spots along the azimuthal direction in the image plane.

between 2 and 3 times as large as the percent errors, and hence of the right order of magnitudes. A statistical study of lattice fringe spacing uncertainty with more data from 23 crystals, and a comparison of the study with the model prediction is given in 4.4.1.5.

Table 4-2. Uncertainties of some reciprocal lattice vectors and an interplanar angle of WC_{1-x} obtained from models, and some percent differences between their experimental counterparts and the literature values.

g	$(dg/g)_x$ (%)		$(dg/g)_z$ (%)		$(dj)_x$ (°)	
	Model	Experimental	Model	Experimental	Model	Experimental
$g_1=g_{200}$	1.75	0.5			1.92	0.8
$g_2=g_{020}$		1.4				
$g_3=g_{1,1,-1}$	2.00	1.2	7.48	2.4		

Notations used:
Model: Uncertainty predicted by a model
Experimental: experimental data

4.4.1.5 Observation: An Ensemble Study of Zone Images A recent paper on HRTEM image simulation indicated that orientation deviations of a 2.8 nm spherical palladium nanocrystal from a <110> zone axis may result in fringes unrelated to the structure of the particle (Malm, 1997). Variation in measured lattice spacings was reported to be as high as several percent, with the highest reaching 10%. To compare such results with our experimental data, 23 single crystals each of which is free of overlap with any other crystal, and showing cross-fringes, were examined. The projected sizes of these crystals range from 3.7 nm × 3.8 nm to 10.8 nm×7.8 nm. The spacings and angles between fringes are plotted in Figure 4-9.

The observed cross-fringes in the HRTEM images fall into two categories, according to their spacings and interplanar angles. The first is characterized by a 90° interplanar angle and two 2.12 Å lattice spacings. There are nine such crystals. The second one by two inter-planar angles of 55°, 70° and three lattice spacings, two of which are 2.12 Å, and the third, 2.44 Å. For fringes in the second category, only the spacings of 2.44 Å and 2.12 Å and the corresponding angle of 55° are plotted inFigure 4-9. Since the two categories of cross-fringes match those along the <001> and <011> zone axes of WC1-x, the only two zones which will show cross lattice-fringes in our HRTEM images, the thin film consists mainly of WC_{1-x}. This is consistent with the chemical composition analyses described in 2.7.3 (Qin, 1998).

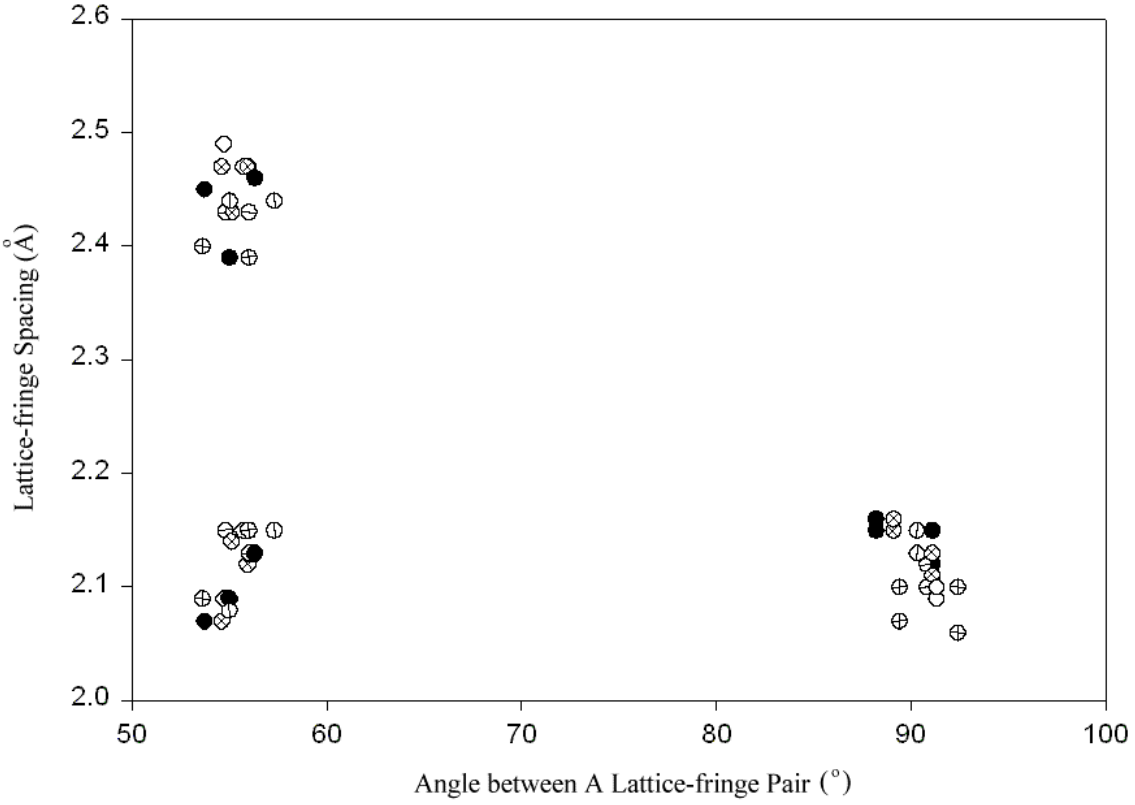

Figure 4-9. The spacings and interplanar angles measured from the cross lattice fringes of 23 WC_{1-x} nanocrystals, each of which is free of overlap with any other as observed in HRTEM images. Each crystal is plotted as a pair of spacings at the same interplanar angle. Each pair uses the same symbol. The specific combinations of lattice spacings and interplanar angles match the finger prints of the <001> and <011> zone images of WC_{1-x}, and hence indicate that WC_{1-x} is the only present phase in the film. The standard deviations from the means of lattice spacings and interplanar angles are less than 1.5% and 1.3°, respectively.

4.4.2. Discussion

4.4.2.1 Ensemble Study of Nanocrystals The above ensemble study is identical in principle with one of the data acquisition methods of electron tomography, which is through imaging different copies of an object occuring in different orientations, as discussed in 1.3.3.2. The other method, which is by imaging the same object in a series

of tilts, can also be extended in our stereo analysis of nanocrystals. This is described as follows.

Given a nanocrystal, its orientation can be randomized in the TEM, and HRTEM images are taken in this process. A large enough number of images at different crystal orientations can be used to perform another "ensemble study", from which the finger print of the crystal lattice can be identified.

4.4.2.2 Optimal Crystal Size Range for Stereo Lattice Imaging Equations (4-8), (4-9), and (4-10) indicate that the uncertainties of a reciprocal lattice vector and an inter-planar angle will increase as the crystal size gets small. While on the other hand, the ease with which to acquire lattice fringes goes up. Hence there exists an optimum crystal size range for applying stereo lattice imaging, for a certain type of crystals. In such an optimum size range, the probability to acquire the targeted reciprocal lattice vectors must be sufficiently high, while on the other hand the uncertainties of reciprocal lattice vectors and interplanar angles must be sufficiently low.

Such a crystal size range varies with the crystal type, but is very likely to be between 1 nm to 10 nm. For example, in studying WC_{1-x} crystals, in order for a g_{111} not to be confused with a g_{200}, the following relationship of

$$(d\, g_{111}/g_{111})_x < \frac{|\, g_{111} - g_{200}\,|}{g_{111}} = 13.4\% \qquad (4\text{-}11)$$

must be satisfied. From (4-8) it can be seen that this happens when the crystal diameter is greater than 1.25 nm, i.e., t >1.25 nm. In this size range, on the other hand, the probabilities of success in the two data acquisition steps in the protocol used in Chapter 2 decrease from about 0.05 and 1, respectively. As a result, the overall probability of success has a maximum value of about 0.05, which indicates the existence of a significant fraction of "correctly-oriented" crystals in a polycrystalline specimen as discussed in 4.3.2.1.

4.4.2.3 Comparison among Theory, Observation and Image Simulation We have also performed a comparison among the model prediction, our ensemble study of the WC_{1-x} nanocrystals, and an image simulation, concerning lattice fringe spacing uncertainty. This is to be presented as follows.

For the 23 nanocrystals, the standard deviations from the means of the fringe spacings and interplanar angles measured from the two types of zone images are both less than 1.5% and 1.3°, respectively. Both are smaller than those reported in the image simulation. The main cause of such a difference, we believe, is the crystal size difference in these two cases. Another more detailed statistical study supports this conclusion.

This study is based on the images of eight out of the nine <001> crystals (the ninth crystal is excluded since its size is the smallest and much smaller than the average). The average projection size for this subset of <001> crystals is 8.85 nm, and the standard deviation from the mean of lattice fringe spacing is 1.47%. This is consistent with the model predicted fringe spacing uncertainty (for WC_{1-x}) in the image plane of $(dd/d)_{200,\,x} = 1.96\%$. For the Pd nanocrystal studied in the image simulation, the model predicts a fringe spacing uncertainty of $(dd/d)_{111,\,x} = 6.36\%$ in the image plane, which is also consistent with the reported typical values of several percents in the image simulation, yet smaller than the largest of about ten percents. This slight difference may be due to the intersection of reciprocal lattice spots along more than one zone axis with the Ewald sphere, which is not taken into account in our model, and will be discussed shortly.

In the image simulation, it was reported that destroyed and severely bent fringes appeared along directions that are between 10° and 30° away from the [011] zone, as a result of the low-pass filtering of the microscope of the dense projection of the charge potential/(atomic positions). Such fringes have not been observed in our experiment. We consider that such a difference also originates from that of the crystal sizes in these two cases.

When the crystal is small enough, the reciprocal lattice spots are large ehough for the Ewald sphere to intersect reciprocal lattice spots along more than one zone axis, as the crystal orientation is far away from low-index zone axes. The above mentioned low-pass filtering of the microscope of the dense projection of the charge potential along

viewing directions that are far way from the [110] zone axis, involves the influence from more than one set of lattice planes. As a result, Moire fringes of these lattice planes, limited in resolution by the TEM, appear.

In contrast, the crystals in our ensemble study are larger. From our previous discussion of θ_t and Figure 4-3, the maximum deviation of a <001> zone from the electron beam is 1.91°, in order for a WC_{1-x} crystal with a diameter of t = 8.85 nm to show cross-fringes along the zone axis. With such a small deviation of a <001> zone axis from the electron beam, as well as reciprocal lattice spots that are smaller, chances for the Ewald sphere to intersect reciprocal lattice spots along more than one zone axes are low, and no severely bent or destroyed fringes are observed.

In summary, since the average crystal diameter of 8.85 nm in our ensemble study is larger than that of 2.8 nm for the Pd particle examined in the image simulation, a smaller uncertainty of lattice fringe spacing is to be expected, as is predicted by our model and has become true in our study. The above comparison among our experimental data, model prediction and the image simulation data is summarized in the following Table 4-3. We recommend that such fringe abundance analyses go hand in hand with stereo lattice studies of nanocrystal specimens, and that comparative image simulation studies be done where possible as well.

Table 4-3. A summary of comparisons concerning lattice fringe spacing uncertainty in the image plane, maximum half angle between zone axis and the electron beam, among data from our experiment, model and the image simulation performed by J. O. Malm and M. A. O'keefe.

Case		Our Experiment	Image Simulation
Crystal		WC_{1-x}	Pd
Zone		<001>	<011>
Crystal diameter (Å)		88.5	28
Imaged Spacing (Å)		d_{002} = 2.124	d_{111} = 2.246
$(\delta g/g)_x$ (%)	Measured	1.47	7.75 (Fig.7. w=70°, α=15°)
	Model	1.96	6.36
θ_t (°)	Model	1.91	N/A

4.5. CONCLUSION

In this paper models to quantify the probabilities of success and the uncertainties of both reciprocal lattice vectors and interplananr angles in stereo lattice imaging have been presented. We have been able to determine the radius of a reciprocal lattice spot of a AuPd nanocrystal is about 0.8/(average crystal dimension). This is used to quantify the probabilities of success in the two data acquisition steps in the protocol used in Chapter 2, for a randomly oriented spherical nanocrystal with a cubic lattice and a diameter of 10 nm. It is found that the probability for such a nanocrystal to show cross-fringes along a <001> zone is on the order of a thousandth, and that to reveal the (1, 1, -1) lattice fringes along the [112] zone after tilting the same <001> crystal which is azimuthally random is about one-third. The overall probability of success is predominantly determined by that of the first data acquisition step. In addition, a sufficient tilt range (±36.0° for cubic crystals) as well as azimuthal rotation (90° for most first zones) will increase the probability to acquire the third set of lattice fringes to one, and hence the overall probability of success by a factor of about 3.

The major cause of the reciprocal lattice vector and interplanar angle uncertainties in the image plane is the expansion of the reciprocal lattice spot in the same plane. In the crystal diameter range of 2 nm to 10 nm, such an uncertainty is on the order of 1%. Reciprocal lattice vector uncertainties along the electron beam direction are about four times as high, and can be reduced through observing reciprocal lattice vectors farther out of the specimen plane. The interplanar angle uncertainty is on the order of 1° in the crystal diameter range of 2 nm to 10 nm for cross lattice-fringes with a typical spacing of 2 Å. As crystal diameter decreases, both the probability of success and the uncertainties of lattice fringe spacings and interplanar angles become higher. Generally there exists an "optimal" crystal diameter, with a balance between higher chances to visualize lattice fringes, and higher uncertainties in lattice fringe spacings as well as interplanar angles, for a certain type of material. For tungsten carbide nanocrystalline materials used in the experiment, the optimal crystal diameter is between 1.25 nm and 10 nm.

An ensemble study of zone images in the tungsten carbide nanocrystalline specimen shows the finger prints of the WC_{1-x} crystal lattice. This study, our model prediction and an image simulation (Malm, 1997) concerning lattice fringe spacing uncertainty all indicate that a larger crystal size reduces the uncertainty. As the crystal gets smaller, the Ewald sphere may intersect reciprocal lattice spots along more than one zone axis, and Moire fringes of the corresponding lattice planes will appear.

5. CONCLUSION

In this thesis three fundamental topics of direct space nanocrystallography in 3D via HRTEM were individually discussed. The development and application of an analytical technique to determine the lattice parameters of a nanocrystal from lattice images taken at two crystal orientations were described in Chapter 2. It is found that for a crystal lattice there are typically a very limited number of data acquisition protocols that serve to resolve the lattice structure in 3D, and hence such protocols can be enumerated. Some example protocols are given for face-centered cubic (f.c.c.), body-centered cubic (b.c.c.) and simple cubic (s.c.) lattices. The lattice parameters of a 10 nm f.c.c. WC_{1-x} crystal are determined using one of the protocols.

In Chapter 3, lattice fringe visibility after tilting is investigated based on the study of crystal diffraction geometry. With a semi-empirical model, the probability for each of the 17 lattice fringe sets to become invisible after tilting is quantified. We have introduced two new concepts, which are the visibility band and visibility band map. The visibility band map of a nanocrystal can be used to guide direct space crystallographic analyses, and thus can be regarded as the counterpart of a Kikuchi map in direct space. The abundance of any set of lattice fringes and any zone images can also be quantified from the map.

In Chapter 4, models to calculate the probability of success and the uncertainties of reciprocal lattice vectors in applying the stereo analysis technique described in Chapter 2 are presented. The size of a {002} reciprocal lattice spot of the AuPd/C nano-particles was determined to be ~0.79/(crystal diameter), and this relationship is assumed for the {111} and {002} reciprocal lattice spots of WC_{1-x} nanocrystals. Based on this relationship, both the probability of success and uncertainties of reciprocal lattice vectors are quantified. It is found that with a side-entry tilt of ±35.3° or more, and a “tilt-rotate” specimen holder, the overall probability of success can be increased by a factor of about three. For a certain type of crystal, there is an optimum crystal size range to apply the technique. In such a size range, an adequately high probability of success and low enough uncertainties of reciprocal lattice vectors coexist.

With modern computer support, visibility band maps discussed in Chapter 3 can be generated and routinely used as the “roadmaps” to guide crystallographic analysis of nanocrystals in direct space, just like Kikuchi band maps have been used in reciprocal space crystallography. When lattice fringes are visible, they can be matched with the visibility bands in the visibility band maps, and the crystal orientation can be determined. This could help computer software to output, and users to recognize, tilt directions of interest for further crystallographic analyses, which may include crystal lattice determination and zone axis imaging.

Other subjects of the thesis also open some possibilities for computer supported direct space crystallography. For example, in Chapter 4 ensemble studies of randomly oriented WC_{1-x} crystals were discussed. These suggest that such fingerprinting of fringe abundances from randomly-oriented crystals can be useful with no tilting at all, and further that computer-guided exploration of fringes as a function of orientation could be used to better identify individual crystals, and constrain both the abundance of phases and their orientation preferences, using images alone! For example, if the computer were simply used to randomize the orientations of a single nanocrystal, the images taken might reveal the fingerprint of the crystal lattice, just as discussed in Chapter 4.

APPENDIX A.

Derivation of An Equation in Chapter 2

DERIVATION OF (2-7): AZIMUTH OF EFFECTIVE TILT AXIS

Let φ_{eff} denote the azimuth of the effective tilt axis in a double tilt, and (θ_1, θ_2) and (θ_1', θ_2'), the beginning and final specimen orientations, respectively. Assume a reciprocal lattice vector **g**, as expressed in our coordinate system specified in 2.3.3 when the specimen is untilted, is parallel to the effective tilt axis.

The reciprocal lattice vector **g** will thus be in Bragg condition in both specimen orientations, and in addition, will have the same micrograph coordinates $\mathbf{g}_m$ in these two specimen orientations. From (2-3) the following relation of

$$A(\theta_1, \theta_2)\mathbf{g}_m = \mathbf{g} = A(\theta_1', \theta_2')\mathbf{g}_m, \text{ where} \quad \text{(A-1)}$$

$$g_{mx} = g\cos(\varphi_{eff}),$$

$$g_{my} = g\sin(\varphi_{eff}), \text{ and}$$

$$g_{mz} = 0 \quad \text{(A-2)}$$

can be obtained. Expanding (A-1) gives the following three equations of

$$g_{mx}\cos(\theta_1) = g_{mx}\cos(\theta_1'), \quad \text{(A-3)}$$

$$-g_{mx}\sin(\theta_2)\sin(\theta_1)+g_{my}\cos(\theta_2) = -g_{mx}\sin(\theta_2')\sin(\theta_1')+g_{my}\cos(\theta_2'), \text{ and} \quad \text{(A-4)}$$

$$-g_{mx}\cos(\theta_2)\sin(\theta_1)-g_{my}\sin(\theta_2) = -g_{mx}\cos(\theta_2')\sin(\theta_1')-g_{my}\sin(\theta_2'). \quad \text{(A-5)}$$

From (A-3) and(A-4), it can be obtained that the following relationship of

$$\theta_1' = -\theta_1, \text{ and}$$

$$\theta_2' = -\theta_2 \quad \text{(A-6)}$$

is valid. Putting (A-6) into (A-5), the following equation of

$$-g_{mx}\cos(\theta_2)\sin(\theta_1)-g_{my}\sin(\theta_2) = g_{mx}\cos(\theta_2)\sin(\theta_1)+g_{my}\sin(\theta_2)$$

is obtained, which can be reduced to

$$-2g_{mx}\cos(\theta_2)\sin(\theta_1) = 2g_{my}\sin(\theta_2). \quad \text{(A-7)}$$

From (A-2) and (A-7), it can be obtained that the following relaiton of

$$g_{my} / g_{mx} = \tan(\varphi_{eff}) = -\cos(\theta_2)\sin(\theta_1)/\sin(\theta_2) \quad \text{(A-8)}$$

is true, and finally (A-8) gives the solution of

$$\varphi_{eff} = \tan^{-1}[-\cos(\theta_2)\sin(\theta_1)/\sin(\theta_2)]. \quad \text{(A-9)}$$

APPENDIX B.

Derivations of Some Equations in Chapter 3

B1. DERIVATION OF (3-1): MAXIMUM TRANSVERSE TILT

The following equation can be obtained from Figure 3-6,

$$\cos \angle ABC = \frac{AB^2 + BC^2 - AC^2}{2 \cdot AB \cdot BC}. \tag{B-1}$$

Through substitution, equation (B-1) changes to

$$\cos\left(\frac{p}{2} - a_{\max}\right) = \frac{\left(\frac{1}{l}\right)^2 + \left(\frac{1}{d}\right)^2 - \left(\frac{1}{l} - \frac{f}{t}\right)^2}{2 \cdot \frac{1}{l} \cdot \frac{1}{d}}. \tag{B-2}$$

Equation (B-2) is then reduced to

$$\sin a_{\max} = \frac{\frac{1}{d^2} + \frac{2f}{lt} - \frac{f^2}{t^2}}{\frac{2}{ld}} = \frac{ld}{2}\frac{2f}{lt} + \frac{ld}{2}\left(\frac{1}{d^2} - \frac{f^2}{t^2}\right) = \frac{df}{t} + \frac{ld}{2}\left(\frac{1}{d^2} - \frac{f^2}{t^2}\right). \tag{B-3}$$

Taking arcsine on both sides of (B-3) leads to (3-1).

B2. DERIVATION OF (3-2)

The following equation can be obtained from Figure 3-7,

$$AC = \frac{1}{l} + \frac{f}{t}. \tag{B-4}$$

In the right triangle DABC, the following equation can be obtained,

$$\left(\frac{1}{l}\right)^2 + \left(\frac{1}{d}\right)^2 - \left(\frac{1}{l} + \frac{f}{t}\right)^2 = \frac{1}{d^2} - \frac{f^2}{t^2} - \frac{2f}{lt} = 0. \tag{B-5}$$

Letting f / t = x, equation (B-5) can be put in the form of

$$\frac{1}{d^2} - \frac{2x}{l} - x^2 = \frac{1}{d^2} - \left(x + \frac{1}{l}\right)^2 + \frac{1}{l^2} = 0. \tag{B-6}$$

The solution of (B-6) is

$$x = \frac{f}{t_0} = \sqrt{\frac{1}{d^2} + \frac{1}{l^2}} - \frac{1}{l} = \frac{1}{dl}\left(\sqrt{d^2 + l^2} - d\right).$$

Therefore the minimum crystal diameter is obtained as

$$t_0 = \frac{fdl}{\sqrt{d^2 + l^2} - d}.$$

B3. DERIVATION OF (3-3): MINIMUM TRANSVERSE TILT

In Figure 3-9(b), the relationship as given in (B-4) is still true. From the triangle DABC, the equation

$$\cos\angle ABC = \frac{\left(\frac{1}{l}\right)^2 + \left(\frac{1}{d}\right)^2 - \left(\frac{1}{l} + \frac{f}{t}\right)^2}{2 \cdot \frac{1}{l} \cdot \frac{1}{d}} = \frac{\left(\frac{1}{d^2} - \frac{f^2}{t^2} - \frac{2f}{lt}\right) l d^2 t^2}{\frac{2}{ld} \cdot l d^2 t^2} = \frac{l t^2 - l f^2 d^2 - 2 f t d^2}{2 d t^2}$$

follows. Therefore it is true that

$$\angle EBC = a_{\min} = \frac{p}{2} - \angle ABC = \frac{p}{2} - \cos^{-1}\left(\frac{l t^2 - l f^2 d^2 - 2 f t d^2}{2 d t^2}\right).$$

APPENDIX C.

Derivations of Some Equations in Chapter 4

C1. DERIVATIONS OF (4-1), (4-2) AND (4-3)

C1.1 DERIVATION OF (4-1): THE PROBABILITY p_x

The relaxation of Bragg condition in getting the <001> zone cross lattice-fringes defines a maximum half angle θ_t between the electron beam and the zone axis. In Figure C. 1 and Figure C. 2, A is the center of the Ewald sphere, O is the origin of the reciprocal lattice, $AO = g_\lambda = 1/\lambda$ is equal to the radius of the Ewald sphere, and D is the projection of A on the horizontal image plane. Segment OZ is parallel to the <001> zone. Segments OB and OC are two basic reciporcal lattice vectors (linearly independent of each other) along the <001> zone. Their magnitudes are $OB = OC = g = 1/d$, where $d > r_{Sch}$ is the corresponding lattice spacing. Also $g_t = f / t$ is the radius of the reciprocal lattice spots centered at B and C (which we will refer to as "reciprocal lattice spots B and C"), where t is the diameter of the crystal, and f is the visibility factor discussed in Chapter 3.

Each of the two figures shows a critical configuration under which the Ewald sphere is tangent with the reciprocal lattice spots B and C simultaneously. Such a tangent is from the outside of the Ewald sphere in Figure C. 1, and from the inside in Figure C. 2. Denote the point in segment AC at which the Ewald sphere and the reciprocal lattice spot C are tangent as E, and that in the segment AB as F. Therefore it is true that $AB = AC = AE + EC = g_\lambda + g_t$ in Figure C. 1, and $AB = AC = AE - CE = g_\lambda - g_t$ in Figure C. 2.

Corresponding to each of these two critical conditions, a maximum deviation angle θ_t, which is equal to $\angle AOZ$ in the figures, of the <001> zone from the electron beam for visualizing the cross lattice-fringes thus exists. As an approximation, assume there is a rotational symmetry of OZ about AO. This subsequently defines a solid angle whose magnitude is proportional to the probability of getting cross lattice fringes from HRTEM images of the crystal.

In Figure C. 1, it is true that $\angle COD = 135°$. Denote OD as x, i.e., $OD = x$. In

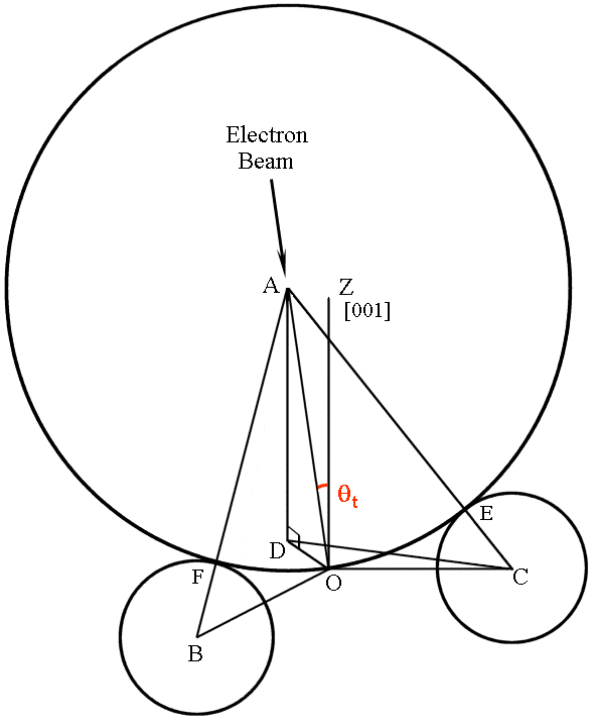

Figure C. 1. Schematic illustrating the geometry among the reciprocal lattice spots and the Ewald sphere in quantifying the probability of getting cross lattice-fringes along a <001> zone of a randomly-oriented spherical cubic crystal. The figure shows a critical configuration in which the Ewald sphere is tangent with two reciprocal lattice spots along the <001> zone simultaneously from the outside. In the figure, A is the center of the Ewald sphere. O is the origin of the reciprocal lattice. AO = $g_\lambda = 1/\lambda$ is equal to the radius of the Ewald sphere. D is the projection of A on the horizontal image plane. OZ is parallel to the <001> zone. OB and OC are two basic reciprocal lattice vectors (linearly independent of each other) along the <001> zone, and OB = OC = g = 1/d are their magnitudes where d > r_{Sch} is the corresponding lattice spacing. g_t = f / t is the radius of the reciprocal lattice spots centered at B and C, where t is the diameter of the crystal, and f is the visibility factor discussed in Chapter 3. The Ewald sphere is tangent with reciprocal lattice spots B and C at points E and F, respectively. Therefore it is true that AB = AF + FB = AC = AE + EC = g_λ + g. The angle $\theta_t = \angle AOZ$ is a maximum half angle between the electron beam and the zone axis. By assuming a rotational symmetry of OZ about OA, the corresponding solid angle is proportional to the probability of getting cross lattice fringes along a <001> zone.

triangle ΔDOC, it can be obtained that

$$DC^2 = OD^2 + OC^2 - 2OD \cdot OC \cdot \cos\angle COD = x^2 + g^2 + \sqrt{2}xg \ .$$

In the right triangle ΔADO, it can be obtained that

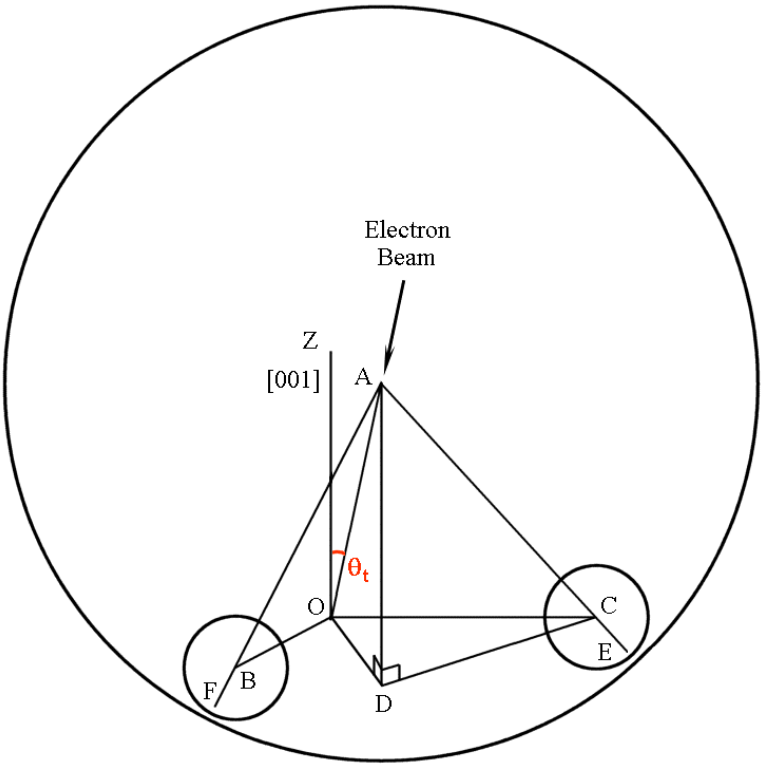

Figure C. 2. Schematic illustrating the geometry among the reciprocal lattice spots and the Ewald sphere in quantifying the probability of getting cross lattice-fringes along a <001> zone of a randomly-oriented spherical cubic crystal. The figure shows a critical configuration in which the Ewald sphere is tangent with two reciprocal lattice spots along the <001> zone simultaneously from the inside. In the figure, A is the center of the Ewald sphere. O is the origin of the reciprocal lattice. AO = $g_\lambda = 1/\lambda$ is the radius of the Ewald sphere. D is the projection of A on the horizontal image plane. OZ is parallel to the <001> zone. OB and OC are two basic reciprocal lattice vectors (linearly independent of each other) along the <001> zone. OB = OC = g = 1/d where d > r_{Sch} is the corresponding lattice spacing. $g_t = f / t$ is the radii of the reciprocal lattice spots centered at B and C, where t is the diameter of the crystal, and f is a parameter for adjusting the radii of the reciprocal lattice spots B and C whose intersection with the Ewald sphere results in detectable lattice fringes in HRTEM images. The Ewald sphere is tangent with reciprocal lattice spots B and C at points E and F, respectively. Therefore AF = AE = g_λ, AB = AC = g_λ - g. The relaxation of Bragg condition in getting the <001> zone cross lattice fringes defines a maximum half angle $\theta_t = \angle AOZ$ between the electron beam and the zone axis. By assuming a rotational symmetry of OZ about OA, the corresponding solid angle is proportional to the probability of getting cross lattice fringes along a <001> zone.

$$AD^2 = AO^2 - OD^2 = g_l^2 - x^2 .$$

Since AC is the hypotenuse of the right triangle ΔADC, it can be obtained that

$$AC^2 = (g_l + g_t)^2 = AD^2 + DC^2 = g_l^2 - x^2 + x^2 + g^2 + \sqrt{2}xg ,$$

which is reduced to

$$g_l^2 + g_t^2 + 2g_l g_t = g_l^2 + g^2 + \sqrt{2}xg\ .$$

Hence x can be obtained as

$$x = \frac{g_t^2 - g^2 + 2g_l g_t}{\sqrt{2}g}\ .$$

∠AOZ can be obtained from ΔADO as

$$\angle AOZ = q_t = \angle OAD = \sin^{-1}\frac{OD}{AO} = \sin^{-1}\frac{x}{g_l} = \sin^{-1}\frac{g_t^2 - g^2 + 2g_l g_t}{\sqrt{2}\cdot g\cdot g_l}\ . \qquad \text{(C-1)}$$

In Figure C. 2, it is true that ∠COD = 45°. Denote OD as x, i.e., OD = x. In triangle ΔDOC, it can be obtained that

$$DC^2 = OD^2 + OC^2 - 2\cdot OD\cdot OC\cdot\cos\angle COD = x^2 + g^2 - \sqrt{2}xg\ .$$

In the right triangle ΔADO, it can be obtained that

$$AD^2 = AO^2 - OD^2 = g_l^2 - x^2\ .$$

Since AC is the hypotenuse of the right triangle ΔADC, it can be obtained that

$$AC^2 = (g_l - g_t)^2 = AD^2 + DC^2 = g_l^2 - x^2 + x^2 + g^2 - \sqrt{2}xg\ ,$$

which is reduced to

$$g_l^2 + g_t^2 - 2g_l g_t = g_l^2 + g^2 - \sqrt{2}xg\ .$$

Hence x can be obtained as

$$x = \frac{g^2 - g_t^2 + 2g_l g_t}{\sqrt{2}g}\ .$$

∠AOZ can be obtained from ΔADO as

$$\angle AOZ = q_t = \sin^{-1}\frac{OD}{AO} = \sin^{-1}\frac{x}{g_l} = \sin^{-1}\frac{g^2 - g_t^2 + 2g_l g_t}{\sqrt{2}\cdot g\cdot g_l}\ . \qquad \text{(C-2)}$$

For d < t, θ_t in (C-2) is greater than that in (C-1) (Given d = 2 Å, such a difference is about 0.8° for t > 5 Å, the difference is on the order of thousandth of a degree). θ_t in

(C-2) is going to be used to evaluate p_x. The solid angle with a half-angle equal to $\angle AOZ = \theta_t$ is

$$s = 2p\left(1-\cos q_t\right). \tag{C-3}$$

Given a multiplicity of n of the <001> zone, the probability p_x is equal to

$$p_x(t,d,f) = \frac{n \cdot s}{4p} = \frac{n}{2}(1-\cos q_t). \tag{C-4}$$

For cubic lattices, n = 6. (C-4) is reduced to

$$p_x(t,d,f) = 3(1-\cos q_t).$$

C1.2. DERIVATION OF (4-2): MAXIMUM PERCENT DIFFERENCE BETWEEN LATTICE FRINGE SPACING AND LATTICE SPACING

In Figure C. 2, when the reciprocal lattice spots B and C are tangent with the Ewald sphere from the inside, generally (for t < 16 nm and d = 2 Å, which will be seen in the following discussion) the lattice fringe vector is shorter than the corresponding reciprocal lattice vector, i.e., the following relationship of g' = OE < g = OC = OB is true, or equally stated, the lattice fringe spacing d' is longer than the lattice spacing d, i.e., d' > d. This relationship can be seen more easily from Figure C. 3. Due to such a difference, corresponding to a crystal diameter t, therefore there exists a maximum percent difference of δ for the lattice fringe spacing. Equally stated, for an upper limit of percent difference δ of the lattice fringe spacing d', there exists a lower limit of crystal size t_{min}. Below t_{min}, the maximum percent difference is greater than δ. δ is defined through the following equation of

$$d' = (1+d)d,$$

which can be rewritten as

$$g' = \frac{1}{1+d}g.$$

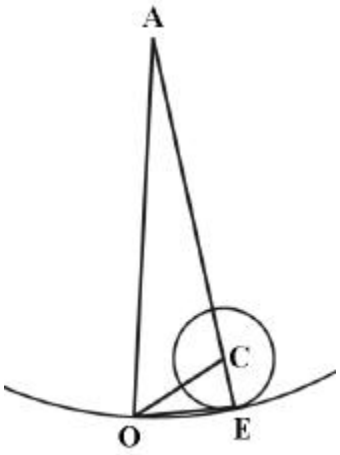

Figure C. 3. Schematic illustrating the geometry between a reciprocal lattice spot and the Ewald sphere in quantifying the maximum percent error of the lattice fringe spacing. What is shown here is the plane containing ∆AOE in Figure C. 1.. The reciprocal lattice spot centered at C is tangent with the Ewald sphere from the inside at E. A is the center of the Ewald sphere. O is the origin of the reciprocal lattice. The lattice fringe vector is OE.

In Figure C. 3, since ΔAOE is an isosceles triangle, the following equation of

$$\sin\frac{\angle OAE}{2}=\frac{\frac{OE}{2}}{OA}=\frac{\frac{g'}{2}}{g_l}=\frac{g'}{2g_l} \tag{C-5}$$

can be obtained. In ΔCOE, the following equation of

$$OC^2=EO^2+EC^2-2\cdot EO\cdot EC\cdot\cos\angle OEC$$

can be obtained. After substitution, this equation is changed to

$$g^2=g'^2+g_t^2-2g'\cdot g_t\cdot\cos(\frac{p-\angle OAE}{2})=g'^2+g_t^2-2g'\cdot g_t\cdot\sin\frac{\angle OAE}{2}.$$

Through using equation (C-5), the above equation is changed to

$$g^2=g'^2+g_t^2-2g'\cdot g_t\cdot\frac{g'}{2g_l}=g'^2+g_t^2-\frac{g'^2\,g_t}{g_l}=g'^2(1-\frac{g_t}{g_l})+g_t^2.$$

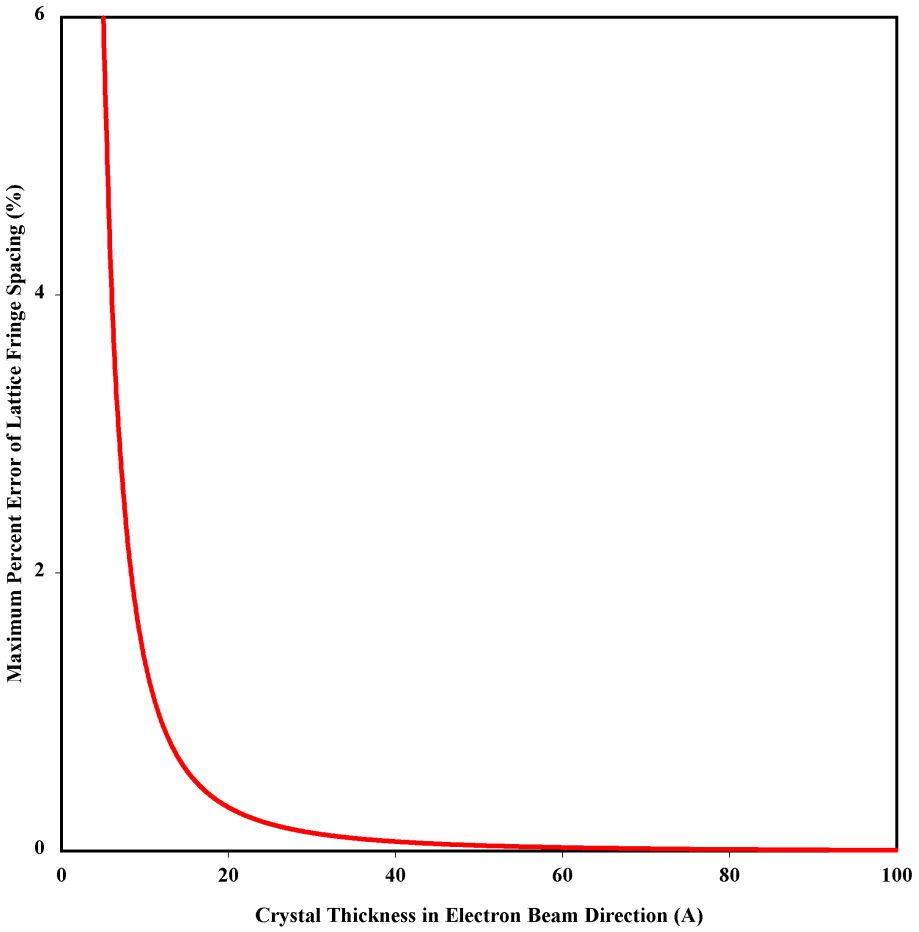

Figure C. 4. The maximum percent error of a lattice fringe spacing for a spherical WC_{1-x} crystal showing <001> cross fringes. The curve corresponds to the critical crystal orientation in which the two basic reciprocal lattice spots along the <001> zone axis are tangent with the Ewald sphere from the inside.

g' can thus be obtained as

$$g' = \frac{g}{1+d} = \sqrt{\frac{g^2 - g_t^2}{1 - \frac{g_t}{g_l}}} \,. \qquad \text{(C-6)}$$

$t_{min}(\delta)$ can be determined from (C-6). Figure C. 4 show a plot of $\delta(t)$ for WC_{1-x}.

As mentioned in the beginning of this section, when t < 16 nm, it is true that g' < g for d = 2 Å. This can be inferred by first assuming that the relation of g' < g, then from (C-6), the following inequality of

$$\frac{g'}{g} = \sqrt{\frac{1-\left(\frac{g_t}{g}\right)^2}{1-\frac{g_t}{g_l}}} < 1$$

can be obtained. This can be sequentially changed to the following forms of

$$1-\left(\frac{g_t}{g}\right)^2 < 1-\frac{g_t}{g_l}, \text{ and}$$

$$\frac{g_t}{g_l} < \left(\frac{g_t}{g}\right)^2, \text{ and}$$

$$\frac{1}{g_l} < \frac{g_t}{g^2}, \text{ and}$$

$$l < \frac{fd^2}{t}.$$

Finally the follwing inequality of

$$t < \frac{fd^2}{l} \qquad \text{(C-7)}$$

can be obtained.

For f = 0.79, d = 2 Å, λ = 0.0197 Å, the right side of (C-7) gives 160 Å. Therefore the relationship of g' > g only becomes true in the crystal diamtere range of t > 160 Å. Yet as the crystal size increases, the reciprocal lattice spot size decreases, the percent error of lattice fringe spacing d' is reduced. As a result, δ becomes very small (<0.005%). Compared with the typical uncertainty of about 1-2% of the lattice fringe spacings due to the reciprocal broadening effect of nanocrystals in HRTEM images, such a difference is negligible, and it becomes true that d' ≅ d. As a conclusion, d' will become shorter than d only for large crystals, yet such a difference will be negligibly small.

C1.3. DERIVATION OF (4-3): CRYSTAL SIZE RANGE OF VALIDITY IN QUANTIFYING p_x

As pointed out above, once a <001> zone falls into the solid angle s, the Ewald sphere intersects two adjacent reciprocal lattice spots out of the four along the <001> zone simultaneously. When a <001> zone is parallel to the electron beam, such intersection must remain valid. This imposes a lower limit of the size of the four reciprocal lattice spots, which in turn determines an upper limit of crystal size. Since such an intersection will be from the outside of the Ewald sphere, Figure C. 1 will be used in the following discussion. Under this condition, the following relationship of OA // OZ and AO⊥OC becomes true. In the right triangle ΔAOC, the following equation of

$$AC^2 = AO^2 + OC^2$$

can be obtained. After substitution, it changes to the following equation of

$$(g_l + g_t)^2 = g_l^2 + g^2,$$

which can be changed to the following equation of

$$g^2 - g_t^2 - 2g_l g_t = 0,$$

and further to the following equation of

$$\frac{}{d} - \frac{f^2}{t} - \frac{f}{lt} = 0.$$

Multiplying both sides by $\lambda d^2 t^2$ gives the following equations of

$$0 = \quad - \quad -2 \quad = \left(\quad - \frac{2fd}{l} \quad - \quad \right) = \left[\left(\quad - \frac{fd}{l} \right)^2 - \frac{f \ d}{l^2} - \quad \right].$$

The maximum crystal diameter can be obtained as

$$_{max} = \frac{}{l} + \sqrt{\frac{}{l^2} + \quad ^2 \ ^2} = \frac{}{l} + \quad \sqrt{\frac{}{l^2} + 1}.$$

For d = 2 Å, and f = 0.79 for Au/Pd particles sputtered on a thin carbo film determined in our experiment, t_{max} = 320 Å. For d = 2.124 Å, and f = 0.79 for WC_{1-x} particles, t_{max} = 361 Å. The crystals studied in these two samples are all smaller than these two upper limits, respectively.

C2. DERIVATIONS OF (4-4), (4-5), and (4-6)

C2.1. DERIVATION OF (4-4): PROBABILITY p_3 OF {111} FRINGES AFTER 35.26° RANDOM TILT FROM CUBIC <001> CRYSTAL

Such a crystal has a <001> zone parallel to the electron beam/optical axis. Denote the (1, 1, -1) reciprocal lattice point as C, and (000) as O, as shown in Figure C. 5.

In this figure, OC is $\theta = 35.26^o$ below the image plane in the reciprocal space. B is the projection of C on the image plane. A is the projection of B on T, i.e., BA$\perp$T**,** where T is the tilt axis. When the (2, -2, 0) reciprocal lattice vector deviates from being parallel to T by φ, the projection of the (1, 1, -1) reciprocal lattice point on the image plane, B, deviates from being perpendicular to T by φ as well, i.e., $\angle OBA = \varphi$. This is illustrated in Figure C. 6. With such an angular deviation of φ, the (1, 1, -1) reciprocal lattice spot will become tangent with the Ewald sphere after tilt, as shown in Figure C. 7, where the (1, 1, -1) reciprocal lattice spot is denoted as C_0 in its new position after tilt, and the tangent point is denoted as E. In addition, D denotes the center of the Ewald sphere. DO and DE are both equal to the raius of the Ewald sphere, i.e., DO=DE = g_λ. EC_0 is equal to the radius of the (1, 1, -1) reciprocal lattice spot, i.e., $EC_0 = g_t = f / t$. B' is the projection of C_0 on the image plane.

In Figure C. 5, from the right triangles ΔOAB and ΔABC, the following equations of

$$AB = OB \cos \angle OBA = OB \cos\varphi,$$

and

$$BC = OB \tan\theta,$$

respectively, can be obtained. Denote $\angle$CAB as α, i.e., $\angle CAB = \alpha$. From the above two equations, α can be obtained as

$$\alpha = \tan^{-1}(BC/BA) = \tan^{-1}(\tan\theta/\cos\varphi). \qquad \text{(C-8)}$$

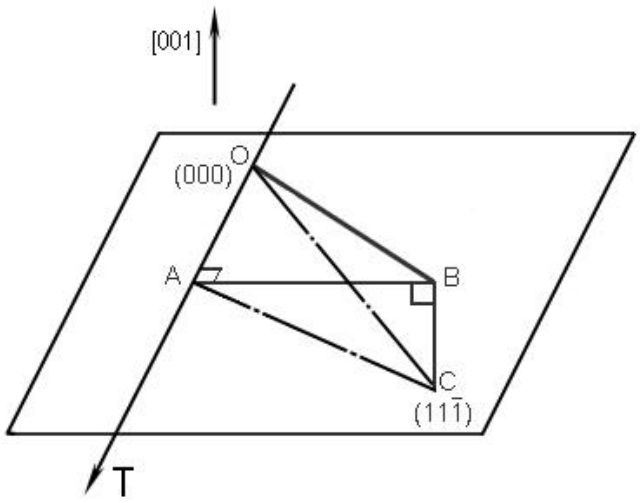

5. Schemat

-1) lattice fringes after tilting an azimuthally random spherical <001> cubic crystal by 35.3°
crystal has the <001> zone parallel to the electron beam/optical axis. C denotes the (1, 1, 1) reciprocal
lattice point, and O, (000). OC is = 35.26°
projection of C on the image plane. A is the projection of B on T, i.e., BA⊥ , where is the tilt axis.
-2, 0) reciprocal lattice vector deviates from being parallel to by , the projection of the (1,
1, 1) reciprocal lattice point on the image plane, B, deviates from being perpendicular to T φ as well,
∠OBA = . This is illustrated in Figure C6. With such an angular deviation , the (1, 1, -
lattice spot will be tangent with the Ewald sphere after tilt, as shown in Figure C. , where the (1, 1, -
reciprocal lattice spot is denoted as C in the new position.

(C 8) α θ -

zero deviation angle , i.e., φ ≠ 0, the amount

(1, 1, - ∠BAC = , is greater than θ

see that after tilting about T θ = 35.26 , AC_0 α θ

T. AC can at most be on the image plane after tilt, which happens when = 0. As

discussed previously, is so defined that the (1, 1, -

tangent with the Ewald sphere at point E after tilt, as shown in Figure C. . This implies

the existence of a lower limit of the size of the (1, 1, 1) reciprocal lattice spot, which

ultimately determines an upper limit of the crystal size. All crystals in our discussion

erwise the intersection of the (1, 1, -

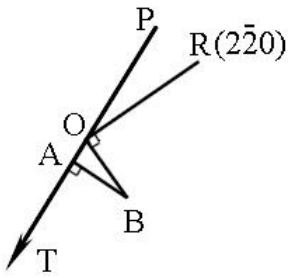

6. Schematic illustrating the geometry between the projections of the (1, 1, 1), (2, -
reciprocal lattice vectors and the tilt axis on the image plane. O is the origin of the reciprocal lattice. B is
-1). (2, 2, 0) is on the image plane and denoted as R. OR deviates from the tilt axis
by . From the relation of ∠ ∠OBA, the projection of (1, 1, 1) on the image plane, OB, deviates
fro φ.

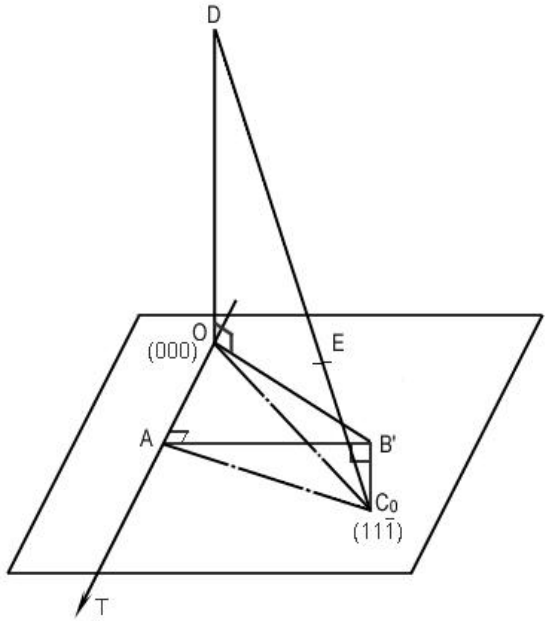

Figure C. . Schematic illustrating the geometry after the crystal in Figure C. . is tilted. D is the center of
the λ, where g is the radius of the Ewald sphere, EC_0 t is the radius of the
-1) reciprocal lattice spot. The reciprocal lattice point (1, 1, 1) has been rotated from C to C_0
subscript 0 denotes the critical condition. The (1, 1, 1) reciprocal lattice spot is tangent with the Ewald
sphere at E. For a certain size of the (1, 1, 1) reciprocal lattice spot, there exists a maximum azimuthal
deviation, i.e., , of the (2, - lt axis. Within φ -1)

proportional to the probability of getting the (1, 1, -
crystal with a random azimuth.

reciprocal lattice spot with the Ewald sphere can never happen after the tilt of 35.3°. This size limit is going to be inferred in C2.3. The following discussion is based on the assumption that the crystal size is below such a limit.

In Figure C. 5, from the right triangles ΔOBC and ΔOAB, the following equations of

$$OB = OC\cos\theta = g\cos\theta,$$

and

$$OA = OB\sin\varphi = g\cos\theta\sin\varphi, \qquad \text{(C-9)}$$

respectively, can be obtained. OA remains unchanged after tilt, and the reciprocal lattice point (1, 1, -1) remains in the plane perpendicular to T and containing A throughout the tilt, as shown in Figure C. 7.

From Figure C. 7, an equality of $\angle C_0AB' = \alpha -$ can be obtained. Denote the angle C_0AB' as *w*, that of $\angle C_0OB'$ as β $\angle DOC$ as γ ΔDOC, the following equation of

$$\cos\angle DOC_0 = \cos g = \frac{OD^2 + OC_0^2 - DC_o^2}{2\cdot OD\cdot OC_0} = \frac{g_l^2 + g^2 - (g_l + g_t)^2}{2\cdot g_l\cdot g}$$

can be obtained, which is simplified as

$$\cos g = \frac{g^2 - g_t^2 - 2g_l g_t}{2\cdot g_l\cdot g}. \qquad \text{(C-10)}$$

From the right triangle of $\Delta OB'C_0$, the following two equations of

$$OB' = OC_0\cos\angle C_0OB' = g\cos\beta, \qquad \text{(C-11)}$$

and

$$C_0B' = OC_0\sin\angle C_0OB' = g\sin\beta \qquad \text{(C-12)}$$

can be obtained. Using (C-11) and (C-9) (since OA remains unchanged throughout the tilt as discussed), one side of the right triangle ΔOAB' can be expressed as

$$AB' = \sqrt{OB'^2 - OA^2} = \sqrt{(g\cdot\cos b)^2 - (g\cdot\cos q\sin j)^2} = g\sqrt{(\cos b)^2 - (\cos q\sin j)^2}. \qquad \text{(C-13)}$$

Using (C-12) and (C-13), the angle $\angle C_0AB'$ has the form of

$$w = \angle C_0 AB' = \tan^{-1}\frac{C_0 B'}{AB'} = \tan^{-1}\frac{\mathrm{g}\cdot\sin b}{\mathrm{g}\sqrt{(\cos b)^2 - (\cos q\sin j)^2}},$$

which can be simplified as

$$w = \tan^{-1}\frac{\sin(g-90°)}{\sqrt{\cos^2(g-90°) - (\cos q\sin j)^2}} = \tan^{-1}\frac{-\cos g}{\sqrt{\sin^2 g - (\cos q\sin j)^2}}.$$

Finally *w* has the form of

$$w = -\tan^{-1}\frac{\cos g}{\sqrt{\sin^2 g - (\cos q\sin j)^2}}.$$

The equality of $\alpha - \theta = w$ can thus be written as

$$a - q = -\tan^{-1}\frac{\cos g}{\sqrt{\sin^2 g - (\cos q\sin j)^2}},$$

which can be reduced as

$$\tan^{-1}\frac{\tan q}{\cos j} + \tan^{-1}\frac{\cos g}{\sqrt{\sin^2 g - (\cos q\sin j)^2}} = q \qquad \text{(C-14)}$$

through the use of (C-8). $\varphi(\theta, d, t, f, \lambda)$ can be obtained from(C-14) , where γ is given in (C-10).

What has been shown in Figure C. 5 is a clockwise deviation of OB from being perpendicular to the tilt axis T. A counterclockwise deviation of OB from being perpendicular to the tilt axis T within φ similarly results in an intersection of the (1, 1, -1) reciprocal lattice spot with the Ewald sphere after tilt. Further more, there exists a multiplicity of four for the {1, 1, 1} reciprocal lattice spots below the image plane (they are the (1,1, -1), (1, -1, -1), (-1, 1, -1) and (-1, -1, -1) reciprocal lattice spots), the probability of having the intersection of the (1, 1, -1) reciprocal lattice spot with the Ewald sphere after tilting a <001> crystal by $\theta = 35.26^o$ is thus

$$P_3(\theta, d, t, f, \lambda) = 2\times 4\times\varphi / 360 = \varphi(t, d, f, \theta, \lambda) / 45.$$

C2.2. DERIVATION OF (4-5): MAXIMUM PERCENT DIFFERENCE BETWEEN LATTICE FRINGE SPACING AND LATTICE SPACING

As shown in Figure C. 7, the lattice fringe vector is shorter than the corresponding reciprocal lattice vector, i.e., the following inequality of g' = OE < g = OC is true. Hence the lattice fringe spacing is longer than the corresponding lattice spacing, i.e., the following inequality of d' > d is true. For a crystal diameter t, therefore there exists a maximum percent error δ for the lattice fringe spacing d'. Stated differently, for an upper limit of percent error of lattice fringe spacing, δ, there exists a lower limit of crystal size t_{min}. Below t_{min}, the maximum percent error of lattice fringe spacing d' is greater than δ. δ is defined through the following equation of

$$d' = (1 + \ddot{a})d ,$$

which can be rewritten as

$$g' = \frac{1}{1+d} g . \tag{C-15}$$

From the triangle ΔDC_0O, the following equation of

$$\cos \angle DC_0O = \frac{DC_0^2 + OC_0^2 - DO^2}{2 \cdot DC_0 \cdot OC_0} = \frac{(g_l + g_t)^2 + g^2 - g_l^{\,2}}{2 \cdot (g_l + g_t) \cdot g}$$

can be obtained. The lattice fringe vector OE has the form of

$$g' = OE = \sqrt{OC_0^2 + C_0E^2 - 2 \cdot OC_0 \cdot C_0E \cdot \cos \angle DC_0O} ,$$

which is changed through substitution and reduction to

$$g' = \sqrt{g^2 + g_t^2 - 2g \cdot g_t \cdot \frac{(g_l + g_t)^2 + g^2 - g_l^{\,2}}{2 \cdot (g_l + g_t) \cdot g}} = \sqrt{g^2 + g_t^2 - g_t \frac{g^2 + g_t^2 + 2g_l g_t}{g_l + g_t}} .$$

Through using equation (C-15), the above equation is changed to

$$\sqrt{g^2 + g_t^2 - g_t \frac{g^2 + g_t^2 + 2g_l g_t}{g_l + g_t}} = \frac{1}{1+d} g^2 . \tag{C-16}$$

$t_{min}(\delta)$ can be determined from (C-16).

C2.3. DERIVATION OF (4-6): CRYSTAL SIZE RANGE OF VALIDITY IN QUANTIFYING p_3

In order for the model to be valid in quantifying the probability p_3, the (1, 1, -1) reciprocal lattice spot must be large enough to intersect the Ewald sphere after a tilt of 35.3°. When the (2, -2, 0) reciprocal lattice vector is perpendicular to the tilt axis, the (1, 1, -1) reciprocal lattice spot comes closest to the Ewald sphere. There exists a lower limit of the (1, 1, -1) reciprocal lattice spot radius, at which the spot becomes tangent with the Ewald sphere. This corresponds to an upper limit of crystal diameter. Equally stated, when the crystal diameter is above this limit, the (1, 1, -1) reciprocal lattice spot becomes so small that it will never intersect the Ewald sphere after a tilt of 35.3°. In the following discussion, we are going to refer to Figure C. 7, and the (2, -2, 0) reciprocal lattice vector is perpendicular to the tilt axis T. Therefore please notice that in this figure, (1, 1, -1) is on the image plane, i.e., $\angle DOC_0 = 90°$. In the right triangle ΔDOC_0, the following euqation of

$$OD^2 + OC_0^2 - DC_o^2 = 0$$

can be obtained, which can be further reduced to

$$g_l^2 + g^2 - \left(g_l + g_t\right)^2 = g^2 - g_t^2 - 2g_l g_t = \frac{1}{d^2} - \frac{f^2}{t^2} - \frac{2f}{lt} = 0.$$

Multiplying oth sides of the equation by $\lambda d^2 t^2$ and subsequent reduction give the following forms of

$$lt^2 - l\,f^2 d^2 - 2\,fd^2 t = l\left(t^2 - \frac{2\,fd^2}{l}t - f^2 d^2\right) = l\left[\left(t - \frac{fd^2}{l}\right)^2 - \frac{f^2 d^4}{l^2} - f^2 d^2\right] = 0.$$

The upper limit of crystal diameter can be obtained as

$$t = \frac{fd^2}{l} + \sqrt{\frac{f^2 d^4}{l^2} + f^2 d^2} = \frac{fd^2}{l} + fd\sqrt{\frac{d^2}{l^2} + 1}.$$

For d = 2.124 Å for WC_{1-x} crystals, t = 361 Å. The projection size of crystal A whose lattice parameters were determined in our experiment, about 100 Å, is below this upper limit.

Since the Ewald sphere curves up, for greater t, the (1, 1, -1) reciprocal lattice spot is too small to contact the Ewald sphere after tilting about **T** by θ, regardless of how the crystal is azimuthally oriented (even with the (2, -2, 0) reciprocal lattice vector parallel to T).

C3. DERIVATIONS OF (4-7), (4-8), (4-9) and (4-10): UNCERTAINTIES

C3.1. DERIVATION OF (4-7)

By definition, the following equality of

$$d = \frac{1}{g}$$

is true, where d is the lattice spacing, and g is the magnitude of the reciprocal lattice vector. Taking the derivatives of both sides of the equation gives the following equation of

$$d\,d = -\frac{1}{g^2} d\,g\,,$$

which, upon deviding both sides by d, is changed to the following form of

$$\frac{d\,d}{d} = \left(-\frac{1}{g^2} d\,g \right) g = -\frac{d\,g}{g}.$$

Therefore the uncertainty of a reciprocal lattice vector is equal to that of the spacing of the corresponding lattice fringes in magnitude.

The following discussion assumes a flat Ewald sphere.

C3.2. DERIVATION OF (4-8): RECIPROCAL LATTICE VECTOR UNCERTAINTY IN IMAGE PLANE

There are three factors contributing to the uncertainty of a reciprocal lattice vector in the image plane. They are going to be discussed in the follwing three subsections individually.

C3.2.1. Lateral Uncertainty of the Reciprocal Lattice Vector As shown in Figure C. 8, O is the position of (000), A is center of the reciprocal lattice spot whose radius is $g_t = \frac{f}{t}$, where t is the diameter of the crystal. When the reciprocal lattice

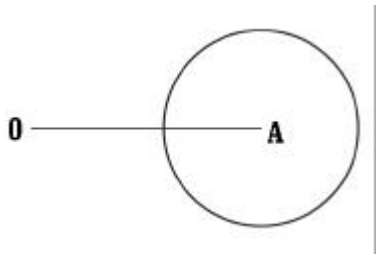

Figure C. 8. Schematic illustrating the uncertainty of a reciprocal lattice vector in the image plane when the vector lies in the image plane. Point O is the origin of the reciprocal space, (000), Point A is center of the reciprocal lattice spot. The reciprocal lattice vector OA lies on the image plane. Such an uncertainty is evaluated as the ratio of the radius of the reciprocal lattice spot and the magnitude of the reciprocal lattice vector, OA.

vector $\mathbf{g} = \overrightarrow{OA}$ is on the image plane, the lateral uncertainty is equal to the radius of the reciprocal lattice spot, i.e., the following equality of

$$d\,g = g_t = \frac{f}{t}$$

is true. Dividing both sides of the equation by g gives the following eualtion of

$$\frac{d\,g}{g} = \frac{fd}{t}.$$

C3.2.2. <u>When the Reciprocal Lattice Vector is off the Image Plane</u> As shown in Figure C. 9, O is the origin of the reciprocal lattice, (000). When the reciprocal lattice vector **g** = OA is off the image plane, the corresponding lattice fringe vector has a different magnitude of g'= OB. Here we consider an extreme case in which the reciprocal lattice spot is tangent with the image plane at the point B. The reciprocal lattice spot has a radius of g_t = f/t. The magnitude of the lattice fringe vector can be obtained as

$$g' = OB = \sqrt{g^2 - g_t^2} = g\sqrt{1-\left(\frac{g_t}{g}\right)^2} = g\sqrt{1-\left(\frac{fd}{t}\right)^2}.$$

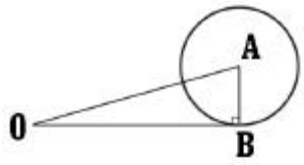

Figure C. 9. Schematic illustrating the uncertainty of a reciprocal lattice vector which arises when the reciprocal lattice vector is off the image plane. What is shown here is the extreme case in which the reciprocal lattice spot is tangent with the image plane. Point O is the origin of the reciprocal space, (000). Point A is center of the reciprocal lattice spot which is tangent with the Ewald sphere at B. Such an uncertainty is equal to the percent difference between OB and OA.

This can be approximated as

$$g' \simeq g\left[1-\frac{1}{2}\left(\frac{fd}{t}\right)^2\right],$$

if $\left(\frac{fd}{t}\right)^2 \ll 1$, i. e. t >>fd.

Therefore the corresponding uncertainty is quantified as

$$\frac{dg}{g}=\frac{|g'-g|}{g}=\frac{1}{2}\left(\frac{fd}{t}\right)^2.$$

C3.2.3. <u>Camera Constant Uncertainty</u> The camera constant here is that of the power spectrum of an HRTEM image from which the lattice fringe vector can be measured, and denoted as λL. The causes of such an uncertainty are the magnification variations both of the microscope operated at the working magnification, and in the image-digitizing process. From the equation of $r=\frac{lL}{d}$, the relation

$$g=\frac{1}{d}=\frac{r}{lL}$$

can be obtained. After taking the derivative on both sides, the relationship

$$dg=-\frac{r}{(lL)^2}d(lL)$$

follows. Finally the corresponding uncertainty can be written as

$$\frac{dg}{g} = -\frac{r}{(lL)^2} d(lL) \frac{lL}{r} = -\frac{d(lL)}{lL}.$$

The sources from which the above uncertainties arise are uncorrelated. Therefore, the average of the cross terms involving the products of the deviations in different variables vanishes. In the below expression, we use subscript x to denote the component of a quantity in the horizontal image plane. The overall reciprocal lattice vector uncertainty in the image plane is expressed as follows

$$\left(\frac{dg}{g}\right)_x = \sqrt{\left(\frac{fd}{t}\right)^2 + \left[\frac{d(lL)}{lL}\right]^2 + \left[\frac{1}{2}\left(\frac{fd}{t}\right)^2\right]^2}.$$

C3.3. DERIVATION OF (4-9): RECIPROCAL LATTICE VECTOR UNCERTAINTY IN ELECTRON BEAM DIRECTION

There are three factors contributing to the uncertainty of a reciprocal lattice vector in the electron beam direction. They are going to be discussed in the follwing three subsections individually.

C3.3.1. Camera Constant Uncertainty As shown in Figure C. 10, point O is the origin of the reciprocal lattice, (000). The reciprocal lattice vector is represented as segment OA. Segment AB is the uncertainty of the reciprocal lattice vector resulted from that of the camera constant. The segments BD and OD are parallel to the electron beam direction and the image plane, respectively. It then becomes apparent that the angle of $\angle$AOD is the amount of tilt θ around the tilt axis to bring the reciprocal lattice vector to the image plane for stereo analysis. The tilt axis direction points into the paper. We use subscript z to denote the component of a quantity along the direction of the electron beam. The uncertainty can be quantified through the following equations of

$$\left(\frac{dg}{g}\right)_z = \frac{BC}{CD} = \frac{AB \cdot \sin q}{OA \cdot \sin q} = \frac{AB}{OA} = \frac{dg}{g} = \frac{d(lL)}{lL}.$$

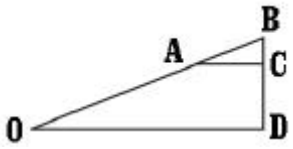

Figure C. 10. Schematic illustrating the contribution to the uncertainty of a reciprocal lattice vector, represented as OA shown in the figure, along the electron beam direction, from that of the camera constant of the power spectrum of the HRTEM image. The point O is the origin of the reciprocal lattice, (000), the segment AB is the uncertainty of the reciprocal lattice vector resulted from that of the camera constant. The segments BD and OD are parallel to the electron beam direction and the image plane, respectively. It then becomes apparent that the angle of ∠AOD is the amount of tilt around the tilt axis to bring the reciprocal lattice vector to the image plane for stereo analysis. The tilt axis direction points into the paper.

C3.3.2. <u>Tilt Uncertainty</u> As shown in Figure C. 11, point O is the origin of the reciprocal lattice, (000). The reciprocal lattice vector is represented as segment OA. The angle ∠AOB is the uncertainty of tilt δθ. The magnitude of the corresponding uncertainty of the reciprocal lattice vector δg is equal to segment AB. Segment OE bisects the angle ∠AOB. The relationship of OE ⊥AB is true. Segment AD is parallel to the electron beam direction. Segment OD is parallel to the image plane. The relationship of AD ⊥ OD is true. The tilt axis direction points into the paper. The angle ∠AOD is the amount of tilt around the tilt axis to bring A to the image plane, denoted as θ, i.e., it is true that ∠AOD=θ. The following relationship of ∠BAC = ∠AOD = θ is also true. From the figure, it follows that

$$d g_z = AC = AB\cos\angle BAC = AB\cos q \ ,$$

which simplifies to

$$d g_z \simeq AO\cdot dq\cdot\cos q = g\cdot dq\cdot\cos q \ ,$$

if δθ <<1. Therefore the uncertainty becomes

$$\left(\frac{d g}{g}\right)_z = \frac{AC}{AD} = \frac{g dq\cos q}{g\sin q} = \frac{dq}{\tan q} \ .$$

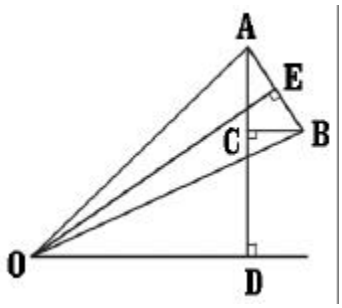

Figure C. 11. Schematic illustrating the contribution to the uncertainty of a reciprocal lattice vector, represented as segment OA in the figure, along the electron beam direction from the tilt uncertainty. O is the origin of the reciprocal lattice (000), segment AB is the uncertainty of g resulted from that of tilt. The tilt axis direction points into the paper. The angle ∠AOD is the amount of tilt around the tilt axis to bring the reciprocal lattice vector OA to the image plane, θ. The angle ∠AOB is the uncertainty of tilt δθ. Segment OE bisects the angle ∠AOB. It is true that OE ⊥AB. Segment AD is parallel to the electron beam. Such a contribution is quantified as the ratio between the segments AC and AD.

C3.3.3. Reciprocal Lattice Spot Uncertainty along Electron Beam Direction

As shown in Figure C. 12, O is the origin of the reciprocal lattice (000).The reciprocal lattice vector is represented as the segment OA. The angle ∠AOC is equal to the amount of tilt to bring the reciprocal lattice vector to the image plane, θ. The tilt axis direction points into the paper. Segment AC is parallel to the electron beam. Segment AB is equal to the radius of the reciprocal lattice spot, g_t.

The uncertainty can be obtained from the equality string

$$\left(\frac{dg}{g}\right)_z = \frac{AB}{AC} = \frac{g_t}{g\sin q} = \frac{fd}{t\sin q}.$$

Similar to the treatment adopted in C3.2, the sources from which the above uncertainties arise are assumed to be uncorrelated. As a result, the overall uncertainty of a reciprocal lattice vector along the electron beam direction is of the form

$$\left(\frac{dg}{g}\right)_z = \sqrt{\left[\frac{d(lL)}{lL}\right]^2 + \left(\frac{dq}{\tan q}\right)^2 + \left(\frac{fd}{t\sin q}\right)^2}.$$

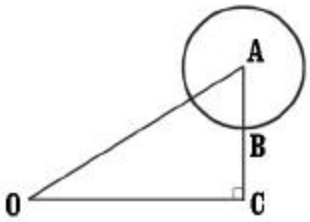

Figure C. 12. Schematic illustrating the contribution to the uncertainty of a reciprocal lattice vector, represented as segment OA in the figure, along the electron beam direction from that of the reciprocal lattice spot in the same direction. Point O is the origin of the reciprocal lattice (000). The angle ∠AOC is equal to the amount of tilt to bring the reciprocal lattice vector to the image plane. The tilt axis direction points into the paper. Segment AC is parallel to the electron beam. Segment AB is equal to the radius of the reciprocal lattice spot along the electron beam direction. Such a contribution is equal to the ratio between the lengths of AB and AC.

C3.4. DERIVATION OF (4-10): INTERPLANAR ANGLE UNCERTAINTY

The uncertainty of an inter-planar angle in the lattice image is due to the azimuthal uncertainty of the corresponding two reciprocal lattice spots. As shown in Figure C. 13, O is the origin of the reciprocal lattice (000). Segment OA represents one of the two reciprocal lattice vectors from which the interplanar angle can be measured. Segments OB and OC are tangent with the reciprocal lattice spot centered at A. The angular uncertainty of the reciprocal lattice spot is equal to angle ∠AOB and can be obtained from

$$\angle AOB = \sin^{-1}\frac{AB}{AO} = \sin^{-1}\frac{g_t}{g} = \sin^{-1}\frac{fd}{t}.$$

Since measuring interplanar angles invoves two reciprocal lattice spots in the power spectrum, the interplanar angle uncertainty is thus twice as much, and can be quantified as

$$(dj)_x = 2\angle AOB = 2\sin^{-1}\frac{fd}{t}.$$

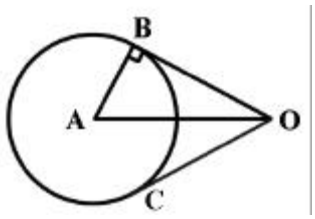

Figure C. 13. Schematic illustrating the contribution to the uncertainty of an interplanar angle from the azimuthal uncertainty of the two corresponding reciprocal lattice spots. Point O is the origin of the reciprocal lattice (000). Segment OA represents one of the two reciprocal lattice vectors. Segments OB and OC are tangent with the reciprocal lattice spot centered at A. Angle ∠BOA is the azimuthal uncertainty of reciprocal lattice spot A. Since there are two reciprocal lattice spots involved in measuring interplanar angles, the interplanar angle uncertainty is twice of angle ∠BOA.

BIBLIOGRAPHY

Amos L. A., Henderson R., Unwin P. N. T. (1982) “Three-dimensional Structure Determination by Electron Microscopy of Two-dimensional Crystals”, *Progress in Biophysics and Molecular Biology*, **39**, 188-231.

Baibich M. N., Broto J. M., Fert A., Dau F. N. V., and Petroff F. (1988) “Giant Magnetoresistance of (001)Fe/(001)Cr Magnetic Superlattices”, *Physical Review Letters*, **61**, 2472-2475.

Basinski Z. S. (1962) “Stereo Electron Micrography of Dislocation Networks”, *Proceedings of the 5th International Congress for Electron Microscopy*, Academic Press, New York, **1**, B. 13.

Beeli C., Doudin B., Ansermet J-Ph. and Stadelmann P.A. (1997) “Measurement of the Remnant Magnetization of Single Co/Cu and Ni Nanowires by off-axis TEM Electron Microscopy”, *Ultramicroscopy*, **67**, 143-151.

Beeston B. E. P., Horne R. W. and Markham R. (1972) “Electron Diffraction and Optical *Practical Methods in Electron Microscopy* (edited by Glauert A. M., North-Holland Publishing Company, Amsterdam, New York, Oxford), p. 295-297.

Bevington P. R. (1969) *Data Reduction and Error Analysis for the Physical Sciences*, McGraw-Hill Book Company, New York, San Francisco, St. Louis, Toronto, London, Sydney, p. 58-60.

Chadderton L.T. (1961) “Electron Microscopy of Crystal Lattices: an Anomalous *Nature*, **189**, 564-565.

Changmo S. and Williams D. B. (1991) “Principles and applications of convergent beam electron diffraction: A bibliography (1938-1990)”, *Journal of Electron Microscopy Technique*, **17**, 95-118.

Chen C. W., Mastenbroek A. and Elen J. D. (1972) “An Electron Stereomicroscopy Analysis of Voids Produced in Nickel During Ion Irradiation”, *Radiation Effect*, **16**, 127-132.

Cowley J.M (1981) “Coherent interference effects in SIEM and CBED”, *Ultramicroscopy*, **7**, 19 -26.

Cowley J. M. (1996) “Electron Nanodiffraction: Progress and Prospects”, *Journal of Electron Microscopy*, **45**, 3-10.

Cowley J. M. (1992) “Twenty Forms of Electron Holography”, *Ultramicroscopy*, **41**, 335-348.

Cox G. and Juniper B. (1973) “the Application of Stereo-micrography in the High Voltage Electron Microscope to Studies of Cell-wall Structure and Deposition”, *Journal of Microscopy*, **97**, 29-40.

Crowther R. A., DeRosier D. J., and Klug A. (1971) “The Reconstruction of A Three-dimensional Structure from Its Projections and Its Application to Electron Microscopy”, *Proceedings of the Royal Society of London*, A. **317**, 319-340.

DeRosier D. J. and Klug A. (1968) “Reconstruction of Three-dimensional Structures from Electron Micrographs”, *Nature*, **217**, 130-134.

Eades J. A. (1989) ed: “Special issues of the Journal of Electron Microscopy Technique on convergent beam electron diffraction”, *Journal of Electron Microscopy Techniques*, Nos. 1, 2, **13**.

Edington J. W. (1976a) *Practical Electron Microscopy in Materials Science*, N.V.Philips' Gleoilampenfabrieken, Eindhoven, p. 60.

Edington J. W. (1976b) *Practical Electron Microscopy in Materials Science*, N.V.Philips' Gleoilampenfabrieken, Eindhoven, p. 60-61.

Edington J. W. (1976c) *Practical Electron Microscopy in Materials Science*, N.V.Philips' Gleoilampenfabrieken, Eindhoven, p. 60-88.

Edington J. W. (1976d) *Practical Electron Microscopy in Materials Science*, N.V.Philips' Gleoilampenfabrieken, Eindhoven, p. 117-118.

Frank J. (1989) "Three-dimensional Imaging Techniques in Electron Microscopy", *BioTechniques*, **7**, 164-173.

Frank J. and McEwen B. F. (1992) "Alignment by Cross-Correlation", in *Electron Tomography – Three-dimensional Imaging with the Transmission Electron Microscope*, (Edited by Frank J., Plenum Press, New York and London), p. 205-214.

Frank J. and Radermacher M. (1986) *Advanced Techniques in Biological Electron Microscopy*, Springer-Verlag, Berlin, p. 1-72.

Frank J. edited, (1992a) *Electron Tomography – Three-dimensional Imaging with the Transmission Electron Microscope*, Plenum Press, New York and London, p. 1.

Frank J. edited, (1992b) *Electron Tomography – Three-dimensional Imaging with the Transmission Electron Microscope*, Plenum Press, New York and London, p. 4.

Frank J. edited, (1992c) *Electron Tomography – Three-dimensional Imaging with the Transmission Electron Microscope*, Plenum Press, New York and London, p. 197-214.

Frank J. edited, (1992d) *Electron Tomography – Three-dimensional Imaging with the Transmission Electron Microscope*, Plenum Press, New York and London, p. 281-389.

Fraundorf P. (1981a) “Stereo Analysis of Single Crystal Electron Diffraction Data”, *Ultramicroscopy*, **6**, 227-236.

Fraundorf P. (1981b) “Stereo Analysis of Electron Diffraction Pattern from Known *Ultramicroscopy*, **7**, 203-206.

Fraundorf P. (1987) “Determining the 3D Lattice Parameters of Nanometer-sized Single Crystals from Images”, *Ultramicroscopy*, **22**, 225-230.

Gabor D. (1948) “A New Microscopic Principle”, *Nature*, **161**, 777-778.

Gabor D. (1949) “Microscopy by Reconstructed Wave-fronts”, *Proceedings of the Royal Society of London*, Series A, **197**, 454-486.

Gevers, R. (1970) “Kinematical Theory of Electron Diffraction”, In *Modern Diffraction and Imaging Techniques in Materials Science* (edited by Amelinckx, S., Gevers, R., Remaut, G. J., Landuyt, V., North-Holland Publishing Company, Amsterdam, London), p. 1-33.

Ghosh S. and Inganas O. (1999) “Self-assembly of A Conducting Polymer Nanostructure by Physical Crosslinking: Applications to Conducting Blends and Modified Electrodes”, *Synthetic Metals*, **101**, 413-416.

Gibson J. M. and Treacy M. M. J. (1997) “Diminished Medium-Range Order Observed in Annealed Amorphous Germanium”, *Physical Review Letter*, **78**, 1074-1077.

Gibson J. M. and Treacy M. M. J. (1998) “Paracrystallites Found in Evaporated Amorphous Tetrahedral Semiconductors”, *Journal of Non-crystalline Solids*, **231**, 99-110.

Glauer A. M. and Mayo C. R. (1973) “the Study of the Three-dimensional Structural Relationship in Connective Tissues by High Voltage Electron Microscopy”, *Journal of Microscopy,* **97**, 83-94.

Hasegawa H., Fujikura H., and Okada H. (2000) “Molecular-beam Expitaxy and Device Application of III-V Semiconductor Nanowires”, *MRS Bulletin*, **24**, 25-30.

Heimendahl M. V., Bell W., and Thomas G. (1964) “Applications of Kikuchi Line Analyses in Electron Microscopy”, *Journal of Applied Physics,* **35**, 3614 -3617.

Henderson R. and Uwin P. N. T. (1975) “Three-dimensional Model of Purple Membrane Obtained by Electron Microscopy”, *Nature*, **257**, 28-31.

Herman G. T., et al. (1979) *Image Reconstruction from Projections*, Springer-Verlag, Berlin.

Hirsch P., Howie A., Nicholson R., Pashley W., and Whelan M. J. (1977a) *Electron Microscopy of Thin Crystals*, Krieger Publishing Company, Malabar, FL, p. 119-124.

Hirsch P., Howie A., Nicholson R., Pashley W., and Whelan M. J. (1977b) *Electron Microscopy of Thin Crystals,* Krieger Publishing Company, Malabar, FL, p. 161

Hirsch P., Howie A., Nicholson R., Pashley W., and Whelan M. J. (1977c) *Electron Microscopy of Thin Crystals*, Krieger Publishing Company, Malabar, FL, p. 195.

Hirsch P., Howie A., Nicholson R., Pashley W., and Whelan M. J. (1977d) *Electron Microscopy of Thin Crystals,* Krieger Publishing Company, Malabar, FL, p. 310-311.

Hirsch P., Howie A., Nicholson R., Pashley W., and Whelan M. J. (1977e) *Electron Microscopy of Thin Crystals*, Krieger Publishing Company, Malabar, FL, p. 454-457.

Hirsch P., Howie A., Nicholson R., Pashley W., and Whelan M. J. (1977f) *Electron Microscopy of Thin Crystals*, Krieger Publishing Company, Malabar, FL, p. 456.

Hoppe W., Wenzl H., Schramm H. J. (1976) "New 3D Reconstruction Techniques at Minimal Doses Conditions", *Proceedings of the 6th European Congress on Electron Microscopy*, Jerusalem, **II**, 58-60.

Hoppe W. and Grill B. (1977) "Prospects of Three-dimensional High Resolution Electron Microscopy of Non-Periodic Structures", *Ultramicroscopy*, **2**, 153-168.

Hoppe W. (1981) "Three-dimensional Electron Microscopy", *Annual Review of Biophysics and Bioengineering*, **10**, 563-592.

Hudson B. (1973) "the Application of Stereo-technique to Electron Micrographs", *Journal of Microscopy*, **98**, 396-401.

Iijima S. (1991) "Helical microtubules of graphitic carbon", *Nature*, **354**, 56-58.

International Union of Crystallography, (1952) International Tables for X-Ray Crystallography, **1**, 531-535.

James J. W. and Shih W. at the Materials Research Center of the University of Missouri-Rolla (1998), private communication.

JCPDS-ICDD, 25-1316.

Johari O. and Thomas G. (1996) *the Stereographic Projection and Its Application in Techniques of Metal Research*, Interscience, New York.

Kikuchi S.(1928) “Diffraction of Cathode Rays by Mica”, *Japanese Journal of Physics*, **5**, 83-96.

Kim B. K., Ha G. H., Lee G. G. and Lee D. W. (1997) “Structure and Properties of Nanophase WC/Co/VC/TaC Hard Metal”, *Nanostructured Materials*, **9**, 233-236.

Knoll M. and Ruska E. (1932) “Das Elektronenmikroskop.”, *Zeitschrift fuer Physik*, **78**, 318-339.

KnowledgeTek (1999) *Disk Drive Technology Course*, 15-2.

Kossel W. and Möllenstedt G. (1939) “Elektroneninterferenzen im Konvergenten *Annalen der Physik*, **36**, 113-140.

Krainer E. and Robitsch J. (1967) “Röntgenographischer Nachweis des kubischen Wolframkarbides in funkenerosiv bearbeiteten Hartmetallen und in reinen Wolframschmelzkarbiden”, *Planseeberitchte Fuer Pulvermetallurgie*, **15**, 46-56.

Kung H. and Foecke T. (1999), “Mechanical behavior of nanostructured materials”, *MRS Bulletin*, **24**, 14-15.

Lang A. R. (1959) “Studies of Individual Dislocations in Crystals by X-Ray Diffraction Microradiography”, *Journal of Applied Physics*, **30**, 1748-1755

Lawrence M. C. (1992) “Least-Squares Method of Alignment Using Markers”, in *Electron Tomography – Three-dimensional Imaging with the Transmission Electron Microscope*, (Edited by Frank J., Plenum Press, New York and London), p. 197-204.

LePoole J. B. (1947) “A New Electron Microscope With Continuously Variable *Philips Technical Review*, **9**, 33-64.

Levine E., Bell W. L., and Thomas G. (1966) “Further Applications of Kikuchi Diffraction Patterns; Kikuchi Maps”, *Journal of Applied Physics*, **37**, 2141-2148.

Lewitt R. M. and Bates R. H. T. (1978) “Image Reconstruction from Projections I: General Theoretical Considerations”, *optiks* (Stuggart), **50**, 189-204

Liu M. and Cowley J. (1994) “Structure of carbon nanotubes studied by HRTEM and Nanodiffraction”, *Ultramicroscopy*, **53**, 333-342.

Liu Q., Meng Q. and Hong B. (1989) “Calculation of Tilt Angles for Crystal Specimen Orientation Adjustment Using Double-tilt and Tilt-rotate Holders”, *Micron and Microscopica Acta*, **20**, 255-259.

Liu Q. (1989) “An Equation to Determine the Practical Tilt Angle of A Double-tilt Specimen Holder and Its Application to Transmission Electron Microscopy”, *Micron and Microscopica Acta*, **20**, 261-264.

Liu Q. (1990) “A Method for Determining the Crystal Orientation for Any Tilt Position when Using A Transmission Electron Microscope Double-tilt Specimen Holder”, *Micron and Microscopica Acta*, **21**, 105-107.

Liu Q., Huang X. and Yao M. (1992) “New Method for Determining Grain Boundary *Ultramicroscopy*, **41**, 317-321.

Liu Q. (1995) “A Simple and Rapid Method for Determining Orientations and Misorientations of Crystalline Specimens in TEM”, *Ultramicroscopy*, **60**, 81-89.

Liu Y., Penczek P. A., McEwen B. F., Frank J. (1995) “A Marker-free Alignment Method for Electron Microscopy”, *Ultramicroscopy*, **58**, 393-402.

Maher D. M., Eyer B. L. and Bartlett A. F. (1971) “Neutron Irradiation Damage in Molybdenum, Part IV. A Quantitative Correlation between Irradiated and Irradiated-Annealed Structures”, *Philosophical Magazine*, **24**, 745-765.

Mallinson J. (1996) *Magneto-Resistive Heads, Fundamentals and Applications, Academic Press,* Sandiego, London, Boston, New York, Sydney, Tokyo, Toronto, p. 97.

Malm J. –O and O'Keffe M.A. (1997) “Deceptive ‘Lattice Fringes’ in High-resolution Micrographs of Metal Nanoparticles”, *Ultramicroscopy*, **68**, 13-23.

Menter J.W. (1958) “The Electron Microscopy of Crystal lattices”, *Advances in Physics*, **7**, 299-348

Miura N., Matsuda Y. H., Uchida K. and Arimoto H. (1999) “Magneto-optical Study of Semiconductor Nanostructures in High Magnetic Fields”, *Journal of Physics-Condensed Matter*, **11**, 5917-5928.

Möck P. (1991) “A Direct Method for Orientation Determination Using TEM (I) *Crystal Research and Technology*, Berlin, **26**, 653-658.

Möck P. (1991) “A Direct Method for Orientation Determination Using TEM (II) *Crystal Research and Technology*, Berlin, **26**, 797-801.

Möck P. (1997) “Direct Crystallographic Analysis Using Electron Microscopy”, unpublished.

Monosmith W. B. and Cowley J. (1984) “Electron diffraction from very small gold *Ultramicroscopy*, **12**, 177-184.

Okamoto P. R., Levine E., and Thomas G. (1967) “Kikuchi Maps for hcp and bcc *Journal of Applied Physics*, **38**, 289-296.

Qin W., Shih W., Li J., James J. W., Siriwardane H. and Fraundorf P. (1998) "High-Resolution Transmission Electron Microscope Analysis of Tungsten Carbide Thin Films", *Materials Research Society Symposium Proceedings*, **520**, 217-222.

Qin W., Siriwardane H. and Fraundorf P. (1999) "The 3D lattice Parameters of A (Nano)crystal from Lattice Images at Two Tilts", *Proceedings of the Microscopy Society of America Annual Meeting*, p. 188-189.

Qin W. and Fraundorf P. (2000a) "Crystal lattice parameters from direct space images at two tilts", *Los Alamos Archives* at http://xxx.lanl.gov/abs/cond-mat/0001139.

Qin W. and Fraundorf P. (2000b) "Probability and Uncertainty in Stereo Lattice *Proceedings of the Microscopy Society of America Annual Meeting*.

Qin W., Fraundorf P. (2000c) "Lattice Fringe Visibility after Tilt", *Proceedings of the Microscopy Society of America Annual Meeting.*

Randon J. (1917) "Über die Bestimmung von Funktionen durch ihre Integralwerte Längs gewisser Mannigfaltigkeiten", Berichte ueber die Verhandlungen der Königlichen Sächsischen Gesellschaft der Wissenschaften Mathematisch - Physische Klasse, **69**, 262-277.

Riecke W. D. and Sakaki Y. (1959) "Zur Untersuchung des reziproken Gitters von Einkristallen mit Hilfe von Kikuchi-Diagrammen", *Zeitschrift fuer Physik*, **156**, 534-554.

Russ J. (1990) *Computer-assisted Microscopy, the Analysis and Measurement of Images*, Plenum Press, New York.

Selby S. M. (1972) *Standard Mathematical Tables*, 20th Edition, the Chemical Rubber Co., p. 199.

Sellmyer D. J., Yu M. and Kirby, R. D. (1999) “Nanostructured Magnetic Films for Extremely High Density Recording”, *Nanostructured Materials*, **12**, 1021-1026.

Shen C. (1997) “Lateral Displacement Maps Within Scanning Probe Microscope Images”, Thesis.

Spence J. C. H. (1988a) *Experimental High-Resolution Electron Microscopy*, Oxford University Press, New York, Oxford, p. 83-89.

Spence J. C. H. (1988b) *Experimental High-Resolution Electron Microscopy*, Oxford University Press, New York, Oxford, p. 87-89.

Spence J. C. H. (1988c) *Experimental High-Resolution Electron Microscopy*, Oxford University Press, New York, Oxford, p. 365-402

Tambuyser P. (1984) “Calculation of Tilt Angles for Obtaining Stereo Transmission Electron Micrographs from Crystalline Specimens”, *Journal of Materials Science Letters*, **3**, 184-186.

Tambuyser P. (1985) “the Direct Indexing of Two-beam Electron Diffraction Patterns”, *Metallography*, **18**, 41-49.

Thomas G. (1970a) “Kikuchi Electron Diffraction and Applications”, In *Modern Diffraction and Imaging Techniques in Materials Science* (edited by Amelinckx, S., Gevers, R., Remaut, G. J., Landuyt, V., North-Holland Publishing Company, Amsterdam, London), p. 167-168.

Thomas G. (1970b) “Kikuchi Electron Diffraction and Applicati *Modern Diffraction and Imaging Techniques in Materials Science* (edited by Amelinckx, S.,

Gevers, R., Remaut, G. J., Landuyt, V., North-Holland Publishing Company, Amsterdam, London), p. 177.

Thomas G. (1970c) “Kikuchi Electron Diffraction and App *Modern Diffraction and Imaging Techniques in Materials Science* (edited by Amelinckx, S., Gevers, R., Remaut, G. J., Landuyt, V., North-Holland Publishing Company, Amsterdam, London), p. 180.

Tonomura A. (1995) “Recent Development in Electron Holography for Phase Microscopy”, *Journal of Microscopy*, No. 6, **44**, 425-435.

Treacy M. M. J. and Gibson J. M. (1993), “Coherence and Multiple Scattering in “Z-contrast” Images*”, Ultramicroscopy*, **52**, 31-53.

Treacy M. M. J. and Gibson J. M. (1996) “Variable Coherence Microscopy: a Rich Source of Structural Information from Disordered Materials”, *Acta Crystallographica Section A*, **52**, 212-220.

Tsang C., Lin T., MacDonald S., Pinarbasi M., Robertson N., Santini H., Doerner M., Reith T., Vo L., Diola T. and Arnett P. (1997) “5Gb/in2 Recording Demonstration with Conventional AMR Dual Element Heads & Thin Film Disks”, *IEEE Transactions on Magnetics*, **5**, 2866-2871.

Wang Y. C., Chou T. M., Libera M. and Kelly T. F., (1997) “Transmission Electron Holography of Silicon Nanosphere with Surface Oxide Layers”, *Applied Physics Letter*, **70**, 1296-1298.

Wauters J. (1998) “Leaping into the Unknown with 0.18 μm”, *Semiconductor International*, **21**, 111-116.

White R. (1994) “Giant Magnetoresistance Materials and Their Potential as Read Head Sensors”, *IEEE Transactions on Magnetics*, **30**, 346-351.

Williams D. B. and Carter C. B. (1996a) *Transmission Electron Microscopy: A textbook for Materials Science*, Plenum Press, New York, p. 77

Williams D. B. and Carter C. B. (1996b) *Transmission Electron Microscopy: A textbook for Materials Science*, Plenum Press, New York, p. 141.

Williams D. B. and Carter C. B. (1996c) *Transmission Electron Microscopy: A textbook for Materials Science*, Plenum Press, New York, p.151-153.

Williams D. B. and Carter C. B. (1996d) *Transmission Electron Microscopy: A textbook for Materials Science*, Plenum Press, New York, p. 152.

Williams D. B. and Carter C. B. (1996e) *Transmission Electron Microscopy: A textbook for Materials Science*, Plenum Press, New York, p. 153.

Williams D. B. and Carter C. B. (1996f) *Transmission Electron Microscopy: A textbook for Materials Science*, Plenum Press, New York, p. 295-296.

Williams D. B. and Carter C. B. (1996g) *Transmission Electron Microscopy: A textbook for Materials Science*, Plenum Press, New York, p.304.

Williams D. B. and Carter C. B. (1996h) *Transmission Electron Microscopy: A textbook for Materials Science*, Plenum Press, New York, p.308.

Williams D. B. and Carter C. B. (1996i) *Transmission Electron Microscopy: A textbook for Materials Science*, Plenum Press, New York, p. 314-315.

Journal of Microscopy, **98**, 379-395.

Wyckoff R. W.G. (1982) *Crystal Structures*, 2nd edition, Volume 1, Robert Krieger Publishing Co., Malabar, Florida.

Zhang H., Takaoka A. and Miyauchi K. (1998) "A 360°-tilt Specimen Holder for Electron Tomography in An Ultrahigh-voltage Electron Microscope", *Review of Scientific Instruments*, **69**, 4008-4009.

VITA

Wentao Qin was born on February 28, 1969 in Huanjiang County, Guangxi Province, People's Republic of China. He finished his primary and secondary education in Huanjiang Elementary School, Huanjiang Middle School, High School of the Hechi Perfecture, and Liucheng High School. He received his B.S. degree in Semiconductor Physics from the University of Science and Technology of China in July 1992. After that he worked in the Institute of Semiconductor, Chinese Academy of Sciences in Beijing. His work involved Raman Scattering studies of semiconductor superlattice and quantum well structures.

He entered the Ph. D. program in the Physics Department of the University of Missouri-St. Louis in January 1995, and got his M.S. degree in January 1997. He was awarded twice Summer Graduate Research Fellowship and once Dissertation Fellowship. In the summer 1999 he worked as an Engineering Intern in the Recording Head Operation (RHO) of Seagate Technology in Bloomington, Minnesota.